Advances in Fluxgate Magnetometry for Space Physics

by

David Michael Miles

A thesis submitted in partial fulfillment of the requirements for the degree of

Doctor of Philosophy

in

Geophysics

Department of Physics
University of Alberta

Abstract

Fluxgate magnetometers are an essential tool for solar-terrestrial research and monitoring or forecasting space weather. They provide high precision measurements of the Earth's magnetic fields and can be used to infer the currents that transport energy and momentum through the magnetosphere and ionosphere. This thesis is a compilation of four journal articles describing instrumentation design advances and applications of fluxgate magnetometers for space physics. It presents the design and performance of the Magnetic Field Experiment (MGF) fluxgate magnetometer component of the Enhanced Plasma Outflow Probe (e-POP) payload on the multi-purpose Canadian Space Agency CASSIOPE small satellite mission. Since its launch on September 29, 2014, The MGF has successfully produced high-cadence low-noise measurements of the Earth's magnetic field that have been used for a variety of research topics including the study of dynamic small-scale auroral currents.

Following the success of the MGF, the design was updated and miniaturised to form the Digital Fluxgate Magnetometer (DFGM) payload, which will launch in early 2017 on the Experimental Albertan #1 CubeSat (Ex-Alta 1). The flight of this small, low-mass, low-power, low-magnetic noise, and boom-mounted fluxgate magnetometer will demonstrate the potential for high-fidelity magnetic field measurements on future multi-spacecraft CubeSat constellation missions.

Fluxgate magnetometers have long been known to be sensitive to variations in sensor temperature and to therefore require appropriate thermal calibration. A novel, low-cost thermal calibration procedure was used to compare the thermal stability of six experimental fluxgate sensors constructed from a variety of materials. Polyetheretherketone (PEEK) with 30% glass content was found to be a promising replacement for traditional expensive and difficult to machine ceramic for

future low-cost, low-mass sensors. This dataset also shows the limitations of the traditional model for how fluxgate sensor geometry and materials control its thermal gain.

Finally, measurements from e-POP and the adjacent European Space Agency Swarm A and C spacecraft were used to study the dynamics and structuring of discrete arc aurora. A case study supported by high-cadence auroral imaging shows 1-10 km structuring of the arcs, which move and evolve on second timescales and confound the traditional field-aligned current algorithms. Non-stationary electrodynamics involving reflected and interfering Alfvén waves were observed co-incident with, and at the same scale as, dynamic auroral structures. Spectral analysis of in-situ electric and magnetic measurements shows evidence of a potential role for the Ionospheric Alfvén Resonator in discrete arc dynamics.

Improved instruments and techniques are needed to fully understand the highly dynamic and localised processes that couple mass and energy through near-Earth space and thereby control space weather. The presented research demonstrates that multi-spacecraft constellation missions featuring modern, low-resource fluxgate magnetometers to provide high-fidelity magnetic field measurements can play a crucial role in future space physics research.

Preface

The research presented in this thesis was completed by the author but was also conducted as part of several national and international research collaborations. Chapter 1 presents an introduction to the subjects covered in the thesis. Chapters 2, 3, 4, and 5 are all based on manuscripts resulting, in part, from these collaborations, and at the time of submission are in various stages of the publication process. Chapter 6 presents conclusions and future work.

Chapter 2 describes the MaGnetic Field experiment (MGF) which is part of the Cassiope/e-POP satellite mission led by Prof. Andrew Yau at the University of Calgary [see e.g., *Yau and James*, 2015]. The MGF instrument is led by Principle Investigator (PI) Dr. Donald Wallis who is affiliated with the University of Calgary, Magnametrics, and the National Resources Canada Geomagnetic Laboratory. I am presently the Co-PI for the MGF payload, am responsible for the day-to-day operation of the payload, and am the corresponding author for the resulting manuscript [*Wallis et al.*, 2015]. I also commissioned the instrument, co-authored the instrument's flight firmware, was responsible for the instrument's final pre-launch checks and updates, and developed the operational data-product code. Chapter 2 of this thesis has been published as: Wallis, D.D., Miles, D.M., Narod, B.B., Bennest, J.R., Murphy, K.R., Mann, I.R., Yau, A.W. (2015) The CASSIOPE/e-POP Magnetic Field Instrument (MGF), Space Science Review. (DOI 10.1007/s11214-014-0105-z).

Chapter 3 describes a miniature Digital Fluxgate Magnetometer (DFGM) developed for the Ex-Alta 1 CubeSat led by Dr. Ian Mann. I am the DFGM instrument lead and the principle author for the manuscript [*Miles et al.*, 2016]. I also completed the majority of the instrument development, manufacturing, testing, and integration. The miniature deployable boom development was led by Miroslaw Ciurzynski. The DFGM data-processing software on the CubeSat was developed by Alex Hamilton and Brendan Bruner. Chapter 3 of this thesis has been published as: Miles, D.M., Mann, I.R., Ciurzynski, M., Barona, D., Narod, B.B., Bennest, J.R., Pakhotin, I.P., Kale, A., Bruner, B, Nokes, C.D.A., Cupido, C., Haluza-DeLay, T., Elliott, D.G., Milling, D.K., A miniature, low-power scientific fluxgate magnetometer: A stepping-stone to cube-satellite constellation missions, J. Geophys. Res. Space Phys., 2016JA023147, doi:10.1002/2016JA023147.

Chapter 4 describes the use of a novel technique for measuring the thermal gain coefficients of fluxgate magnetometers in a magnetically noisy environment using an inexpensive test setup to characterise the thermal gain coefficients of six fluxgate magnetometers constructed from different materials. I developed and conducted the experiment, and I am the principle author of the resulting manuscript [*Miles et al.*, 2017b]. The magnetometer electronics and the Macor/Macor sensor used in the experiment were built by Dr. Barry Narod and John Bennest and were provided on loan from the CARISMA magnetometer array by Dr. David Milling. The sensors built for the experiment were manufactured in collaboration with Dr. Barry Narod and John Bennest. The Acetal/Acetal sensor was provided on loan from Dr. Barry Narod. Earlier versions of this experiment used field deployable Narod Geophysics Ltd. magnetometers on loan from Dr. Martyn Unsworth. Chapter 4 of this thesis is in preparation for publication as: Miles, D.M., Mann, I.R., Kale, A. Narod, B.B., Bennest, J.R., Barona, D., Milling, D.K., Unsworth, M.J., Thermal stability of fluxgate magnetometer sensors constructed from different materials. (In preparation for Geosci. Instrum. Method. Data Syst.)

Chapter 5 presents an example of the utilisation of fluxgate magnetometer data for space science research. It presents a case-study of a discrete auroral arc whose dynamics and structure appear to involve reflected and interfering Alfvén waves potentially modulated by the Ionospheric Alfvén Resonator (IAR). I am the principal author of the manuscript [*Miles et al.*, 2017a], and I scheduled the CASSIOPE/e-POP observations that created the magnetic conjunction with the Swarm A and C spacecraft. I conducted the majority of the data analysis and am the principle author of the manuscript. Data from the e-POP Fast Auroral Imager was provided by Dr. Leroy Cogger using software developed by Andrew Howarth. Data from the Swarm EFI instrument was provided by Dr. David Knudsen and was processed and validated by Dr. Jonathan Burchill. Chapter 5 of this thesis is in preparation for publication as: Miles, D.M., Mann, I.R., Pakhotin, I.P., Knudsen, D.J., Burchill, J.K., Howarth, A., "Alfvénic dynamics and structuring of discrete auroral arcs: Swarm and e-POP observations." (In preparation for Geophys. Res. Lett.).

Appendix A is based on a technical report originally prepared by Dr. Barry Narod concerning the thermal compensation of fluxgate magnetometers sensors. It was updated and expanded in support of Miles et al. [2017b].

Dedication

“To test a perfect theory with imperfect instruments did not impress the Greek philosophers as a valid way to gain knowledge.”

— Isaac Asimov

Acknowledgments

This thesis would not have been possible without the guidance of my supervisors Professors Ian Mann and Martyn Unsworth. I am also indebted for the contributions of a great many people including: David Barona, John Bennest, Brendan Bruner, Jonathan Burchill, Bill Burris, Miroslaw Ciurzynski, Colin Cupido, Stefan Damkjar, Paul Davis, Alex Degeling, Duncan Elliot, Greg Enno, Robert Fedosejevs, Taryn Haluza-DeLay, Alex Hamilton, Andrew Howarth, Andy Kale, David Knudsen, Richard Marchand, David Milling, Mark Moldwin, Kyle Murphy, Barry Narod, Charles Nokes, Louis Ozeke, Ivan Pakhotin, Jonathan Rae, Jonathan Schmidt, Richard Sydora, Don Wallis, Len Wampler, Clare Watt, Andrew Yau.

I would like to acknowledge the Canadian Space Agency for their financial support and the Canadian National Science and Engineering Research Council for their financial support via a PGSD graduate scholarship. Funding, in-kind contributions, data sources, and related disclosures related to the individual research projects presented in Chapters 2, 3, 4, and 5 are acknowledged at the end of each chapter.

My deepest gratitude goes to my family: my wife Jessy, my daughter Cassie, my son Jack, my father Mike, my mother Wynne, my sister Sarah, and my dog Caddy. I would never have finished without their help and encouragement. Thanks for putting up with me.

Any errors or omissions are entirely my own.

Table of Contents

List of Tables

List of Figures

Glossary of Terms

3U	Three-Unit CubeSat
AC	Alternating Current
ADC	Analog to Digital Converter
ADCS	Attitude Determination and Control System
AMPERE	Active Magnetosphere and Planetary Electrodynamics Response Experiment
AMR	Anisotropic Magnetoresistance
ASI	All Sky Imager
AWG	American Wire Gauge
BCE	Before Common Era
BP	Band-pass Filter
CANOPUS	Canadian Auroral Network for the OPEN Program Unified Study
CARISMA	Canadian Array for Realtime InvestigationS of Magnetic Activity
CASSIOPE	CAScade, Smallsat and IOnospheric Polar Explorer
CE	Common Era
CSA	Canadian Space Agency
CSSDP	Canadian Space Science Data Portal
CubeSat	A standard for nanosatellites
CVCM	Collected Volatile Condensable Materials
DAC	Digital to Analog Converter
DHU	Data Handling Unit
e-POP	Enhanced Polar Outflow Probe
EMF	Electromotive Force
ESA	European Space Agency

Ex-Alta 1	Experimental Albertan #1 CubeSat
EUV	Extreme Ultraviolet
FAC	Field-Aligned Current
FAI	Fast Auroral Imager
FDAM	University of Alberta Facility for Data Analysis and Modeling
FET	Field Effect Transistor
FFT	Fast Fourier Transform
FIR	Finite Impulse Response
FPGA	Field Programmable Gate Array
GBO	Ground Based Observatory
GEI	Geocentric Equatorial Inertial
GPS	Global Positioning System
I/V	Current-to-Voltage
IGRF	International Geomagnetic Reference Field
LEO	Low Earth Orbit
LSB	Least Significant Bit
MagCon	Magnetospheric Constellation
MGF	Magnetic Field Experiment
MMS	Magnetospheric Multiscale Mission
Nadir	Coordinate defined by the direction of gravity (colloquially equivalent to ‘down’)
NASA	National Aeronautics and Space Administration
NRCan	National Resources Canada
NRCSD	NanoRacks CubeSat Deployer
NSERC	National Science and Engineering Research Council

PCB	Printed Circuit Board
PEEK	Polyetheretherketone
PGSD	Alexander Graham Bell Canada Graduate Scholarships-Doctoral Program
PPS	Pulse Per Second
RLC	Resistor, Inductor, Capacitor time constant
RMS	Root Mean Square
RPS	Revolutions Per Second
SMILE	Small Magnetometer In Low-Mass Experiment
SOSMAG	Service Oriented Spacecraft Magnetometer
THEMIS	Time History of Events and Macroscale Interactions during Substorms
TML	Total Mass Loss
V/I	Voltage-to-Current

Chapter 1: Introduction

1.1 Motivation

A growing body of research shows the ongoing toll of space weather effects on modern technological infrastructure such as communication satellites, GPS navigation systems, and electrical networks ranging from accelerated aging to critical failures. The European Space Agency Space Situational Awareness Program defines space weather operationally as "the environmental conditions in Earth's magnetosphere, ionosphere and thermosphere due to the Sun and the solar wind that can influence the functioning and reliability of space borne and ground-based systems and services or endanger property or human health".[1] Space weather includes a variety of phenomena resulting from the interaction of the output of the Sun with the Earth's magnetic field including: increased radiation flux experienced by satellites and airplanes, radio signal interference caused by ionospheric irregularities, and currents in terrestrial electrical grids driven by ionospheric currents. For example, the 1859 solar super-storm called the Carrington Event [*Stewart*, 1861] is an oft-cited example of extreme space weather. A large coronal mass ejection struck the Earth causing the largest geomagnetic space weather event in recorded history. Ionospheric currents were so strong that aurorae were visible as close to the equator as Hawaii [e.g., *Kimball*, 1960]. This event caused telegraph systems to shock their operators, triggered electrical fires, and allowed telegraph communication using just the current induced by the aurora [e.g., *Boteler*, 2006]. More recent research and literature illustrates how devastating such an event could be to modern technological infrastructure if it were to occur in the modern era and impact infrastructure such as satellite communication, GPS navigation systems, and electrical power distribution. A 2013 report by Lloyd's [*Maynard et al.*, 2013] estimated the cost of a modern Carrington Event at $0.6 - 2.6 Trillion USD in the United States alone. In July 2012, a coronal mass ejection considerably larger than that which is believed to have caused the Carrington Event narrowly missed Earth [*Baker et al.*, 2013].

While only a few extreme events such as the Carrington storm have ever been observed, more frequent and more moderate space weather can also have a variety of negative impacts. Some examples are shown schematically in Figure 1-1. Geomagnetic disturbances can induce current

[1] http://www.esa.int/Our_Activities/Operations/Space_Situational_Awareness/Space_Weather_-_SWE_Segment

flow in terrestrial electrical power distribution systems causing premature aging of transformers [*Koen and Gaunt*, 2003] or even taking large sections of the electric power grid offline such as occurred in the 1989 Hydro-Quebec blackout [*Boteler et al.*, 1998]. Similarly, geomagnetic disturbances can drive telluric currents in pipelines causing accelerated corrosion [*Gummow*, 2002]. Disturbed ionospheric conditions caused by precipitating auroral electrons or the transport of dense dayside sun-lit plasma can cause multipath interference (scintillation) of the radio signals required for Global Positioning System (GPS) and degrade or interrupt service [*Basu et al.*, 2001]. A variety of space radiation and satellite charging effects, particularly in the Earth's Van Allen radiation belts, are correlated with operational anomalies of spacecraft [e.g., *Baker*, 2000]. Space weather can also affect the commercial airline industry by degrading avionics and contributing to increased total radiation dose of the flight crew. This is particularly an issue for long-haul routes which travel over the poles crossing the auroral oval [e.g., *Jones et al.*, 2005].

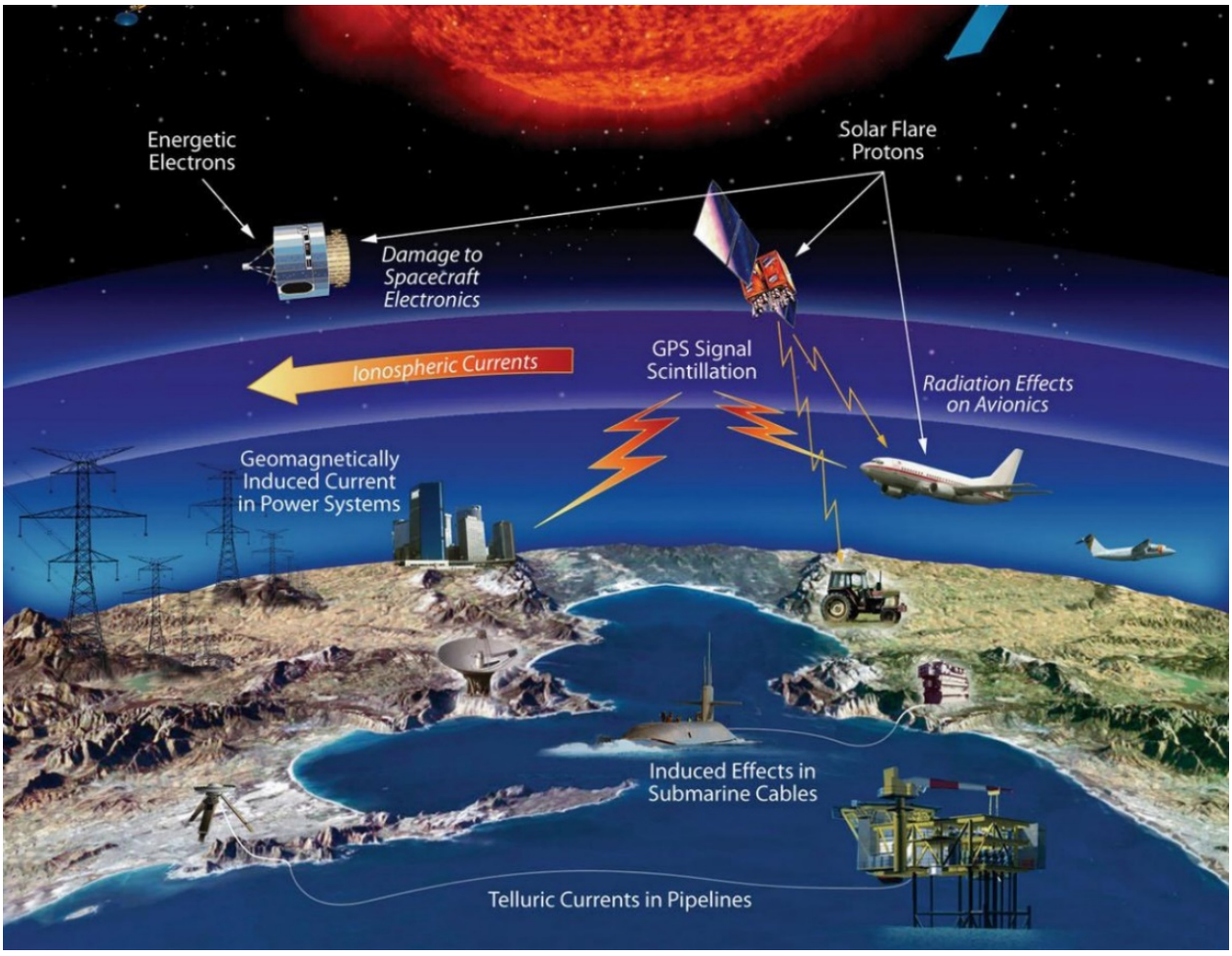

Figure 1-1: Space weather impacts on humans and technology on the ground, in the air, and in space. Image credit: NASA https://www.nasa.gov/sites/default/files/thumbnails/image/faq13.jpg

The prediction of space weather and the future mitigation of space weather effects requires a better understanding of the physical processes that cause these phenomena. This necessitates more comprehensive experimental studies of the magnetic field and plasma dynamics in near-Earth space. Fluxgate magnetometers have played, and will continue to have in the future, a vital role for providing these measurements. The designs, instrument improvements, and analysis techniques described in this thesis help ensure that high fidelity magnetic field measurements are available for future space physics research.

1.2 Thesis Scope and Overview

The primary and substantive research presented in the thesis comprise a compilation of four journal articles describing advances and applications of fluxgate magnetometers and magnetic field data for space physics. Fluxgate magnetometers are a core and essential tool for solar-terrestrial research and the monitoring and forecasting of space weather. They provide high precision measurements of the Earth's magnetic environment, can be used to infer the currents which transport momentum and energy through the coupled magnetosphere-ionosphere (M-I) system, and can contribute to interpreting charged particle dynamics. The remainder of Chapter 1 provides introductory context for the thesis research, briefly reviews the near-Earth space environment, describes some of the physical processes which transport energy and momentum through this system, examines the role of magnetic field measurements in space physics research, reviews the principles of a fluxgate magnetometer, discusses the emergence of multi-point spacecraft constellation concepts for future space physics research, and provides an example of a future application for the instruments presented here.

Chapter 2 describes the MaGnetic Field (MGF) experiment fluxgate magnetometer which was developed for the Enhanced Plasma Outflow Probe (e-POP) payload [*Yau and James*, 2015] on the multi-purpose CASSIOPE small satellite mission sponsored by the Canadian Space Agency (CSA). CASSIOPE/e-POP was launched on September 29, 2013 and the MGF instrument has since produced three years of data. This chapter was published in Space Science Reviews as Wallis et al. [2015].

Chapter 3 presents the design and development of a miniature fluxgate magnetometer to be deployed on a 60 cm deployable boom suitable for use on a CubeSat nanosatellite platform. The instrument will provide high-fidelity magnetic field measurements on a CubeSat. This will enable

future low-cost constellation missions carrying such instruments to investigate the spatial scale and temporal variability of auroral field-aligned currents. This chapter has been published in the Journal of Geophysical Research: Space Physics as Miles et al. [2016].

Chapter 4 investigates constructing the mechanical elements of a fluxgate sensor from new more robust, lower-cost, and easier to machine engineering plastics rather than traditional machinable ceramic without compromising the sensor's thermal gain stability. A novel, low-cost laboratory based calibration procedure is used to compare the performance of six geometrically and electrically matched fluxgate sensors in which the material used to support the windings and the sensor base is varied. The thermal gain dependence of the fluxgate sensors is measured at the part-per-million per degree Celsius level in a typical magnetically noisy university laboratory. The procedure will be useful for future University-built low-cost space missions, such as CubeSats, which may not be able to gain ready access to a dedicated magnetic calibration facility. This chapter is in preparation for publication in Geoscientific Instrumentation, Methods and Data Systems as Miles et al. [2017b].

Chapter 5 presents a case study of dynamic discrete arc aurora observed during a near magnetic conjunction between e-POP and the European Space Agency Swarm A and C spacecraft [*Friis-Christensen et al.*, 2008]. High cadence auroral imaging and magnetic data are used to examine a dynamic dual-arc for evidence of Alfvén waves and signatures of modulation by the Ionospheric Alfvén Resonator. This chapter is in preparation for publication in Geophysics Research Letters as Miles et al. [2017a].

Chapter 6 summarises the results of this thesis and considers future work in the form of a potential sub-orbital sounding rocket application of the instruments and techniques described herein.

1.3 The Solar-Terrestrial Connection

"… the domain of space weather is vast – extending from deep within the Sun to far outside the planetary orbits – and the physics complex – including couplings between various types of physical processes that link scales and domains from the microscopic to large parts of the solar system. Consequently, advanced understanding of space weather requires a coordinated international approach to effectively provide awareness of the processes within the Sun–Earth system through observation-driven models." [*Schrijver et al.*, 2015]

A 2015-2025 roadmap [*Schrijver et al.*, 2015] commissioned by the Committee on Space Research (COSPAR) and the International Living With a Star (ILWS) program makes several recommendations on how the international scientific community should work to understand space weather and mitigate its affects. Foremost of these, is a recommendation to focus on "observation-based modeling throughout the Sun–Earth system."

Figure 1-2 illustrates a coronal mass ejection from the sun colliding with the Earth's magnetic field. This is a dramatic example of the broader and ongoing interaction between the magnetised plasma (the solar wind) emitted by the sun and the near-Earth region dominated by the Earth's magnetic field (the magnetosphere). The Earth's magnetic field extends from the Earth's core into space and, by interaction with the solar wind, is dynamically compressed on the sun-facing dayside and is stretched to extend in the opposite night-side to form the tear-shaped magnetosphere cavity.

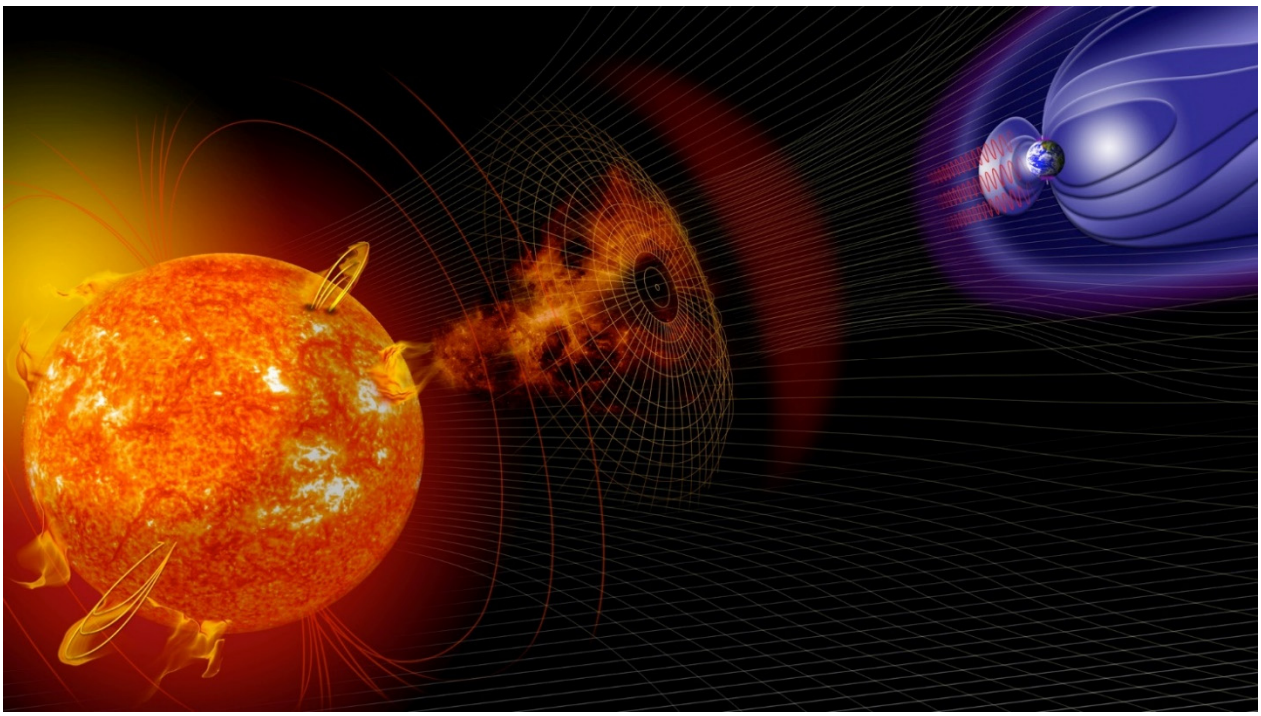

Figure 1-2: Interaction of a coronal mass ejection from the sun with the Earth's magnetosphere. Image credit: NASA. https://www.nasa.gov/sites/default/files/525022main_faq12_0.jpg

Figure 1-3 shows examples of how the Earth's magnetic field can connect to that of the solar wind, via the process of magnetic reconnection, driving a global-scale plasma convection process referred to as the Dungey cycle [*Dungey*, 1963]. A southward interplanetary magnetic field (IMF) arrives anti-parallel to the Earth's dayside magnetic field allowing the two fields to (re)connect in the process of magnetic reconnection. The resulting highly kinked magnetic field line is pulled

straight via magnetic tension and then dragged anti-sunward over Earth's pole by the action of the solar wind. Field lines anchored in the northern and southern hemispheres but connected to the IMF are stretched by the solar wind flow, eventually convecting towards midnight to become anti-parallel in the night-side equatorial plane. This process forms the magnetotail where the stretched anti-parallel field lines can (re)connect to form newly closed magnetic flux. The closed magnetic field lines convect Earth-wards restoring the nominally dipole terrestrial magnetic field and completing the cycle. Conversely, northward IMF arrives parallel to the Earth's dayside magnetic field and it held off by magnetic pressure. However, magnetic reconnection can still occur at high latitudes on the night-side typically driving convection in the polar cusp.

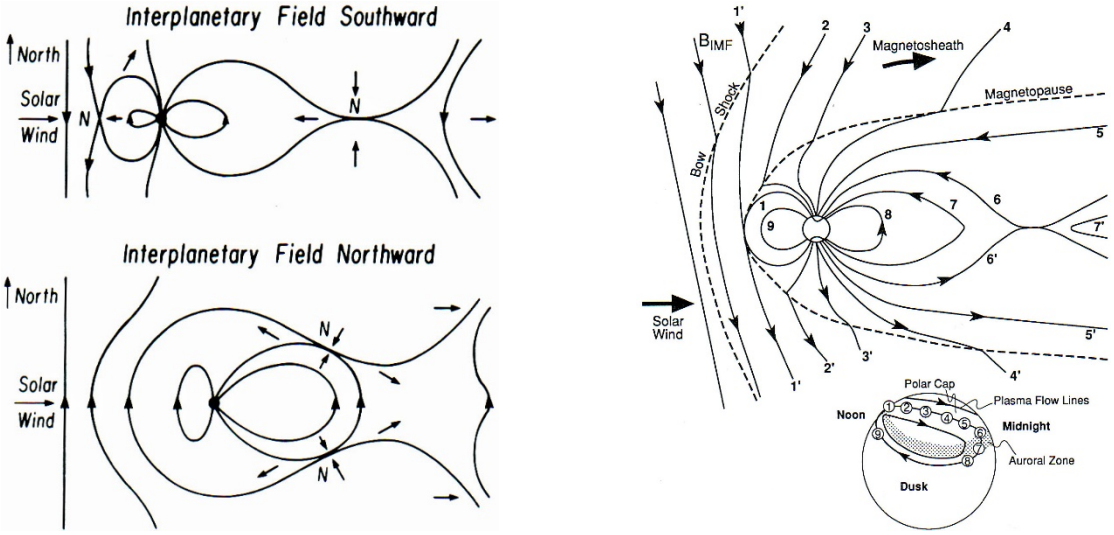

Figure 1-3: Schematic of solar-terrestrial coupling and magnetic reconnection. (left) Simplified interaction of the interplanetary magnetic field (IMF) and the Earth magnetic field showing dayside re-connection with southward IMF and pile-up with northward IMF. (right) Anti-sunward motion of plasma over the pole due to southward IMF driving a convection cells in the auroral region. From Kivelson and Russell [1995].

Figure 1-3 (right) shows the sequence of magnetic field line transport during the Dungey cycle for southward IMF and the resulting plasma transport by the reconnection driven convection cells created in the Earth's auroral region and polar cap. Magnetic reconnection thereby provides a power source for Earth's space weather by providing a mechanism to drive energy into the Earth's magnetosphere leading to a variety of complex interactions and phenomena in near-Earth space including geomagnetic storms and substorms.

1.4 Near Earth Space Environment

Near-Earth space, above the neutral atmosphere, contains a variety of plasma regimes composed primarily of hydrogen ionised into its constituent protons and electrons with a small addition of

heavier ions such as Helium. Typical densities vary from ~10^7 m^{-3} in the solar wind to ~10^{12} m^{-3} in the ionosphere. The plasma is influenced by local magnetic field, which ranges in strength from ~10 nT in the solar wind to ~10^4 nT at the ionosphere. Figure 1-4 illustrates the major regions of the Earth's magnetosphere, the principle currents, and the general magnetic field topology. The incoming solar wind not only interacts with the Earth's magnetic field through magnetic reconnection but also compresses the dayside field and forms the magnetopause, which separates the region dominated by the Sun's output and the region dominated by the Earth's magnetic field. Inside the magnetopause are two torus-shaped regions called the Van Allen radiation belts. The outer belt is formed mostly by energetic electrons and is typically found at geocentric altitudes of about 4-7 Earth Radii (R_E) and its inner edge is thought to track the plasmapause [*Li et al.*, 2006]. The inner belt is comprised of mostly energetic protons, is typically observed at geocentric distances of at 1.5-3 R_E and resides within the plasmasphere. The plasmasphere is a region of denser low-energy plasma between the ionosphere and a sudden order-of-magnitude drop in plasma density called the plasmapause. Inside the plasmasphere, the field lines co-rotate with the Earth, higher densities being generated by equilibrium with an ionospheric plasma source at the ends of the field lines.

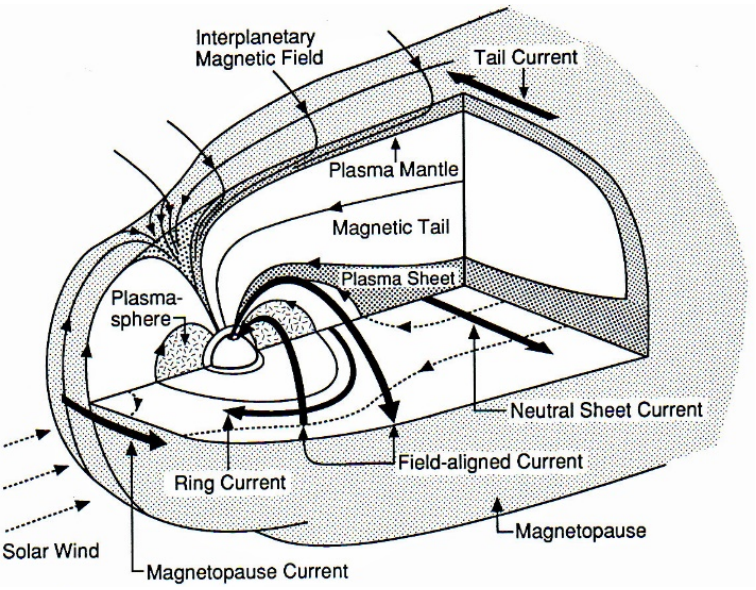

Figure 1-4: Regions of the Earth's magnetosphere, the principle currents, and field topology. From Kivelson and Russel [1995].

The ionosphere is the region above ~60 km where, due to the presence of free electrons, conductivity is high enough to influence the propagation of radio signals [*Ratcliffe*, 1972]. The ionosphere is created primarily by the ionisation of the tenuous upper atmosphere by Extreme

Ultraviolet (EUV) solar radiation. Figure 1-5 shows a nominal ionospheric density altitude profile illustrating how the electron density varies by orders of magnitude and separates the ionosphere into the distinct D-, E-, and F-layers. The altitudes, densities, and sharpness of layers varies with a variety of factors including local time and solar activity.

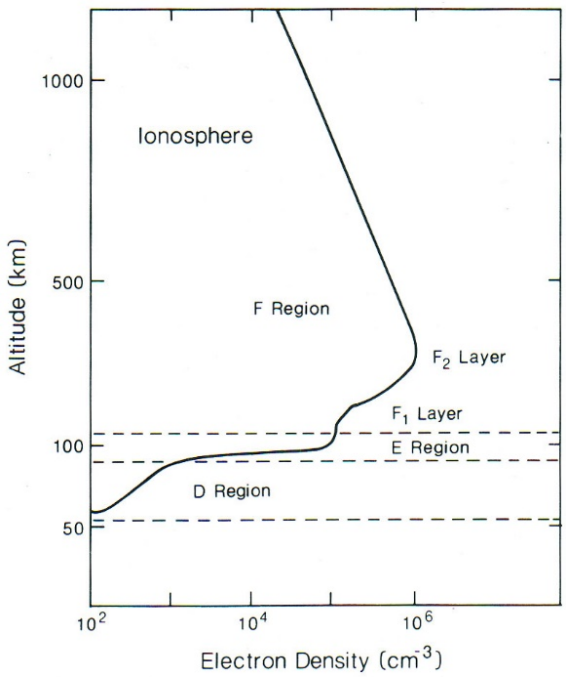

Figure 1-5: Nominal ionosphere density profile. From Kivelson and Russel [1995]

The high conductivity of the E-layer ionosphere forms an electromagnetic boundary separating the neutral atmosphere from the ionised and highly conducting magnetosphere above. However, energy from the solar wind that is captured and stored in the magnetosphere can be coupled to the ionosphere via current systems aligned with the background magnetic field in the form of field-aligned currents (FACs). Figure 1-6 shows the large-scale field-aligned Region 1 and Region 2 currents driven in the magnetosphere and which are closed in the ionosphere by perpendicular Pedersen currents flowing along the ionospheric electric field. Due to the charged particle dynamics there are also $\boldsymbol{E} \times \boldsymbol{B}$ driven Hall currents in the ionosphere. Different types and scales of field-aligned currents exist with different charge carriers and energies. Visible aurora are typically linked to electrons in the keV range [e.g., review by *Rees*, 1969].

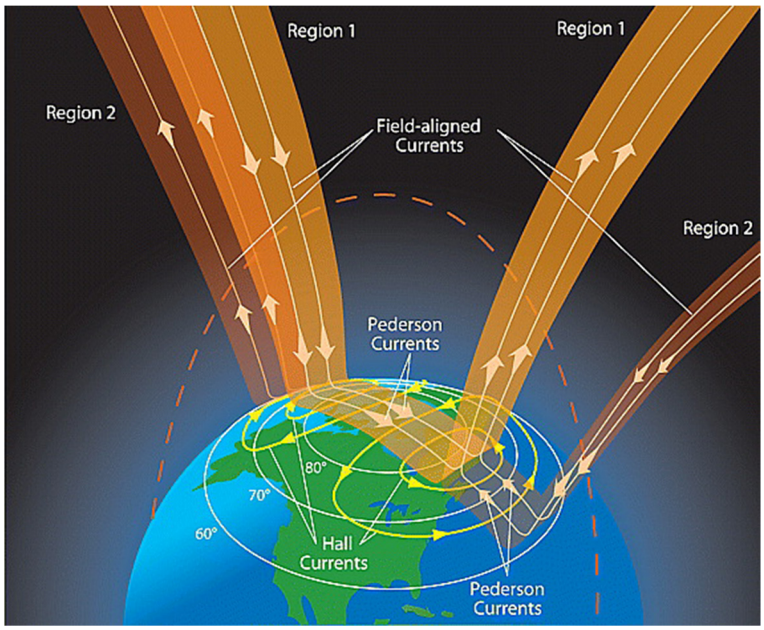

Figure 1-6: Magnetosphere-ionosphere coupling via field-aligned Region 1 and 2 and Pederson and Hall currents in the ionosphere. Reproduced from Le et al. [2010]

1.5 Alfvén Waves

Alfvén waves, first described by Hanes Alfvén and for which he was awarded the Nobel Prize, are a type of magnetohydrodynamic wave which propagates along a magnetic field line [e.g., *Alfvén and Falthammar*, 1963]. For the purposes of this thesis, we are interested in Alfvén waves due to their potential role in carrying field-aligned currents and their potential role in auroral electron acceleration. Many processes have been proposed to explain the acceleration of electrons required to create the aurora. These can be divided [e.g., *Mottez*, 2015] into acceleration by a quasi-static electrical potential drop [e.g., *Evans*, 1974] and acceleration by interaction with Alfvén waves [e.g., *Lysak*, 1990]. Historically, discrete arc aurora, such as those examined in Chapter 5, were thought to be related to quasi-static electric fields [e.g., *Swift*, 1981]. However, electron acceleration by interaction with Alfvén waves is increasingly invoked to explain especially small scale and dynamic aurora [*Stasiewicz et al.*, 2000] and multi-arc aurora [*Trondsen et al.*, 1997].

Alfvén's model for wave generation is shown qualitatively in Figure 1-7 based on the propagation of a magnetic field perturbation resulting from the displacement of a volume of plasma. This is a special case of a more general wave mode; however, Alfvén's model is useful for visualising the process and can be summarised as follows [following *McPherron*, 2005]:

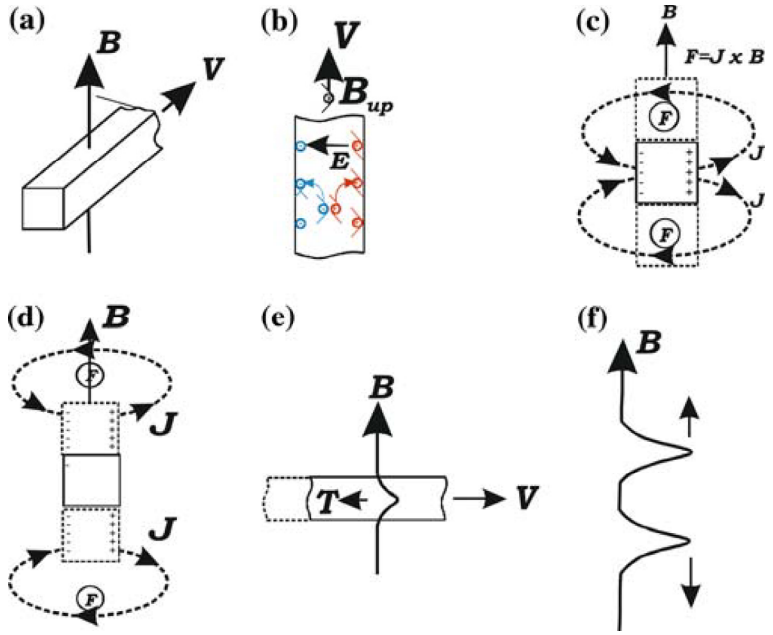

Figure 1-7: Creating an Alfvén wave through the displacement of a volume of plasma frozen to a magnetic field. From McPherron [2005] following Alfvén and Falthammar [1963].

A volume of highly conducting plasma in a magnetic field $\boldsymbol{B}$ is displaced with velocity $\boldsymbol{V}$ (Figure 1-7 a). The charges q of the particles in the plasma experience a Lorentz force $\boldsymbol{F} = q(\boldsymbol{V} \times \boldsymbol{B})$ as they move. The opposite charges of the free electrons (blue) and protons (red) causes them to separate, the electrons moving left and the protons moving right (Figure 1-7 b). This charge separation creates an electric field $\boldsymbol{E}$ perpendicular to both $\boldsymbol{V}$ and $\boldsymbol{B}$. In a finite volume, the charges could not leave the plasma volume and eventually they would reach an equilibrium where the Lorentz force matches the electric force such that $\boldsymbol{E} = -\boldsymbol{V} \times \boldsymbol{B}$. However, in a plasma, charge can move through the surrounding volume to cancel out the charge separation (Figure 1-7 c). This current, $\boldsymbol{J}$, exerts a force per unit volume $\boldsymbol{F} = \boldsymbol{J} \times \boldsymbol{B}$ as it moves across the magnetic field. Consequently, the plasma volumes immediately above and below the original volume element to move in the direction of the original displacement (Figure 1-7 d).

The same process now applies to the two new moving volumes of plasma causing the original displacement to propagate in both directions parallel to the magnetic field. The volumes of plasma are frozen-in to the magnetic field so their displacement bends the field creating a restoring force through magnetic tension (Figure 1-7 e). As this process bends and restores volumes of plasma above and below the original volume the resulting perturbation and restoration of the magnetic field creates a pulse that propagates along the magnetic field – an Alfvén wave (Figure 1-7 f).

High conductivity in the ionosphere can reflect earthward travelling Alfvén waves [e.g., *Hughes*, 1974] although the reflection efficiency is complex and frequency dependent [e.g., *Lessard and Knudsen*, 2001]. Conversely, Alfvén waves travelling away from the Earth can reflect from the steep gradient in the Alfvén speed $V_A = B/(\mu_0\rho)^{1/2}$ profile due to the varying plasma mass density (ρ) and magnetic field strength (B) along the magnetic field line. Together, these can create the top and bottom of a resonant cavity which can trap Alfvén waves creating the Ionospheric Alfvén Resonator [*Belyaev et al.*, 1990; *Lysak*, 1990]. It has been argued that the Ionospheric Alfvén Resonator can be excited both by Earthward travel waves generated in the magnetosphere [e.g., *Prikner et al.*, 2004] and by lightning on the ground [e.g., *Sukhorukov and Stubbe*, 1997].

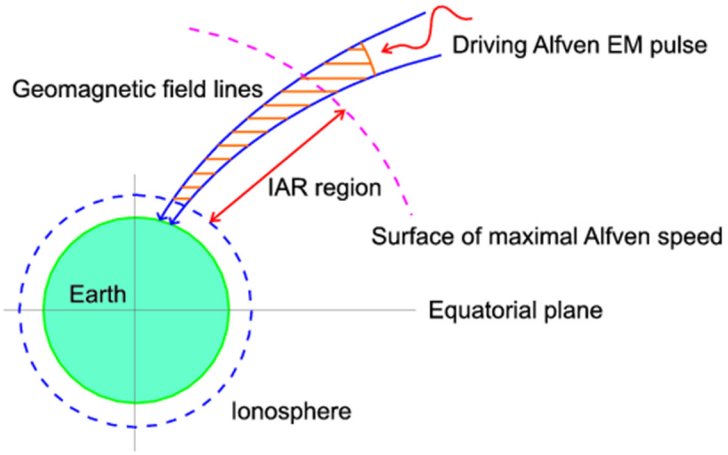

Figure 1-8: Schematic illustration of the Ionospheric Alfvén Resonator (IAR) formed between the ionosphere and the peak in Alfvén speed. Image credit: University of Alberta Facility for Data Analysis and Modeling (FDAM)

1.6 The Role of Magnetic Field Measurements in Auroral Space Research

Aurora have likely been observed for as long as humans inhabited the polar regions. Descriptions of lights in the sky matching the aurora are found throughout the earliest human written works including the Old Testament, early Greek literature, and Chinese literature dated to earlier than 2000 BCE [*Kivelson and Russell*, 1995]. Similarly, references to the existence of the Earth's magnetic field and its utility for marine navigation by compass needle have been found as early as ~1100 CE [*Kivelson and Russell*, 1995]. The link between auroral phenomena and the magnetic fields was hinted at in 1716 when Edmond Halley observed aurora which appeared aligned with the Earth's magnetic field lines; in 1722 George Graham observed magnetic fluctuations with his compass which were later correlated to observations of the aurora [*Moldwin*, 2008]. Kristian Birkeland robustly established the link between magnetic field perturbations and the aurora

through his third arctic expedition, the Norwegian Aurora Polaris Expedition from 1902 to 1903. He made extensive observations of perturbations to the Earth's magnetic field (Figure 1-9) during auroral displays [*Birkeland*, 1908]. Based on these observations, he argued that the aurora must be related to large currents flowing parallel to the nearly vertical polar magnetic field.

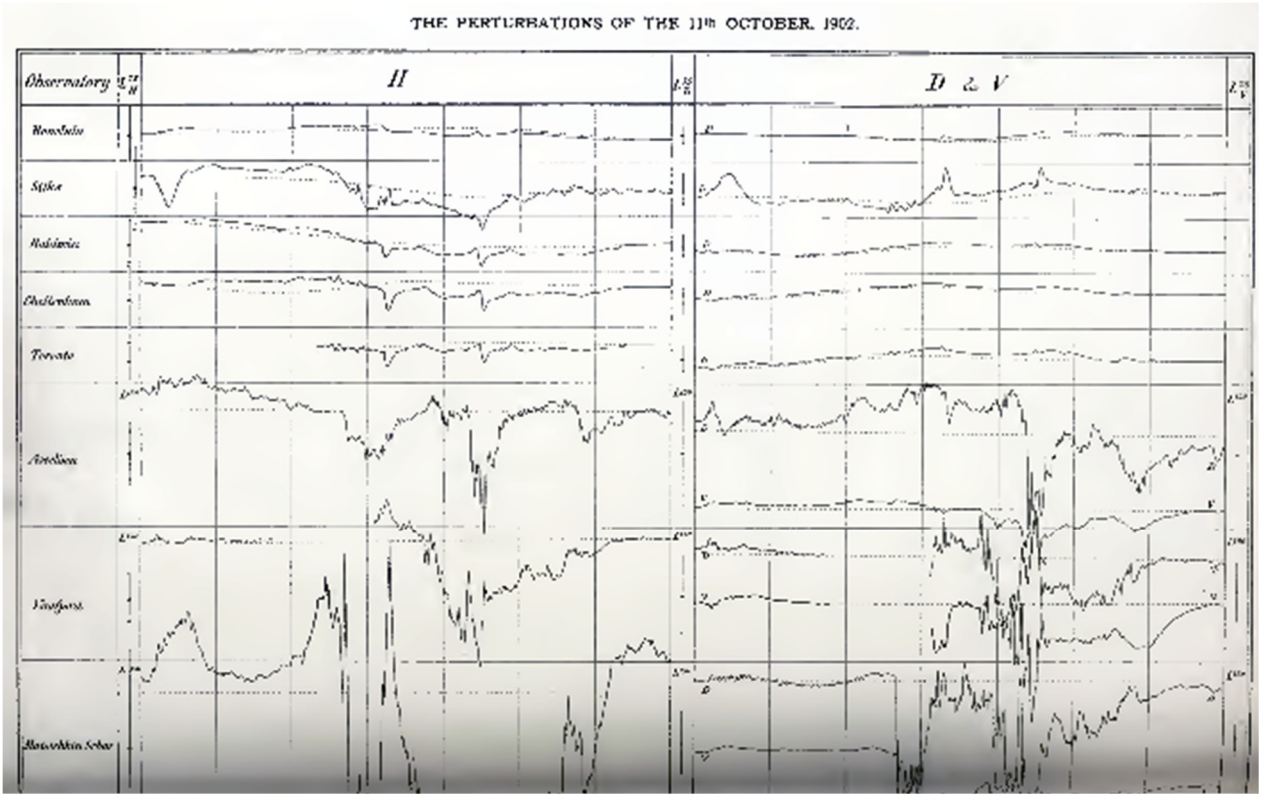

Figure 1-9: Early magnetic and auroral observations. Magnetic perturbations on October 11, 1902 from the Norwegian Aurora Polaris Expedition [Birkeland, 1908].

These observations were influential on another Norwegian scientist, Carl Størmer [*Størmer*, 1935, 1937], who modelled the motion of charged particles within the Earth's magnetic field and exploited the emergence of practical cameras to take photographs of the aurora and estimate their altitude (Figure 1-10).

Figure 1-10: Prof. Carl Størmer and assistant photographing the aurora in 1910. http://www.nb.no/cgi-bin/galnor/gn_sok.sh?id=110728&skjema=2&fm=4

The advent of spacecraft magnetometry allowed these currents to be indirectly investigated in-situ by observing the perturbations of the background magnetic field. Iijima and Potemra [1976] used perturbations to the cross-track magnetic field, nominally corresponding to a FAC, measured by the Triad satellite during quiet conditions to build up an average FAC map reproduced as Figure 1-11.

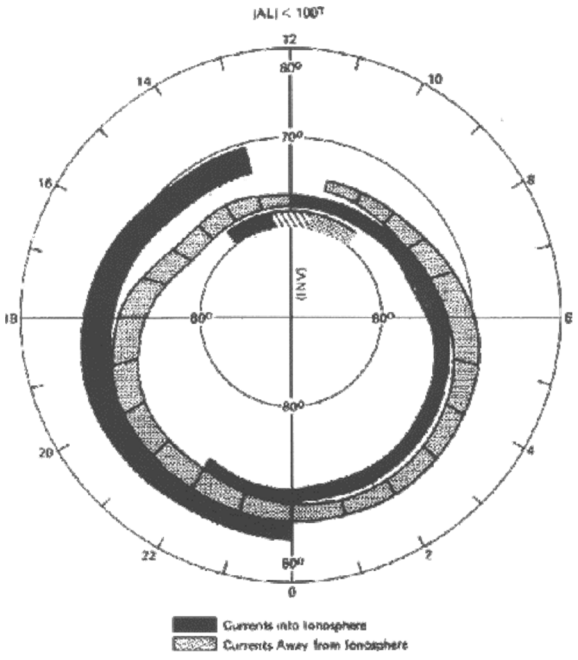

Figure 1-11: Historical spacecraft observations of field-aligned current. Large scale field-aligned current systems as measured by Iijima and Potemra [1976] using Triad

The same general topology of upward and downward current regions has been widely reproduced, including recently by the Active Magnetosphere and Planetary Electrodynamics Response Experiment (AMPERE) experiment [*Anderson et al.*, 2000; *Waters et al.*, 2001] using the navigational magnetometer on the Iridium communication satellite network comprised of over 70 satellites (Figure 1-12).

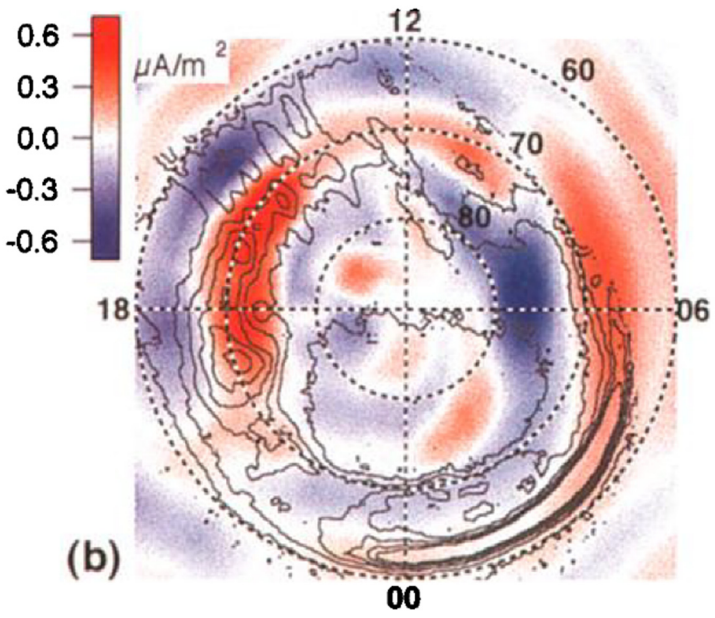

Figure 1-12: Modern spacecraft observations of field-aligned current. Large scale field-aligned current systems as measured by Waters et al. [2001] using AMPERE. Blue denotes downwards going current and red denotes upward current.

Keiling et al. [2003] performed a statistical study using one year of data from the Polar spacecraft at altitudes of 25,000 to 38,000 km but focusing on energy transport by Alfvénic wave Poynting flux into the auroral ionosphere. Keiling et al. [2003] used auroral images from Polar (Figure 1-13 A) averaged over one year to create a statistical average auroral intensity map (Figure 1-13 B). Perturbations to the electric field, $\boldsymbol{\delta E}$, and the magnetic field, $\boldsymbol{\delta B}$, where then used to calculate the wave Poynting flux ($\boldsymbol{S} = \boldsymbol{\delta E} \times \boldsymbol{\delta B}/\mu_0$) to estimate the average energy transported by waves at Polar altitudes in the field aligned downward (Figure 1-13 C) and upwards (Figure 1-13 D) directions.

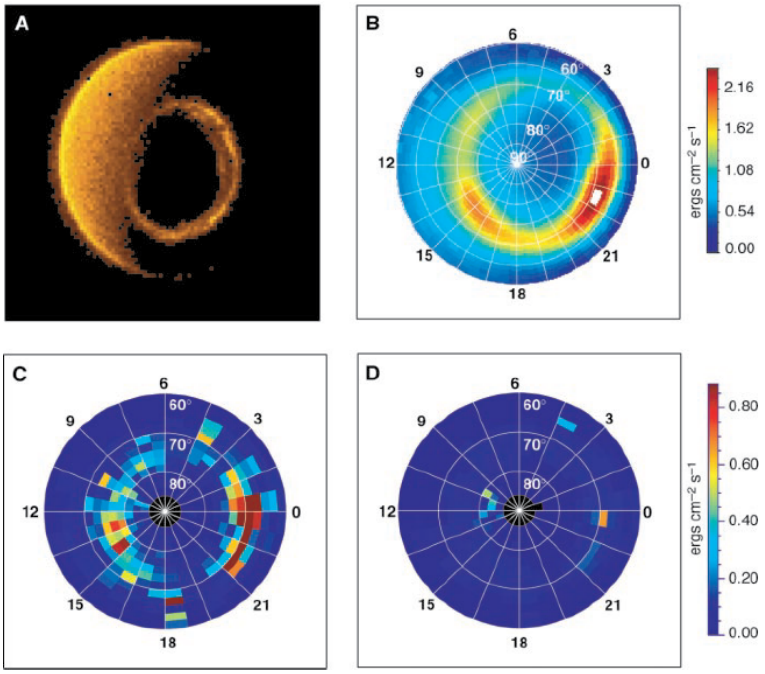

Figure 1-13: Statistical distribution and wave energy transfer of the aurora. (A) Example auroral image from the Polar satellite. (B) Average intensity from auroral imaging. (C) Average downwards wave Poynting flux. (D) Average upwards wave Poynting flux. Reproduced from Keiling et al. [2003].

Keiling et al. [2003] observed significantly more downward Alfvén wave Poynting flux than upwards resulting in a net average transfer of energy towards the Earth, the distribution of which matched the observed average auroral intensity. Further, this Alfvén wave Poynting flux exceeded energy levels of 5 ergs per square centimeter per second which is above the threshold of ~1 erg per square centimeter per second thought necessary for electron beams to produce visible aurora [*Keiling et al.*, 2003].

Ongoing research continues to study the role and relative importance of static field-aligned potential drops and Alfvén waves in auroral electron acceleration and magnetosphere-ionosphere coupling. Magnetic field measurements, such as those provided by the fluxgate magnetometers described in this thesis, will be an essential part of this research through their deployment on the ground, in-space, and on sub-orbital flights of high-altitude balloons and sounding rockets.

1.7 Fluxgate Magnetometer Instruments

Fluxgate magnetometers are an essential tool for solar-terrestrial research and monitoring or forecasting space weather. They provide high precision measurements of the Earth's magnetic fields and can be used to infer the currents that transport energy and momentum through the magnetosphere and ionosphere. As described by Snare [1998], fluxgate magnetometers were first

developed by Aschenbrenner and Goubau [1936] and have been used for a variety of applications including the military detection of submarines [*Vacquier*, 1993] and the mapping of ocean floor spreading [*Vacquier et al.*, 1961]. When combined with electric field measurements using magnetotellurics [*Cagniard*, 1953], magnetic field measurements such as those from fluxgate magnetometers can be used to image the Earth's subsurface by inferring electrical conductivity based on surface measurements of natural geomagnetic and geoelectric signals.

Fluxgate magnetometers sense the local magnetic field as a consequence of Faraday's law. Following Ripka [2001], for a coil of wire with a high magnetic permeability core, a changing magnetic flux Φ will induce a voltage V_i related to the number of wire turns N the area of the turns A the magnetic constant μ_0 the relative permeability of the core μ_r and the magnetic field H.

$$V_i = \frac{d}{dt}\Phi = \frac{d}{dt}(NA\mu_0\mu_r H).$$

Observing that A, μ_r, and H can be time varying and considering each separately gives a generalised induction equation

$$V_i = (NA\mu_0\mu_r)\frac{dH}{dt} + (N\mu_0\mu_r H)\frac{dA}{dt} + (NA\mu_0 H)\frac{d\mu_r}{dt}.$$

The dH/dt term is the basis of an induction coil magnetometer, the dA/dt is typically either negligible or an error term, and the $d\mu_r/dt$ term allows the sensing of H and is the basis of the fluxgate action. A high-permeability core will normally concentrate the local magnetic field enhancing the flux through a sense coil. Modulating μ_r will modulate the flux carried in the core, and hence the flux surrounded by the sense coil. Figure 1-14 (left) shows schematically how the modulation of μ_r can be achieved. A periodic drive current I_{drive} is forced into a coil of wire surrounding the core. I_{drive} creates new magnetic flux which exceeds the carrying capacity of the core forcing it into magnetic saturation and abruptly changing μ_r. The electromotive force from the $d\mu_r/dt$ induction term then creates V_i which is a function of the external magnetic field H. However, changes in the coil geometry, which can occur with temperature, affect the scaling of the instrument requiring calibration and mitigation as described in Chapter 4.

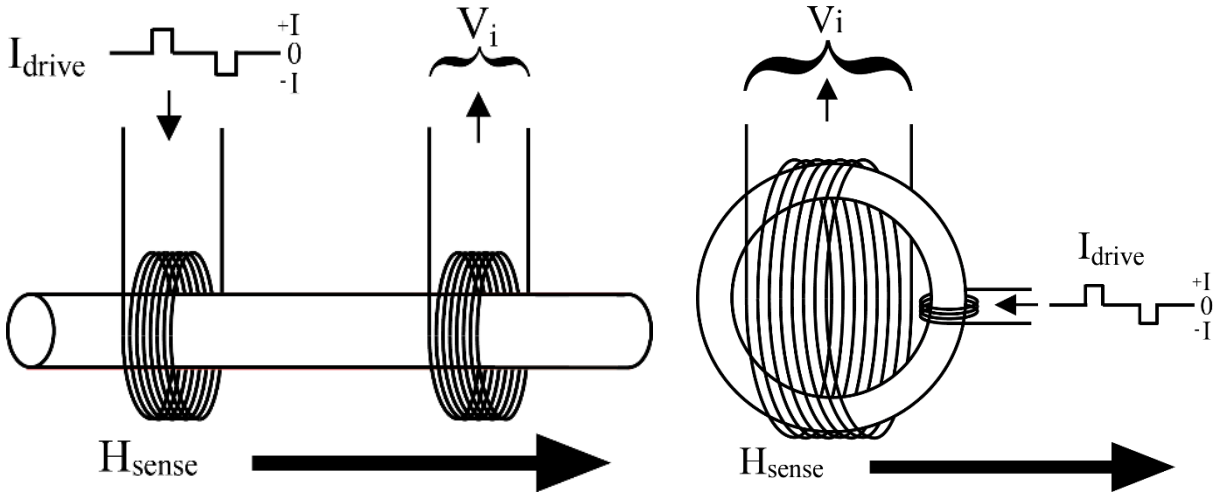

Figure 1-14: Schematic illustration of a fluxgate magnetometer sensor constructed from a rod-core (left). Same but with the core formed into a toroid creating a ring-core sensor (right). Adapted from Miles [2013].

Unfortunately, the assembly illustrated in Figure 1-14 (left) is also an electrical transformer that will couple the I_{drive} signal into the sensor's output V_i. Fluxgate sensors typically use other geometries to minimize this transformer action via symmetry while preserving the fluxgate action. For the instruments described in this thesis, a high-permeability foil is formed into a circle to create a ring-core sensor (Figure 1-14 right). The magnetic flux created by I_{drive} is primarily contained within the, now toroidal, drive winding. Flux, which leaks from the drive winding and is picked up by the sense winding, is cancelled by the antiparallel flux from the other half of the symmetric ring-core reducing the drive signal coupling. Figure 1-15 shows a physical implementation of a flux-gate ring-core such as is used in several of the instruments described in this thesis [*Narod and Bennest*, 1990; *Wallis et al.*, 2015]

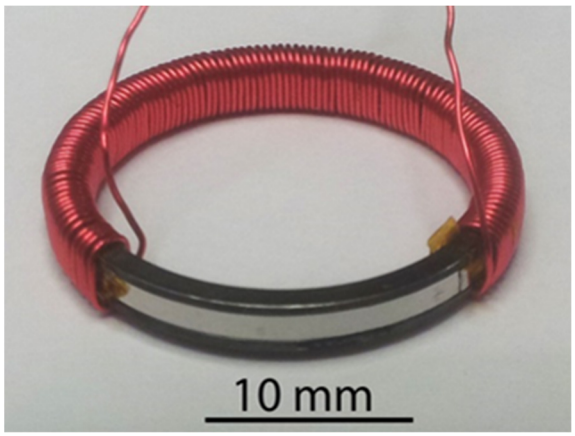

Figure 1-15: Partially disassembled 25.4 mm fluxgate ring-core. The permalloy foil is high-gloss grey, the Inconel bobbin is matte black, the tan insulating Kapton layer and red enameled copper wire have been partially removed for the picture.

The 6-81 permalloy foil used as the high permeability element (Figure 1-15, high-gloss grey) is mechanically supported by an Inconel bobbin (matte black). Kapton (tan) electrically isolates the magnetic core and bobbin from the toroidal winding of enameled copper wire (red). The Kapton tape and toroidal drive winding have been partially removed for Figure 1-15.

The fluxgate instruments described in this thesis all use variations of the classic second harmonic fluxgate design illustrated by Ripka [2001] in Figure 1-16. A common time base (GEN) creates a drive signal at frequency f that is power amplified (PA) and used to saturate the fluxgate core. The resulting induced voltage (V_i) is power amplified (PA), band-pass filtered around the second harmonic (2f) and then a phase sensitive detector at 2f is used to demodulate the signal before it is low-pass filtered (LP1) and integrated (INT) to create a quasi-dc voltage related to the sensed projection of the magnetic field (H_0).

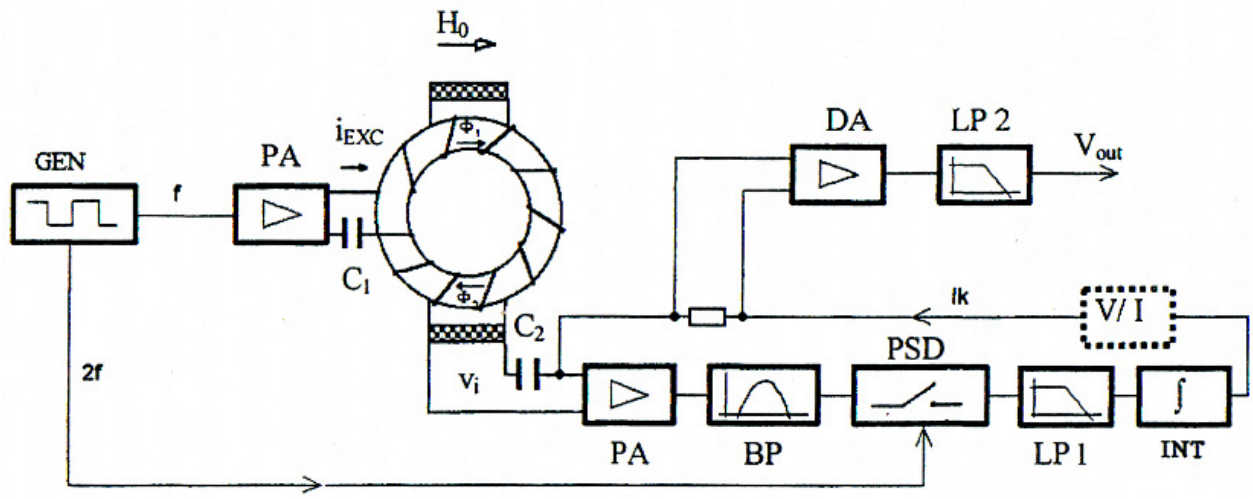

Figure 1-16: Block diagram for a traditional second harmonic fluxgate magnetometer. Reproduced from Ripka [2001].

Global negative magnetic feedback can be added by converting the measured magnetic field into a current (V/I) and either driving it back into the sense winding or into a separate feedback winding. This creates global negative magnetic feedback that will drive the magnetic field within the sense winding towards zero and can be used to linearize and extend the magnetic range of the instrument. Replicating this instrument topology two additional times and arranging the sense windings in three orthogonal directions allows the vector magnetic field to be constructed. Figure 1-17 shows a complete three-axis vector ring-core fluxgate magnetometer sensor as designed for the MAGSAT mission by Acuña et al. [1978]. This design was the starting point for the development of the majority of fluxgate instruments described in this thesis.

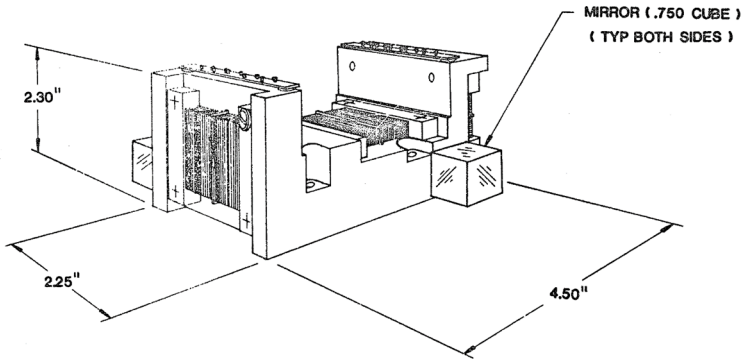

Figure 1-17: A three-axis ring-core fluxgate magnetometer sensor as designed for the MAGSAT mission. Reproduced from Acuña et al. [1978].

1.8 Multi-Spacecraft Constellations

Scientific spacecraft and in-situ space missions are in general expensive and have significant overhead costs in the form of the launch vehicle and the spacecraft bus that generates power, provides command and control, and telemeter data from the science payload back to Earth. Consequently, there is a historical preference for launching a single large and extremely well instrumented spacecraft to make maximum use of the investment. These single spacecraft missions have provided excellent scientific return; however, as a single moving measurement point they influence how space is viewed and have a very limited ability to differentiate between phenomena that vary in space from those that vary in time.

For example, auroral Field-Aligned Currents (FAC) are a long-predicted [*Birkeland*, 1908] and well-established [*Iijima and Potemra*, 1976] phenomenon linking auroral displays to the broader dynamics of Magnetosphere-Ionosphere (M-I) coupling. However, the scale, morphology, and origin of FAC and their relevance to auroral physics remain controversial. The archetypal FAC geometry described by Iijima and Potemra [1978] was based on averages of 439 passes of the Triad spacecraft during weakly disturbed conditions and neglects any small-scale temporal variations (small spatial scales) in the magnetic field in the frame of the Triade spacecraft in low-Earth orbit. This provides a useful picture of the morphology of large-scale (assumed) static FAC but is necessarily incomplete as it averages away small-scale and dynamic phenomena. The same large, quasi-static structures can be reliably and routinely observed by experiments such as AMPERE [*Anderson et al.*, 2000; *Waters et al.*, 2001], which uses the navigational magnetometers on the ~66 Iridium communication spacecraft to estimate the global FAC structure with a higher ~10 minute cadence. AMPERE data have also enabled more sophisticated analyses of FAC spatio-

temporal dynamics [*Murphy et al.*, 2013], which reveals that dynamical evolution can occur on timescales much shorter than the approximately 10-minute revisit time of the spacecraft in each of the Iridium orbital planes.

Modern spacecraft missions have sometimes used a small number of spacecraft, often from a common launch vehicle, to attempt to distinguish between spatial and temporal phenomena and to understand the morphology and coupling between different regions of the Earth's magnetosphere. For example, Gjerloev et al. [2011] used data from the three ST 5 spacecraft in a string-of-pearls configuration (Figure 1-18, left) to study the spatio-temporal characteristics of FAC. Gjerloev et al. [2011] argue that large-scale structures have a dominant role in the transport of energy and momentum. However, they were forced to spin-average their data over ~3-second periods that they acknowledge makes the data questionable for spatial scales below 20 km. They also observe less coherency between the three spacecraft at smaller scales leaving open the possibility of a significant role for dynamic small-scale currents or waves as discussed in Chapter 5. Moreover, ST-5 was a technical demonstration mission and only collected data for three months.

The European Space Agency Swarm mission [*Friis-Christensen et al.*, 2008] uses three spacecraft (Figure 1-18, middle) to avoid some of the limitations of single spacecraft measurements. The Swarm A and C spacecraft are 'side-by-side' separated by only ~1.5° azimuthally cross-track and ~10 seconds along track. Assuming that currents are homogeneous and static on the spatial and temporal separation of the two spacecraft allows the estimation of FAC considering both cross-track and along-track perturbations in the magnetic field by the two spacecraft 'integral method' [*Ritter et al.*, 2013]. However, as shown in Chapters 3 and 5, this separation may still be too large to resolve all relevant waves and currents. Consequently, Swarm A and C may either average away the small-scale dynamic signals or difference signals which sample unrelated plasma regions the result of which can be non-physical and hence might poorly represent FACs including those associated with dynamic auroral features [*Forsyth et al.*, 2017]. This would suggest that either additional spacecraft or smaller separations are required to accurately characterize the spatial and temporal dynamics of FACs connecting the magnetosphere and ionosphere.

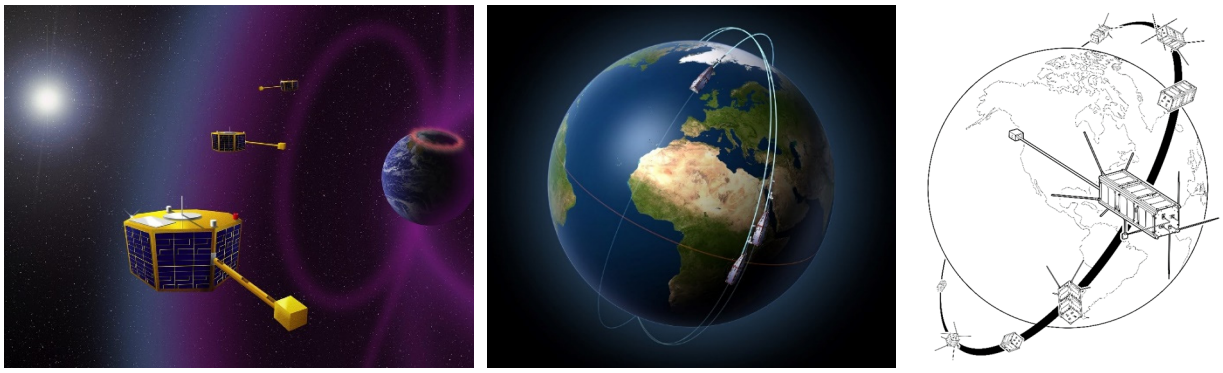

Figure 1-18: Multi-spacecraft constellations. (Left) The NASA ST 5 constellation. Image credit: NASA. https://www.nasa.gov/images/content/137254main_ST5_lg.jpg (Middle) The ESA Swarm satellite constellation. Image credit: ESA http://www.esa.int/images/SWARMs-Orbits-LR,0.jpg (Right) The Framework Seven QB50 CubeSat constellation mission. Image credit: Andy Kale

Of particular interest are instrumentation and analysis approaches that utilise a greater number of spacecraft thereby providing both the necessary coverage and small spatio-temporal separations needed to accurately characterize FACs. However, future constellations of greater numbers of spacecraft will likely require lower resource and lower cost hardware for each spacecraft in order to keep the missions from becoming prohibitively expensive. The upcoming international QB50 mission [Muylaert, et al., 2009] will create a dense, string-of-pearls constellation of ~28 CubeSats each no larger than 10x10x30 cm. There are intrinsic physical limitations imposed on such small platforms such as maximum available solar power. However, miniaturized manufacturing and modern electronics increasingly allow CubeSats to be reasonably well instrumented. For example, the University of Alberta Ex-Alta 1 CubeSat for QB50 carries a multi-needle Langmuir probe, a radiation dosimeter, and the miniature, boom-mounted fluxgate magnetometer described in Chapter 3. Such miniature instruments pose new design challenges to preserve measurement fidelity while shrinking and reducing the mass of the sensors and electronics. New materials, manufacturing processes, and calibration techniques, such as described in Chapter 4, are required to produce multiple small, high-quality instruments at reasonable cost. CubeSats and miniature hardware may be one of the few practical and cost-effective ways to implement the Magnetospheric Constellation (MagCon) type missions of 30 or more spacecraft identified as one of the next critical opportunities to drive scientific discovery by the NASA Heliophysics Science and Technology Roadmap for 2014-2033 [*Heliophysics Roadmap Team*, 2014]

Chapter 2: The Cassiope/e-POP Magnetic Field Experiment (MGF)[2]

2.1 Abstract

Field-aligned currents couple energy between the Earth's magnetosphere and ionosphere and are responsible for driving both micro and macro motions of plasma and neutral atoms in both regimes. These currents are believed to be a contributing energy source for ion acceleration in the polar ionosphere and may be detected via measurements of magnetic gradients along the track of a polar orbiting spacecraft, usually the north-south gradients of the east-west field component. The detection of such gradients does not require observatory class measurements of the geomagnetic field. The Magnetic Field instrument (MGF) measures the local magnetic field onboard the Enhanced Polar Outflow Probe (e-POP) satellite by using two ring-core fluxgate sensors to characterize and remove the stray spacecraft field. The fluxgate sensors have their heritage in the MAGSAT design, are double wound for reduced mass and cross-field dependence, and are mounted on a modest 0.9 m carbon-fiber boom. The MGF samples the magnetic field 160 times per sec (~50 meters) to a resolution of 0.0625 nT and outputs data at 1952 bytes per second including temperature measurements. Its power consumption is 2.2 watts, and its noise level is 7 pT per root Hz at 1 Hz.

2.2 Introduction

The Enhanced Plasma Outflow Probe (e-POP) is a part of the multi-purpose CASSIOPE small satellite mission sponsored by the Canadian Space Agency (CSA). It is a companion to the Cascade advanced communications technology demonstration payload that serves as a high-speed data downlink for e-POP (as discussed below). The CASSIOPE spacecraft is in an elliptical, polar orbit, with an inclination 80.99°, a perigee of 325 km, and apogee of 1,500 km.

The scientific objective of e-POP is to study plasma outflows, neutral atmospheric escape, and associated effects of auroral currents and plasma microstructures on radio propagation at the highest possible resolution. Knowledge of the magnetic field is essential to this objective [*Yau and James*, 2015]. The primary objective of the Magnetic Field Instrument (MGF) on e-POP is the

[2] This chapter is based on [*Wallis et al.*, 2015] with contributions as described in the preface for this thesis.

characterization of electric currents flowing into and away from the high latitude (auroral) ionosphere.

Ionospheric currents result in energy being deposited in the ionosphere and drive plasma instabilities which give rise to wave particle interaction and ion acceleration [*André and Yau*, 1997] in the topside ionosphere. An integral part of this current system are low-frequency Alfvén waves that propagate to the ionosphere from the distant magnetosphere as the magnetic field is being distorted by the convecting plasma. These waves are an important source of both ion and electron acceleration in and above the topside ionosphere [*Watt and Rankin*, 2009, 2012]

The spatial distribution of the field-aligned currents therefore constitutes an essential measurement on e-POP. In the absence of a direct method for measuring currents, the ideal means of determining a field-aligned current distribution is to measure the curl of the magnetic field perturbations resulting from the current and to derive the current distribution based on Maxwell's equations. However, this cannot be done with one spacecraft. Instead we assume the FACs exist as current-sheet structures to reduce the problem to the determination of magnetic field gradients along the spacecraft track. Further, we employ a high cadence fluxgate vector magnetometer to allow us to resolve fine scale current structure. This determination can be successful in the presence of bias fields, such as those that might be present due to spacecraft systems, provided these bias fields are unchanged over the measurement interval.

The bias field from the spacecraft can be estimated and removed from the measured data using a method proposed by Ness et al. [1971]. The MGF payload includes two sensors on a single boom at different distances from the spacecraft. The Ness method uses the difference between simultaneous vector measurements taken at different radial distances to estimate the true environmental field and the potentially varying local field generated by the spacecraft. Notably, the Ness method is easiest to apply when the boom is aligned radially with the magnetic center of the spacecraft and is sufficiently long that the dipole term of the spacecraft stray field dominates. Neither of these conditions is well satisfied in the CASSIOPE/e-POP application making the estimation and removal of the spacecraft field more challenging.

Field-aligned currents enter and exit the auroral ionosphere with a typical density of 1 μAm^{-2} but on small spatial scales (~100 m) can exceed 100 μAm^{-2}; see for example Ijima and Potemra [1976] and Rother, Schlegel, and Lühr [2007]. The corresponding magnetic gradients are 1.25 and 125

nT per km or 0.12 and 12 nT per 100 m, respectively. The goal of MGF is the detection of 0.12 μAm^{-2} or stronger currents at scale sizes of 100 m or larger. This calls for an instrument with resolution of ~0.1 nT and a sample rate of 160 per second.

Elements of the Cascade payload and the CASSIOPE spacecraft bus are intrinsically magnetic, posing difficulties for the measurement of the ambient magnetic field. The MGF sensors are boom mounted to increase the separation of its measurements from the spacecraft's magnetic sources. Two sensors on the boom at two separations are used to estimate and correct for the spacecraft influences.

2.3 Instrument Design and Operation

A fluxgate magnetometer [*Primdahl*, 1979] makes vector measurements of the local magnetic field. It operates by gating the magnetic flux through a solenoid coil and detecting the induced electromagnetic field (EMF). Gating is achieved by periodically driving a specially constructed ring of ferromagnetic material into saturation using an alternating current of frequency f applied with a toroidal winding. The ring is placed in a solenoidal coil. The gated flux, in the presence of an external field, generates an EMF at frequency $2f$ in the solenoid due to the nonlinear permeability of the ring as it is driven into magnetic saturation [*Narod*, 2014]. This second harmonic signal is amplified in an AC amplifier, synchronously detected, integrated, and fed back to produce a field opposing and nulling the ambient field in the sensor. The system is carefully designed so that the only means of obtaining a signal at the $2f$ frequency is the non-linear behavior of the ring core.

The implementation of the over-all fluxgate design for e-POP MGF is illustrated in Figure 2-1. The time base circuitry generates a signal at frequency f = 16,457 Hz which is applied to the ring, driving it into saturation twice per cycle. The EMF induced by the changing flux in the sensor winding passes through a $2f$ band-pass filter and is synchronously detected. Parametric gain is achieved by capacitively loading the sensor [*Narod and Russell*, 1984]. The demodulated $2f$ signal is then integrated and digitized, and fed back through a trans-conductance amplifier to the sense/feedback winding. Each component incorporates a digital to analog converter (DAC) to bias the operating range of the instrument. This biasing technique is not commonly used but has been successfully employed by the CARISMA (previously CANOPUS) magnetometers [*Rostoker et al.*, 1995; *Mann et al.*, 2008] used on the Earth's surface.

The design of the MGF instrument was motivated by the measurement objectives in terms of sensitivity and sampling rate. A ranging magnetometer design was chosen as a suitable digitizer capable of the range of expected field values (±65,536 nT) was not available at the desired resolution (0.0625 nT) and sampling rate (160 samples per second) at the beginning of the e-POP project. A 12-bit analog to digital converter (ADC) digitizes the analog magnetometer signal in the range of –128 to +127 nT. A 17-bit DAC (16-bit integrated circuit with an external analog switch providing polarity control) with a 1 nT least significant bit applies an offset current to the combined sense/feedback winding to set the range under digitization. The output of the instrument is a combination of the DAC input bits and the ADC output bits. Each channel is restricted to steps of 64, 96, or 128 nT to reduce telemetry requirements and the frequency of offset adjustments. The bottom 5 bits of the DAC are therefore zero and are not telemetered.

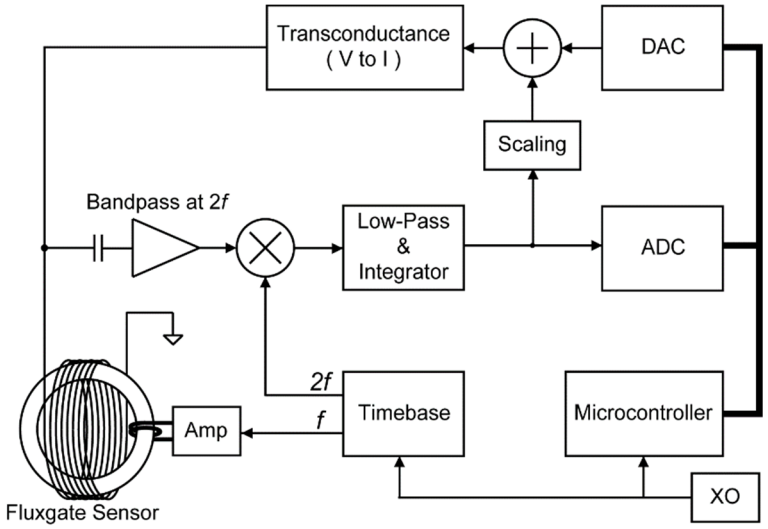

Figure 2-1: Simplified diagram of the MGF instrument showing the major functional blocks in each magnetometer.

The chosen DAC has integral and differential non-linearity of 0.2 least significant bit (LSB). Offset changes inevitably introduce a step function in the analog magnetometer circuit that will introduce a transient in the combined digital output. Offset changes are synchronous with the time base governing the sampling and are allowed only every fourth sample so they can be removed in post-processing.

The sensor design has its heritage in the NASA MAGSAT fluxgate design [*Acuña et al.*, 1978]. Infinetics manufactured the S1000 ring cores. They are close wound toroidally and cemented in their Macor feedback coil bobbins with room temperature vulcanizing (RTV) silicone. The combined feedback/sense coils are 360 turns of insulated copper wire wound under tension. The

thermal expansion of Macor is close to that of the rings and the tensioned winding effectively makes the thermal expansion of the copper wire equal to that of the Macor. Two orthogonal solenoidal coils are wound on each bobbin, providing two measurements in the plane of each ring. Figure 2-2 shows the two double-wound coil assemblies orthogonally mounted on a Macor block that is machined to mount on the magnetometer boom.

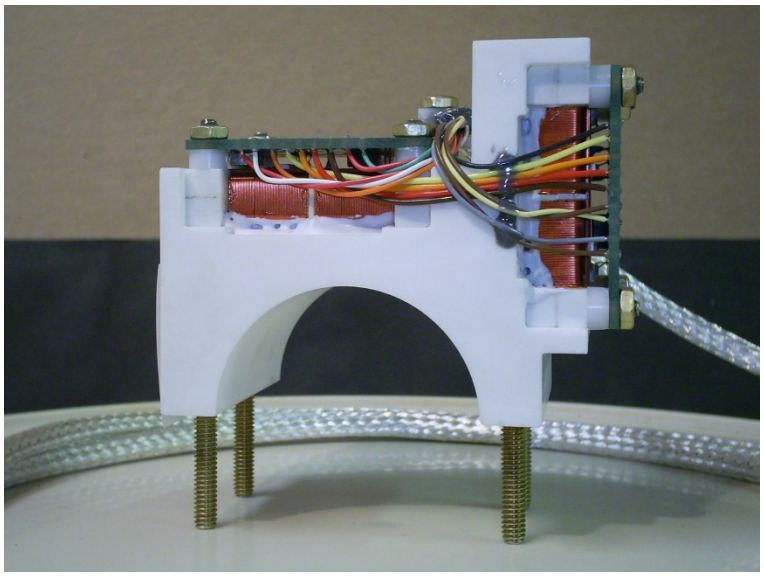

Figure 2-2: An MGF sensor constructed from two orthogonal ring-cores, each with a combined sense/feedback winding.

The X-Y, X-Z, and Y-Z angles between the sensitive axes have similar tolerances to a standard three ring sensor and were measured to be 89.9347°, 90.0239°, and 89.9326° respectively for the outer sensor and 90.1153°, 90.1047°, and 89.8066° respectively for the inner sensor. Our adoption of a two-ring design resulted in a significant reduction in mass (as only two rather than three rings and sensor bobbins are needed) and in the reduction of the cross-field sensitivity to near zero. Cross field sensitivity is an undesirable response to the orthogonal field component in the plane of the ring [*Acuña et al.*, 1978]. By simultaneously zeroing both components, cross-field sensitivity is minimized.

In this design, one ring gates the flux in the X and Z directions while the second ring gates the Y and Z directions; X and Z being the nominal spacecraft ram face (out of the page in Figure 2-6 below) and nominal nadir direction (down in Figure 2-6 below), respectively. Figure 2-3 shows how the Z feedback coils are wired in series, so that the result for the Z component is the average of the Z fields at the two rings.

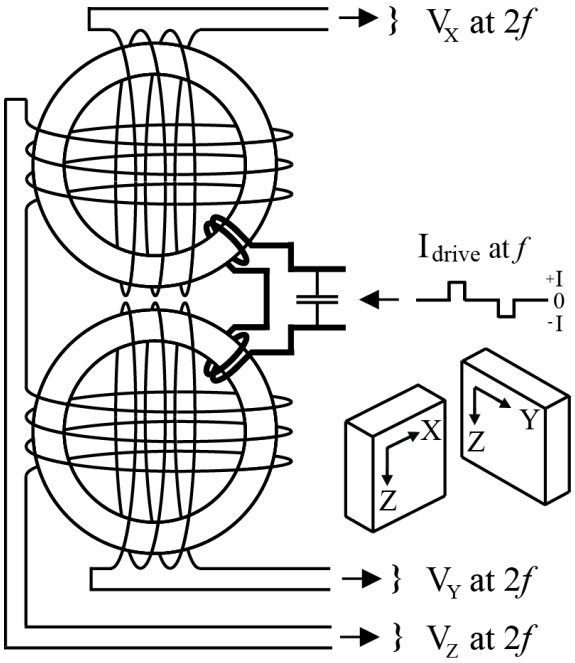

Figure 2-3: Wiring diagram for the fluxgate sensor. Channels X and Y are each derived from orthogonal sense/feedback windings. Channel Z is derived from two sense/feedback windings connected in series. The two rings and their respective windings are mounted orthogonally as shown in the inset.

The MGF incorporates two independent and almost identical electronics boards. Each board contains its own DC-to-DC switched power converter, to allow each one to operate independently should the other fail. Both boards share the data, command and power interfaces. Figure 2-4 shows the MGF flight electronics box and connectors. The top and bottom ports are for the two fluxgate sensors. The two middle ports are for power and communication with the spacecraft bus, respectively.

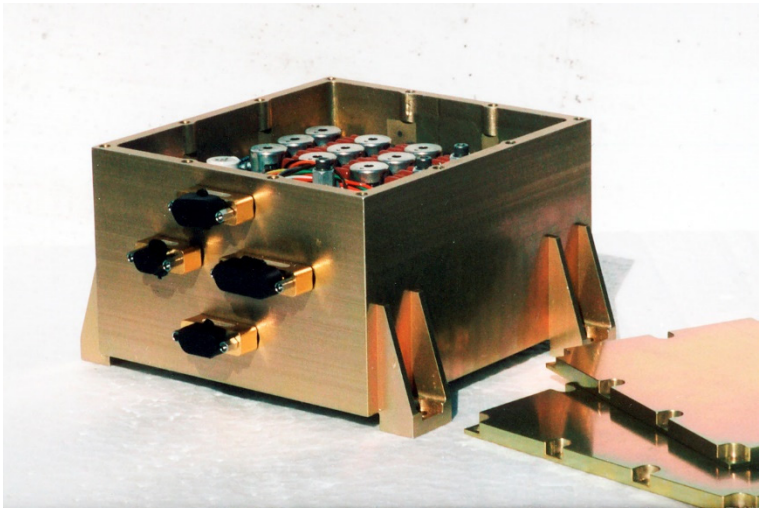

Figure 2-4: MGF flight electronics box, with the top and bottom covers removed. The top and bottom ports are for the two fluxgate sensors. The two middle ports are for power and communication with the spacecraft bus.

Each board has its own crystal oscillator, excitation drive circuitry, controller, and magnetometer circuitry with DACs and ADCs for each measured component. The crystal oscillator on each board is cross-strapped with the other board to serve as backup for the other oscillator in the case of failure. At power up, a failure tolerant voting circuit selects one oscillator to drive both boards synchronizing the two magnetometers. The two cards share one power feed and each provides data on a RS-422 synchronous interface to the e-POP Data Handling Unit (DHU). Time multiplexing of the data from each magnetometer allows sharing of the interface to the DHU. Data transmission is synchronized to the spacecraft-generated 1 Hz clock. Additionally, the cards are wired so that if the 1 Hz spacecraft clock is unavailable for synchronization at power-up, the card currently in "Master" mode continues to operate while the other card in "Slave" mode goes dormant and will not transmit.

The magnetometer data comprise 160 12-bit ADC samples per second for each of three magnetic components. The DAC for each component is updated and telemetered as a 12-bit value 40 times per second (every fourth ADC value). The data require 900 bytes per second per magnetometer. Two data blocks are transmitted to the data-handling unit per second, one for each of the magnetometers. Each data block is 976 bytes long and contains 76 bytes of housekeeping and status data, memory checksums and software flags.

The employed controller chip is the Atmel ATMEGA32L 8-bit microprocessor, clocked at 3.6864 MHz. Its on-chip digitizers monitor the temperatures of both sensors and both electronics boards, and voltages derived from the internal voltage rails. Figure 2-5 shows the electronics card for one of the magnetometers staked and mounted for flight.

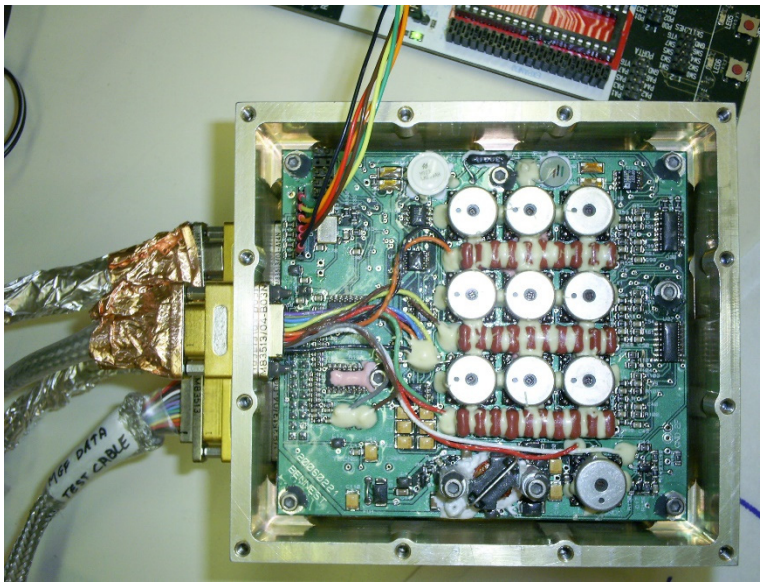

Figure 2-5: Electronics card for one of the MGF magnetometers, with the electronic components staked for flight and an external programmer connected for testing and reloading of the onboard microcontroller.

The MGF is intended to operate continuously whenever possible, to maximize the data acquisition both inside and outside the auroral zone and the polar cap. The MGF data samples are time-stamped against the spacecraft 1 Hz pulse, which is derived from the onboard GPS receivers. A custom firmware bootloader allows the MGF firmware to be reloaded during flight via spacecraft command. Essentially any subset or the full set of the firmware may be reloaded.

As the temperature of the sensors varies, the physical dimensions of the feedback coil change. Nulling a given field component then requires a different current from the trans-conductance amplifier. Additionally, the resistance of the copper wire making up the feedback coil changes, producing another source of temperature variation. The trans-conductance amplifier senses the voltage of the feedback current circuit which is fed back to the input via a temperature compensation network [*Acuña et al.*, 1978]. The load resistance (and its temperature dependence) is dominated by a 100-ohm platinum resistor in series with the feedback coil. This platinum resistor is cemented to the feedback winding with Nusil CV2942 thermally conductive elastomer. Changes in sensor temperature cause a linear change in gain scaling that is measured to be -0.6, -1.3, and +1.2 nT/$^{\circ}$C in the X, Y, and Z channels respectively. Sensor temperature has no measurable effect on the instrumental zeroes.

A carbon fiber boom is used to position the sensors at a modest distance from the spacecraft. At launch, the boom was in a stowed configuration, folded at the base of the CASSIOPE spacecraft

and held in place by a hinge mechanism at one end and a deployment actuator and a pin puller arrangement at the other. The deployment actuator provides a positive deployment force when a small pin is removed from a plug in the end of the boom. The pin puller is of the melting wax type employing a redundant heater element. The hinge assembly utilizes a viscous damper to slow the deployment and a locking wedge to secure the deployed boom. A potentiometer was used to measure the hinge angle. The MGF boom was released early in the commissioning phase of the mission and deployed to an angle of 89.2° ±1°. Figure 2-6 depicts the MGF in the deployed configuration, showing the inboard and outboard fluxgate sensors.

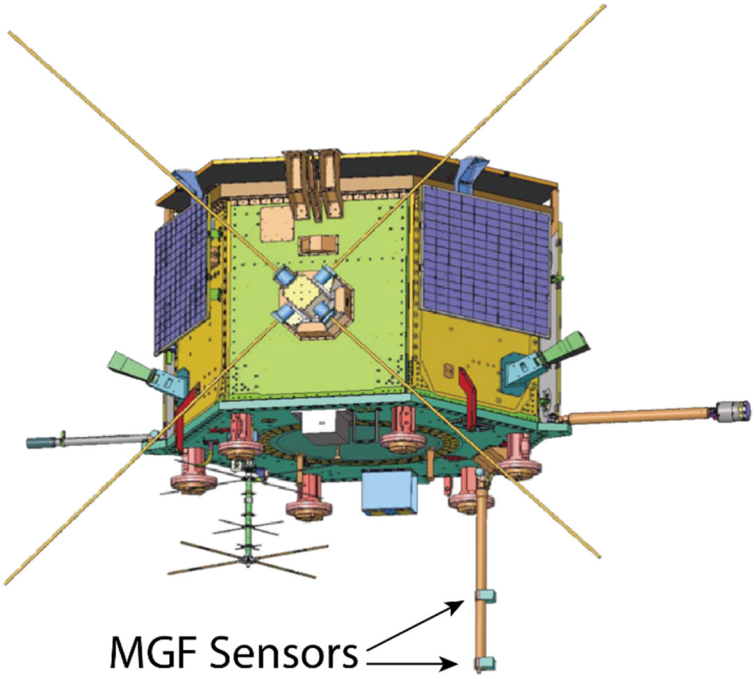

Figure 2-6: MGF in deployed configuration showing the inboard and outboard fluxgate sensors.

Carbon fiber was chosen to eliminate fields due to eddy currents that would be induced in a metallic boom. Such fields were estimated to be ~10 nT at times of large changes of the ambient field. The boom was machined to achieve a smooth surface at the mounting locations of the sensor assembly. The bases of the sensors were machined to have a semi-circular saddle of the same diameter as the machined boom. A thin layer of thermally conductive RTV silicone was applied to the boom before final assembly. A mounting bracket made of aluminum was cemented to the backside of the boom to provide a reference surface for remounts during tests and calibrations. The entire boom was covered with a multilayer conductive blanket for thermal control.

Since the thermal conductivity of Macor is moderately high, the thermal coupling between the Macor bases and the boom provides a large thermal mass and reduces the temporal changes of the temperature of the sensors (which has generally been in the range of -15 to -30 °C on orbit). A small, 2-watt survival heater situated midway between the two sensors on the boom is programmed to activate at -40 ºC and deactivate at -38 ºC. The controlling thermistor is mounted at the outboard sensor bracket. The current required by the survival heater should create a detectable stray magnetic field at both sensors. However, there was no opportunity to characterize this before launch and, since commissioning, there has never been an MGF observing session where the sensor was sufficiently cold to activate the heater.

The CASSIOPE/e-POP satellite can control its attitude using either reaction wheels or magnetic torque rods. Both techniques impact the magnetic field measurement. However, the torque rods render the magnetic data unusable so the spacecraft is normally restricted to reaction wheels during MGF observing sessions. The instrument is saturated (but is not damaged) by exposure to the fields from the torque rods of approximately 1,000 to 2,000 nT at the boom end. The instruments servo rapidly back into the range of the environmental field after the torque rods finish firing. The four reaction wheels are normally idle with a frequency near 15 Hz but vary between 10 and 20 Hz during maneuvers. The combined magnetic signature of the four wheels is a varying envelope sinusoid with a peak-to-peak amplitude of 10-20 nT. Low-pass filtering the measured data removes the majority of the reaction wheel tones. More sophisticated filtering is in development to suppress the reaction wheel interference in the full cadence data.

The stray spacecraft field of the CASSIOPE/e-POP satellite can be estimated and removed using the dual-magnetometer technique described by Ness et al. [1971]. It was not possible to fully characterize the stray magnetic fields of the spacecraft in its many different operational configurations on-orbit before launch. The stray field is therefore estimated from in-flight data by treating it as a dipole field at the center of the spacecraft. The estimation is further simplified by assuming that the two magnetometers are co-aligned and radial to the spacecraft dipole. The measurement from each sensor is corrected using an orthogonality matrix and then rotated into the frame of the boom before the dual magnetometer technique is applied. These assumptions allow us to create a dynamic estimate of the spacecraft field that can be subtracted from the measured field to obtain the corrected estimate of the ambient magnetic field. It should be noted that it is not

possible to separate instrumental zero drift and spacecraft fields solely from on-orbit measurements. However, the zeroes can be independently estimated using spacecraft roll maneuvers. The dual magnetometer method was illustrated by Acuña [2002] and was employed recently in the Double Star mission [*Carr et al.*, 2005].

The relative proximity of the two sensors introduces crosstalk between them. The separation is governed by the length of the boom and the magnitude of the spacecraft field components at the sensors. Each sensors acts to null the field in its solenoidal coils, which generates a stray surrounding magnetic field. In testing, the perturbation of a 50,000 nT field on the X, Y, and Z components by the other sensor is 2, 2 and 13 nT, respectively. The effect is linear with ambient field. The Z component is larger because it comprises two coils per magnetometer (increasing the size of the source) and the Z axis is parallel to the boom while X and Y axes are orthogonal. This interaction is scaled and removed from the flight data in post-processing.

Table 2-1 lists the spacecraft resources required by MGF and Table 2-2 summarizes the key science measurement parameters described in this section.

Table 2-1: Spacecraft resources required by the MGF.

MGF component	**Mass (kg)**	**Power (watts)**	**Dimensions (mm)**
Electronics Box	1.22	2.2	130 × 110 × 70
Sensors (2)	0.58	0.2	70 × 50 × 60
Sensor Harness	0.35	-	-
Boom	1.17	-	44 × 900
Boom Hardware	1.11	-	-

Table 2-2: Key science measurement parameters achieved by MGF.

Data Rate	**1.9 kbps**
Sampling Cadence	160 sps
Magnetic Range	±65,536 nT
Resolution	0.0625 nT

Before spacecraft integration, the two e-POP MGF flight magnetometers were calibrated individually at the Geomagnetic Laboratory of National Resources Canada near Ottawa. Sensitivity and directions of the sensitive axes with respect to the boom were determined, as well as the temperature dependence of both the electronics and the sensors. The magnetometers were

found to exhibit no meaningful sensitivity to the supply voltage. The cross talk between the boom-mounted sensors was also characterized.

Figure 2-7 presents power spectral density measurements acquired from the engineering model electronics card and the Infinetics core-based sensor. These data are comparable to the performance achieved by both flight instruments. These spectra are taken with the sensor operating in a 6-layer magnetic shield at effectively zero field at all frequencies. Two narrow features are present at 30 and 60 Hz. These are likely residuals of the AC power lines in the laboratory. The spectra show the expected 1/*f* frequency dependence of the noise floor, which is below 10 pT per $Hz^{1/2}$ at 1 Hz and achieves our goal of resolving currents of 0.1 μAm^{-2} in 100-m wide structures.

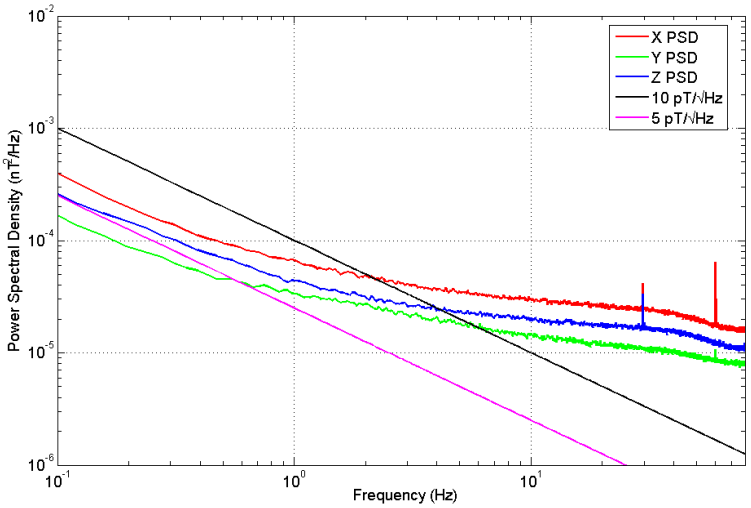

Figure 2-7: Engineering model magnetometer frequency spectra.

2.4 MGF Data Products

Several data products are created from the MGF measurements. Level 0 and 1 data are not expected to the useful to the general science user and are therefore not routinely distributed. In addition, MGF generates Level 2 and 3 data on a routine basis. Level 2 data reconstructs the fully calibrated magnetic measurement from each sensor rotated into the reference frame of the spacecraft, and is useful for the analysis of the particle distribution measurements taken by other science instruments. Level 3 data use the Ness et al. [1971] dual magnetometer technique described above to estimate and remove the spacecraft magnetic field. Level 3 data contains single three-component estimates of the local field. Resampled perfectly second-aligned 10-samples per second (sps) and 1-sps time series are also produced. These time series are available in the spacecraft coordinate system and rotated into the Geocentric Equatorial Inertial (GEI) coordinate system. Quick look and summary

plots are created from Level 2 data for each MGF orbit pass. The various MGF data products including the data plots are available online through the Canadian Space Science Data portal (http://www.cssdp.ca).

2.5 Example of MGF Observation Data

Figure 2-8a shows ground tracks for two consecutive conjunctions over the Fort Smith all sky imager [*Mende et al.*, 2009] crossing the North American sector of the night side auroral oval from between 56 and 65 degrees latitude on February 27 and 28, 2014. Both orbits pass near the center of the field of view of the Fort Smith all sky imager (ASI) at 09:18:36 UT. During these passes the e-POP Fast Auroral Imager (FAI) payload was not operating hence, we use THEMIS ground based ASI data. The spacecraft was in Nadir pointing mode so, in the spacecraft coordinate system, +Z is in the Nadir (down) direction, +X is in the direction of spacecraft motion (approximately northward), and +Y completes the right-handed coordinate system (approximately eastward). Field-aligned currents can be detected as perturbations in the local magnetic field compared to the nominal background. In this analysis, the cross-track spacecraft Y component was selected to minimize the effect of orbit and attitude uncertainty as discussed by Anderson et al. [2000]. February 27 was a geomagnetically quiet day with no significant auroral activity in the region of interests (Figure 2-8b). The pass on February 28 intersected several auroral forms between 56 and 65 degrees latitude (Figure 2-8c) during a substorm expansion phase, which initiated at 07:51 UT.

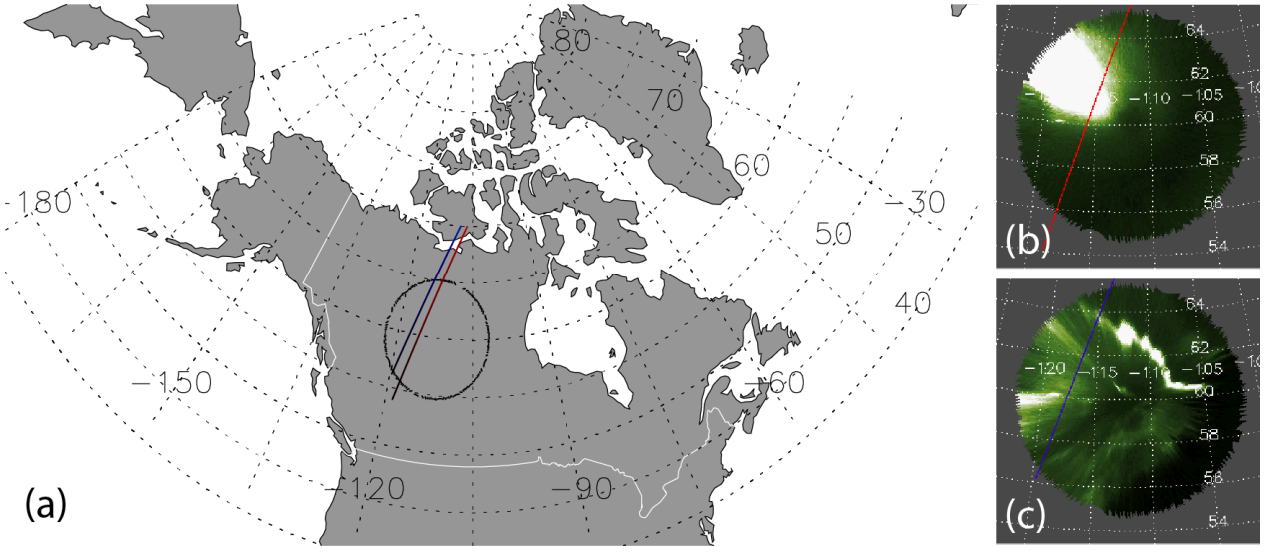

Figure 2-8: Case study on February 28, 2014. (a) Field of view of the Fort Smith all sky imager and spacecraft track for February 27 (black to red shows poleward spacecraft motion) and 28 (black to blue shows poleward spacecraft motion). (b) Fort Smith all sky camera February 27, 2014 at 09:18:36 UT with superposed spacecraft track in red. (c) Forth Smith all sky camera February 28, 2014 at 09:18:36 UT with superposed spacecraft track in blue.

Figure 2-9a shows the magnetic field measurement in the spacecraft Y component (cross-track, approximately eastward) versus latitude on February 27 and 28 as respectively red and blue. The magnetic data have been low-pass filtered at 4.5 Hz to suppress the stray magnetic field from the four reaction wheels used to steer the spacecraft. Figure 2-9b compares the FAC densities observed during each pass. The FAC densities are approximated using the spacecraft Y component magnetic field and X component velocity of the spacecraft as described in Potemra [1985]. This approximation ignores perturbations in the spacecraft X magnetic field component and assumes that that the spacecraft motion is predominantly along the spacecraft X direction. Positive (negative) denotes upward (downward) FACs or downward (upward) going electrons. It is clear from Figure 2-9b that the FAC amplitudes are both stronger and more dynamic in the presence of the aurora.

The relation between auroral features and FAC intensities is better illustrated by comparing the along-track auroral intensity from the Fort Smith ASI with the estimated FACs. This is shown in Figure 2-9c and Figure 2-9d. Figure 2-9c plots the FAC from February 28 (same as Figure 2-9b) with the along-track auroral intensity. The FAC strength is shown in blue and the auroral intensity in green. Figure 2-9d plots the average FAC intensity over a spatial scale of 0.25 degrees (~60 km), the approximate scale size of auroral features observed in the Fort Smith ASI by smoothing the data at 4 seconds with the along track auroral intensity (in the same format as Figure 2-9c). During the auroral pass it is clear that FACs are both large and very dynamic with the largest FAC strengths observed at the peak in auroral intensity at ~60 degrees latitude. Averaging over 0.25 degrees (~60 km), Figure 2-9d, shows a net upward FAC in the region between 59.5-61.5 degrees. This matches the peak in auroral intensity where we would expect to find downward going electrons. Similarly, between ~58.5-59.5 degrees a secondary peak in auroral intensity is associated with a net upward FAC. Conversely, the peak in auroral intensity between 61.5-62 degrees is associated with a net downward FAC. This is likely an artifact of using a single magnetic field component in spacecraft coordinates and a simple approximation to calculate FACs.

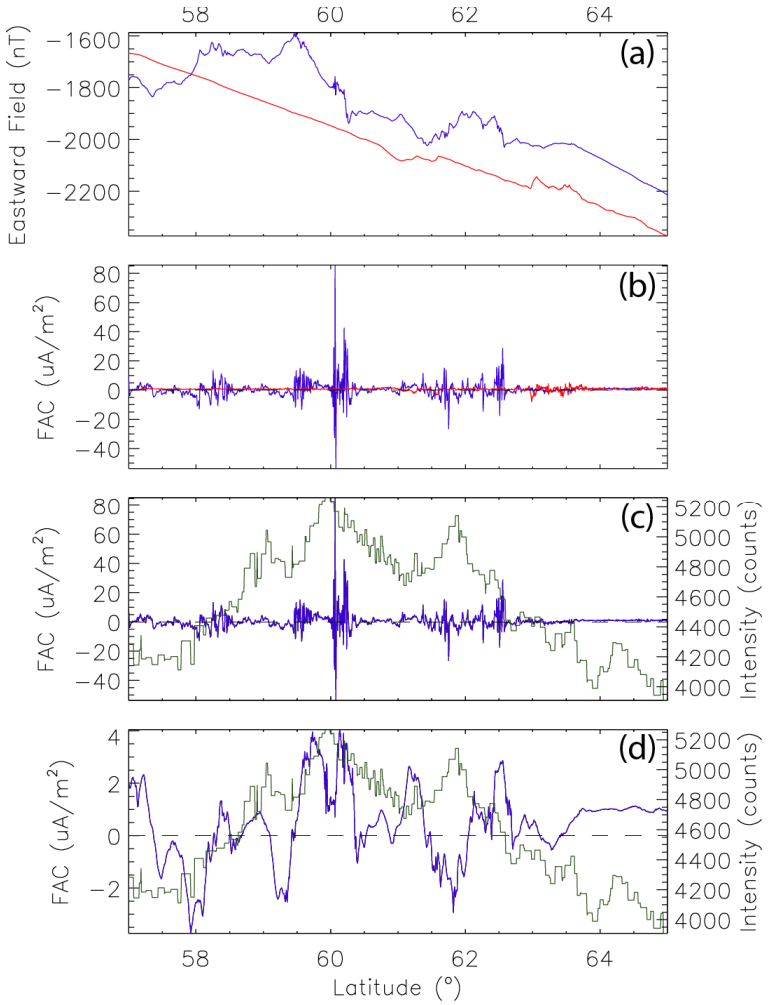

Figure 2-9: Comparison of auroral intensity and magnetic perturbations. (a) Spacecraft Y magnetic field (eastward) versus latitude from February 27 quiet day (red) and February 28 as the spacecraft passes through an active auroral region (blue). (b) FAC amplitudes for February 27 (red) and February 28 (blue). (c) FAC amplitude on February 28 (blue) and along-track auroral intensity from the Fort Smith all sky imager (green). (d) FAC amplitudes on February 28 (blue) averaged at 4 seconds to show the net FAC density on the spatial scale of the auroral forms observed at the Fort Smith all sky imager. This smoothing corresponds to approximately 60 km scales, or 0.5 degrees in latitude. The along-track intensity from the Fort Smith all sky imager is shown in green. In panels (b)-(d) positive denotes upward FACs or downward going electrons.

In general, the magnetic signature of field-aligned currents is more accurately determined from the deviation from the theoretical International Geomagnetic Reference Field (IGRF) [*Anderson et al.*, 2000; *Waters et al.*, 2001]. This requires accurate background field removal, which at this time is limited by the processing of the spacecraft attitude solution, which introduces artifacts into the subtraction of the background field from the measured spacecraft field. Once these issues are resolved, we intend to routinely generate and distribute FACs estimated from the east-west and north-south magnetic field perturbations to provide a more robust FAC estimate. We also intend to integrate the e-POP magnetic field data into the AMPERE and Iridium determinations of FACs on a case-by-case basis to provide global estimates of FACs from multiple spacecraft.

2.6 Conclusions

Field-aligned currents may be detected via measurements of magnetic gradients along the track of a polar orbiting spacecraft (usually the north-south gradients of the east-west field component). The Magnetic Field Instrument (MGF) on the Enhanced Plasma Outflow Probe (e-POP) measures the local magnetic field onboard by using two ring-core fluxgate sensors to characterize and remove the stray spacecraft field. The fluxgate sensors draw their heritage from the MAGSAT design, and the instrument relies on a ranging design that was previously adopted successfully in the CARISMA ground-based magnetometers. Sensor mass has been reduced by using each ring core to sense two components of the field. This has the added benefit of minimizing cross-field dependence. The MGF samples the magnetic field at 160 samples per sec (~50 meters) to a resolution of 0.0625 nT and has a noise level of 7 pT per root Hz at 1 Hz. Data in the first few months of the mission has demonstrated the potential of the instrument to achieve its scientific goal of providing high fidelity measurements of field-aligned current structures in the high-latitude auroral ionosphere.

2.7 Acknowledgements

We acknowledge the support from the Canadian Space Agency for the development and operation of the CASSIOPE/e-POP mission. The authors are grateful for the support and guidance of R. Hum. We thank J. Schmidt of Minerva Technology Inc. for his contributions to the flight firmware, W. Lunscher and his team at COM DEV for their technical assistance, and the technical team at Magellan Aerospace Corporation for the boom development. K. R. Murphy is supported by an NSERC Postdoctoral fellowship. D. M. Miles is supported by grants from the Canadian Space Agency and a Canadian NSERC PGSD2 graduate scholarship. I. R. Mann is supported by an NSERC Discovery Grant. A.W. Yau is supported by grants from the Canadian Space Agency and the NSERC Industrial Research Chair and Discovery Grant programs.

Chapter 3: A Miniaturized CubeSat Fluxgate Magnetometer[3]

3.1 Abstract

Difficulty in making low noise magnetic measurements is a significant challenge to the use of CubeSat nanosatellite platforms for scientific constellation class missions to study the magnetosphere. Sufficient resolution is required to resolve three-dimensional spatio-temporal structures of the magnetic field variations accompanying both waves and current systems of the non-uniform plasmas controlling dynamic magnetosphere-ionosphere coupling. This chapter describes the design, validation, and test of a flight-ready, miniature, low-mass, low-power, and low-magnetic noise boom-mounted fluxgate magnetometer for CubeSat applications. The miniature instrument achieves a magnetic noise floor of 150-200 pT/√Hz at 1 Hz, consumes 400 mW of power, has a mass of 121 g (sensor and boom), stows on the hull, and deploys on a 60 cm boom from a three unit (3U) CubeSat reducing the noise from the onboard reaction wheel to less than 1.5 nT at the sensor. The instrument's capabilities will be demonstrated and validated in space in 2017 following the launch of the University of Alberta Ex-Alta 1 CubeSat, part of the QB50 constellation mission. We illustrate the potential scientific returns and utility of using a CubeSats carrying such fluxgate magnetometers to constitute a magnetospheric constellation using example data from the Low-Earth Orbit (LEO) European Space Agency (ESA) Swarm mission. Swarm data reveal significant changes in the spatio-temporal characteristics of the magnetic fields in the coupled magnetosphere-ionosphere system, even when the spacecraft are separated by only approximately 10 seconds along track and approximately 1.4 degrees in longitude.

3.2 Introduction

The advent of nanosatellite technology, particularly CubeSats, over the last few decades is changing the scale of spacecraft missions opening up the possibility of using miniature CubeSat type platforms as a solution for delivering low-cost constellation class missions. Recently, a number of missions such as the ESA-NASA Cluster mission [*Escoubet et al.*, 2001], NASA Time History of Events and Macroscale Interactions during Substorms (THEMIS) [*Angelopoulos*, 2009], and the NASA Magnetospheric Multi-Scale (MMS) mission [*Burch et al.*, 2016], have operated four or five spacecraft. These missions have made excellent progress on understanding

[3] This chapter is based on [*Miles et al.*, 2016] with contributions as described in the preface for this thesis.

some of the fluid-, ion-, and now even electron-scale physics of the coupled solar wind-magnetosphere-ionosphere system. However, as recognized by the recent NASA Heliophysics Science and Technology Roadmap for 2014-2033 [*Heliophysics Roadmap Team*, 2014], one of the next critical opportunities to drive scientific discovery will come from a magnetospheric constellation (MagCon) type mission of 30 or more spacecraft.

The number of CubeSats being launched is increasing exponentially [*Hand*, 2015b], creating new opportunities for scientific research exploiting miniaturization, constellations, expendability, and redundancy to offset the cost of entry to space [*Hand*, 2015a]. CubeSat platforms could serve as the basis for future formation flying [*Bandyopadhyay et al.*, 2015] constellation class missions measuring the magnetic fields across large regions of the magnetosphere in three dimensions as well as time. This would resolve the details of the spatio-temporal evolution of electrical currents and waves, which couple and control some important dynamics of the system. However, there are challenges associated with the development of specialized miniature instruments with suitable mass, power, and volume to be accommodated on a CubeSat without sacrificing the scientific utility.

Here, we describe a miniature, boom-mounted fluxgate magnetometer suitable for future CubeSat missions, which has been developed to demonstrate the potential of magnetic measurements on a CubeSat. The instrument is intended principally as a variometer to study perturbations on the background field, rather than for absolute field measurements. It is a complete, flight ready scientific fluxgate magnetometer (Figure 3-1) of sufficient fidelity to conduct detailed field-aligned current studies, and will be test flown in late 2016 on the Experimental Albertan #1 CubeSat (Ex-Alta 1). Ex-Alta 1 is the University of Alberta's first CubeSat mission and the first spacecraft to be built in Alberta. It represents the University's contribution to the international QB50 mission [*Muylaert et al.*, 2009] for in-orbit demonstration of CubeSat systems and technology, for the training of students, and for multi-point research into the coupled magnetosphere-ionosphere-thermosphere system.

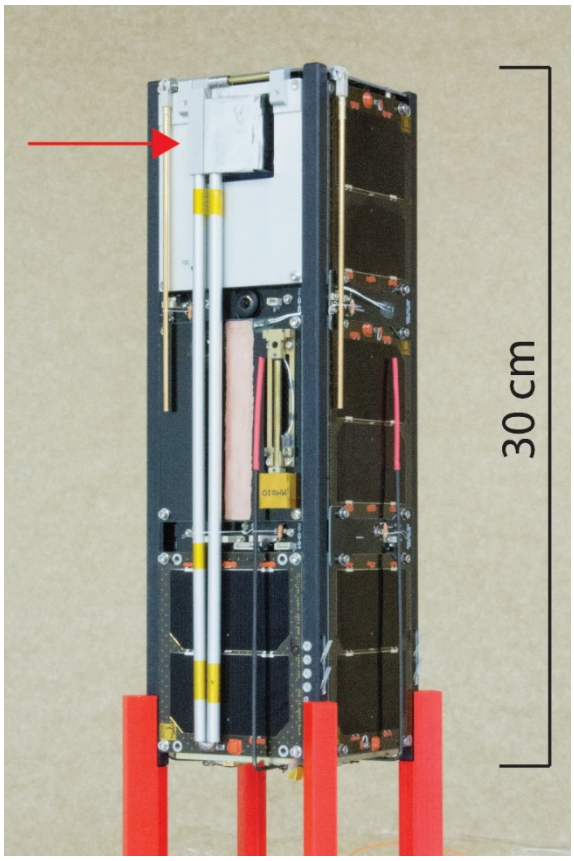

Figure 3-1: Miniature boom-mounted fluxgate magnetometer sensor stowed on the Ex-Alta 1 CubeSat. Arrow shows the fluxgate sensor atop its folding 60 cm boom in its stowed configuration.

Ex-Alta 1 will be launched from the International Space Station via a NanoRacks deployer to an orbit with a nominal altitude of 400 km, an inclination of 51.6°, and an orbital period of 92.6 minutes. Ex-Alta 1 carries three scientific instruments: the miniature fluxgate magnetometer described here, a needle-Langmuir probe [*Bekkeng et al.*, 2010], and a dosimeter [*Mazur et al.*, 2011]. Once in orbit, down-sampled magnetic measurements from the magnetometer will be validated by comparison to magnetic field models such as IGRF or CHAOS [*Finlay et al.*, 2015] during magnetically quiet geophysical conditions and portions of the orbit. The utility of the full cadence 100 sps burst mode data will be evaluated using conjugate studies to compare against magnetic field measurements from the ESA Swarm spacecraft [*Friis-Christensen et al.*, 2008], and the magnetic field experiment [*Wallis et al.*, 2015] on the CSA Cassiope/e-POP spacecraft [*Yau and James*, 2015]. Higher frequency ULF-band waves observed in the 100 sps data will be compared with ground based magnetometer data, such as those from the Canadian CARISMA array [*Mann et al.*, 2008], to establish that the CubeSat magnetometer is measuring geophysical phenomena such as Pi1B waves observed during substorm onset [*Lessard et al.*, 2011] rather than

spacecraft noise. Field-aligned current measurements will also be validated by comparison to auroral signatures from the THEMIS GBO all-sky imagers in North America [*Mende et al.*, 2009], and to high-cadence (1 Hz) Infra-Red Auroral imaging from the e-POP Fast Auroral Imager [*Cogger et al.*, 2014].

In the sections below, we describe in detail the design of our CubeSat fluxgate magnetometer instrument, and outline its performance. In advance of our conclusions, we also use data from the Swarm mission to outline the scientific utility of an example low-Earth orbit (LEO) constellation class mission, and demonstrate its potential value for studying and resolving the spatio-temporal dynamics of the coupled and dynamic magnetosphere-ionosphere system. For example, four identical nanosatellites could each use a boom-deployed scientific fluxgate magnetometer, creating a constellation with variable along-track and cross-track separation (Figure 3-2). Implementing the constellation using three unit (3U) spacecraft would require modest launch mass, and would be compatible with standard CubeSat deployers. Six unit (6U) spacecraft would allow for additional instruments and spacecraft propulsion, but would require additional launch mass. After validation in small constellations, such CubeSats could also be used in much larger constellations as well.

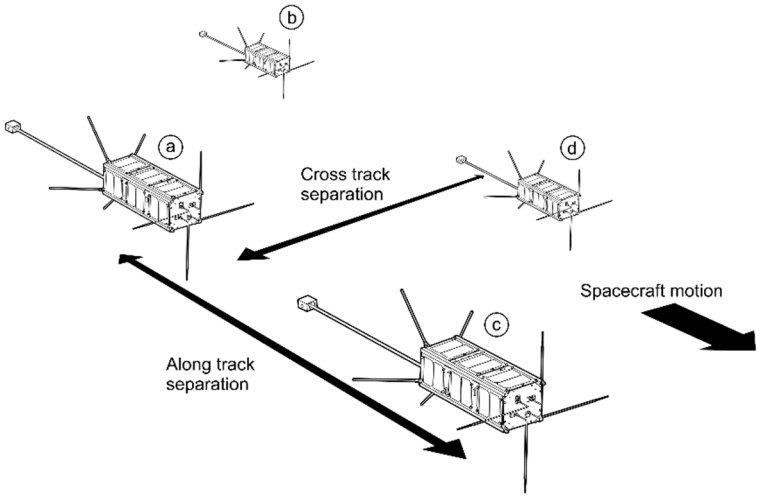

Figure 3-2: CubeSat constellation concept with variable cross-track and along-track separation to provide over specified magnetic curl measurement to estimate field-aligned current density.

Such a four CubeSat constellation could, for example, be placed into a LEO polar orbit crossing the auroral oval from a single launch vehicle, even one with a relatively low mass orbital throw capacity. Varying the cross-track separation of pairs a-b and c-d would allow the spatial scales of field-aligned currents to be studied by tracking the correlation in measured magnetic field perturbation as a function of cross track separation. Varying the along-track separation of pairs a-

c and b-d would allow the temporal dynamics to be investigated. This would partially restore the string-of-pearls configuration from the early Swarm mission, which has demonstrated utility for resolving temporal evolution of plasma structures [*Goodwin et al.*, 2015; *Spicher et al.*, 2015], and statistical characterization of the Earth's field-aligned current systems [*Gjerloev et al.*, 2011].

Magnetic perturbations received simultaneously on more than one spacecraft could be examined to separate wave processes, such as those due to the exchange of Alfvén waves between the magnetosphere and ionosphere, from current systems which appear static on given spatial scales as a function of their time scale [*Gjerloev et al.*, 2011]. Future missions with electric field measurements may be able to distinguish between Alfvén waves and quasi-static structures by examining the ratio of electric and magnetic perturbations [*Knudsen et al.*, 1990; *Dombeck et al.*, 2005] when the spacecraft is at an altitude sufficiently high above the ionosphere that the ratio is not dominated by the height-integrated Pedersen conductivity. The Ex-Alta 1 mission will focus on demonstrating that the relevant magnetic perturbations can be reliably measured on a CubeSat platform.

The use of four spacecraft provides multiple quasi-independent estimates of magnetic perturbations, over specifying the local magnetic curl, and allowing for an error estimate on the derived field-aligned current density. Additional spacecraft with vertical separation would also be desirable. However, the required increased orbital radius of such spacecraft would rapidly move them away from the lower constellation. Expansion into a much larger constellation could provide coverage on a more global scale too (cf. the Active Magnetosphere and Planetary Electrodynamics Response Experiment (AMPERE) project [*Anderson et al.*, 2000; *Waters et al.*, 2001]) allowing studies of magnetosphere scale phenomena [*Murphy et al.*, 2013].

The scientific utility of such a CubeSat constellation is significantly advanced by the availability of a complete, flight-ready magnetometer and boom payload delivering magnetic measurements with the appropriate sensitivity and resolution. In this chapter, we describe the design of a miniature three-axis fluxgate magnetometer, which can be flown on CubeSats within such a constellation. Once attitude determination and control systems have developed even further the magnetometer instrument design presented here could also be used in follow-on higher apogee missions, such as those envisaged for a MagCon type mission in the global magnetosphere.

3.3 Payload Definition

3.3.1 Measurement Requirements

Historical field-aligned current studies have been able to derive scientifically valuable results from magnetometers with even modest resolution. For example, Iijima and Potemra [1976] used measurements from the Triad spacecraft with a resolution of 12 nT and a cadence of 2.25 samples per second (sps). Studies employing the AMPERE experiment from the Iridium network have used the navigation magnetometers which are digitized to a resolution of 48 nT, and, despite a native sampling rate of 11 sps, are typically down sampled to a 200 s period before being telemetered [*Anderson et al.*, 2000]. For more modern missions a resolution of around 1 nT is typically accepted as the required minimum resolution – with 0.1 nT or better being preferred. Historically this required a large instrument not easily accommodated on a CubeSat. For example, Freja [*Freja Magnetic Field Experiment Team*, 1994] provided 2 nT resolution at 128 sps as a normal telemetry mode (with high cadence burst modes and AC data channels). The Space Technology 5 (ST-5) [*Purucker et al.*, 2007] fluxgate magnetometers continued the overall trend of low mass, power, and volume fluxgate to fit on the three micro satellites used in the mission. The ST-5 fluxgates provided 16 sps vector magnetic measurement at 1.25 and 0.30 nT resolution in high (± 64,000 nT) and low (± 16,000 nT) range respectively using a sensor of only 5 x 5 x 3 cm [*Slavin et al.*, 2008]. The most sensitive and accurate absolute magnetic field measurements to date are from the Swarm mission [*Friis-Christensen et al.*, 2008]. The Swarm Vector Field Magnetometer provides 62.5 pT resolution with a native cadence of 50 sps [*Merayo et al.*, 2008]. For comparison, Cassiope/e-POP provided 62.5 pT resolution at 160 sps [*Wallis et al.*, 2015], but the data above 20 Hz were degraded by interference from the spacecraft's reaction wheels.

Based on these successful previous missions, the CubeSat fluxgate magnetometer presented here was designed with the goal of achieving a minimum magnetic resolution of 0.1 nT, a maximum magnetic noise of 50 pT/√Hz, a nominal cadence of 1 sps, and the capability to burst sample to above 10 sps. This resolution must be achievable in the full strength of the Earth's magnetic field at LEO, giving a target magnetic range of at least ±60 μT. For Ex-Alta 1, no firm goals were set for axes orthogonality, thermal stability, or stability over time because the instrument was planned to be used principally as a variometer. We do not plan to routinely rotate the data into a geophysical frame, partly because of the expected attitude knowledge that will be available from the ADCS system, and often only the cross-track component will be considered. These parameters will be

much more important for future constellation missions where the data from multiple platforms will be inter-compared to estimate the local magnetic curl. Specific science goals and constellation geometry will determine future mission requirements; however, axis orthogonality within 0.5° (and measured to 0.005°), thermal gain stability of 50 ppm/°C or better, and drift of less than 500 pT/day are likely reasonable targets. Similarly, future three-axis stabilized missions may impose the strictest requirements on attitude knowledge and control.

Ex-Alta 1 is a three-axis stabilized spacecraft, which requires the actuation of three magnetorquers and one reaction wheel to maintain its orientation and these attitude control subsystems generate significant local magnetic noise. Deploying the sensor to a distance of twice the spacecraft's major axis was set as an achievable goal to mitigate the expected magnetic noise of the attitude control system.

3.3.2 CubeSat Platform Constraints

The CubeSat Design Specification was developed in 1999 by researchers at California Polytechnic State University (Cal Poly) and Stanford University's Space Systems Development Laboratory (SSDL), and has been periodically updated [*Mehrparvar et al.*, 2014]. Ex-Alta 1 is representative of CubeSats used in similar missions, and implements a standard three-unit (3U, ~10x10x30 cm) form factor which limits the longest possible section in the deployable magnetometer boom to less than 30 cm while in the stowed position, the boom design presented here a folded boom to achieve a deployed length of 60cm. Ex-Alta 1 is scheduled to be deployed by a NanoRacks CubeSat Deployer (NRCSD) aboard the International Space Station. The interface control document for the NRCSD [*NanoRacks LLC*, 2013] provides an additional mechanical constraint that no feature shall exceed 8 ± 0.9 mm normal to the surface defined by the rails of the spacecraft, to prevent collision with the CubeSat launcher. In application, this means that the stowed fluxgate sensor and boom cannot protrude more than 8.9 mm from the exterior panels of the spacecraft.

Modelling of the power available to the spacecraft showed that 270 to 5,000 mW orbit-average power would be available for instrument payloads depending on orbit parameters. The spacecraft would be capable of operating a payload which consumed less than 500 mW for at least 50% of the time in all orbits and for 100% of the time in most orbits [*Grey*, 2016]. The electronics for Ex-Alta 1 were implemented as stacked circuit boards conforming to the CubeSatKit PCB specification [*Pumpkin Inc.*, 2007], and providing connectors for ribbon cables to pass the main

spacecraft communication and power signals through the inter-stage region between the central and outer thirds of the spacecraft.

The various CubeSat specifications impose other requirements including: ensuring all parts remain attached to the CubeSat (no creation of additional space debris); restrictions on pyrotechnics and propulsion systems; Total Mass Loss (TML) outgassing less than 1%; Collected Volatile Condensable Material (CVCM) less than 0.1%; random and sinusoidal vibration testing; quasi-static acceleration tested to 10.8 g; thermal vacuum testing; and a bake test for three hours at 50 °C. These constraints directed our design primarily through reduction in mass and power consumption. They also led to the development of a novel CubeSat boom mechanism that lies flat against the spacecraft skin during launch, and is subsequently deployed to separate the sensor from the noisy electromagnetic environment of the spacecraft.

3.3.3 Current State of Magnetic Sensors for CubeSats.

The use of CubeSats as a platform for magnetic measurements is an emerging topic in the literature. Recent instrument developments tend to focus on two areas: miniaturizing traditional fluxgate magnetometer designs for CubeSat applications without overly compromising their measurement capability [*Ripka*, 2003]; or improving, calibrating, and compensating various types of small magnetoresistive and Hall Effect sensors to improve their scientific utility [*Ripka et al.*, 1999; *Brown et al.*, 2012, 2014; *Michelena*, 2013]. Combinations of these approaches are also possible. For example, the European Space Agency Service Oriented Spacecraft Magnetometer (SOSMAG) aims to take high fidelity measurements on larger spacecraft by combining one or two classic boom-mounted fluxgates with two small anisotropic magnetoresistance (AMR) sensors in the spacecraft body, to characterize and remove interference from the spacecraft [*Leitner et al.*, 2015].

Several groups are developing fluxgate sensors on integrated circuits [*Choi et al.*, 1996; *Robertson*, 2000; *Drljaca et al.*, 2003; *Texas Instruments Inc.*, 2016]. However, to date they have not reached the resolution and noise levels of a dedicated external fluxgate sensor. Commercial fluxgate sensors that could potentially be flown on CubeSats continue to improve, achieving noise of around 0.7 nT_{rms} at 12.83 sps [*Matandirotya et al.*, 2013]. The THEMIS mission incorporated low-mass fluxgate sensors (75 g), which having 70 mm diameter and 45 mm height [*Auster et al.*, 2009] were too large to be easily boom deployed from a CubeSat Platform. The best instrument to date

appears to be the Small Magnetometer In Low-mass Experiment (SMILE) developed by Forslund et al. [2007] which achieved 30 pT/√Hz at 1 Hz using a 20 x 20 x 20 mm cubic sensor based on three rod cores.

3.4 Instrument Overview

The CubeSat fluxgate magnetometer described here draws heritage from decades of Canadian instruments, starting with the terrestrial instruments designed by Narod and Bennest [1990]. This design was updated for the Canadian Space Agency Cassiope/e-POP mission as the Magnetic Field Experiment (MGF) [*Wallis et al.*, 2015], and was further modernized and improved as a principally digital instrument by Miles et al. [2013].

Fluxgate magnetometers [*Primdahl*, 1979] measure the static and low frequency vector magnetic field by modulating or gating the local magnetic flux, and measuring the induced electromagnetic force (EMF) in a sense winding. A ferromagnetic core, periodically driven into magnetic saturation at frequency *f,* is used to gate the local field, thereby inducing a signal at *2f* (and other harmonics) due to the non-linear magnetic permeability of the core as it enters magnetic saturation. In many instruments, including that presented here, magnetic feedback is used to null the magnetic field in the sensor, which linearizes and extends the measurement range of the instrument.

The sensor (Figure 3-3a) is a double wound ring-core design, similar to that of the Cassiope/e-POP design, using two custom miniature ferromagnetic ring-cores and occupying a volume of 36 x 32 x 28 mm. The sensor base and mount were manufactured from 30% glass filled polyetheretherketone (PEEK) plastic to provide a robust, thermally stable mount for the sense windings. The mass of the miniature sensor is 47 g (cf. 290 g on Cassiope/e-POP).

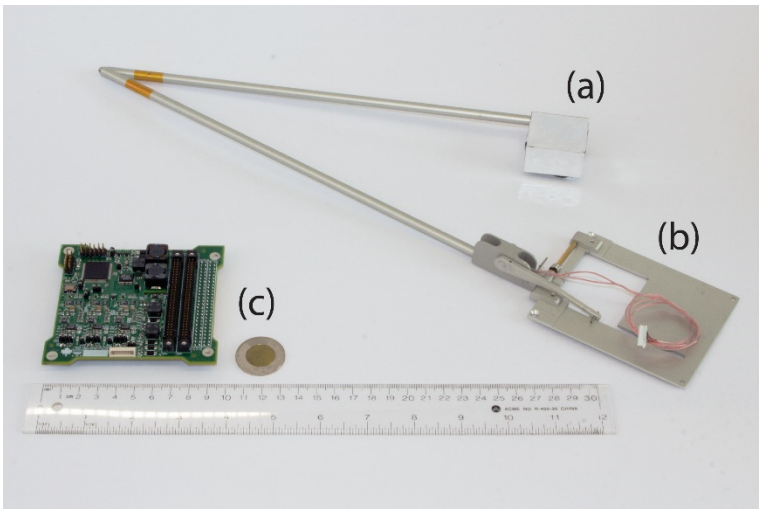

Figure 3-3: Sub-assemblies of the Ex-Alta 1 miniature fluxgate magnetometer payload comprising (a) a double-wound ringcore sensor, (b) a deployable 60 cm boom, and (c) a single associated electronics card.

The electronics have a low power consumption of 400 mW, which was achieved by moving traditional analog signal conditioning to digital processing. All electronics were fit on a single 10 x 10 cm circuit board compliant with the CubeSatKit PCB specification. Finally, a novel deployable boom was designed to occupy a single 10 x 10 cm exterior panel, stow along the outer surface of the spacecraft, and deploy the fluxgate sensor to a distance of 60 cm (Figure 3-3b). Table 3-1 summarizes the performance of the miniature fluxgate instrument.

Table 3-1: Characteristics and performance of the miniature, boom-mounted fluxgate.

Parameter	**Value**
Sensor Mass	47 g
Boom Mass	74 g
Electronics Mass	65 g
Sensor Dimensions	36 x 32 x 28 mm
Electronics Dimensions	96 x 91 mm
Boom Length	60 cm
Power Consumption	400 mW
Cadence	100 sps
Magnetic Range	±65,536 nT
Magnetic Resolution	35 pT
Noise Floor	150-200 pT/√Hz @ 1 Hz
RMS Noise	0.6-1.6 nT_{rms}

3.5 Detailed Instrument Design

Figure 3-4 shows the major components of one axis of the CubeSat fluxgate magnetometer. The Field Programmable Gate Array (Figure 3-4, FPGA) generates a 5 kHz drive signal (I_{drive}), which is power amplified (PA) and sent into the toroidal drive winding to periodically saturate the core. The AC current output of the sense winding (I_{sense}) is converted to a voltage (I/V), band pass (BP) filtered to block transformer coupled drive signal and to provide antialiasing, and is then digitized (ADC). The FPGA uses this signal as the input to a linear control loop, and outputs a digital offset. This is converted first to a voltage (DAC) and then (V/I) to a current ($I_{feedback}$), which is in turn sent back into the sense winding to provide magnetic feedback and to drive the field within the sensor towards zero on that axis. The data are timestamped based on a pulse per second (PPS) input from the GPS receiver, and is transmitted to the spacecraft via a serial data interface.

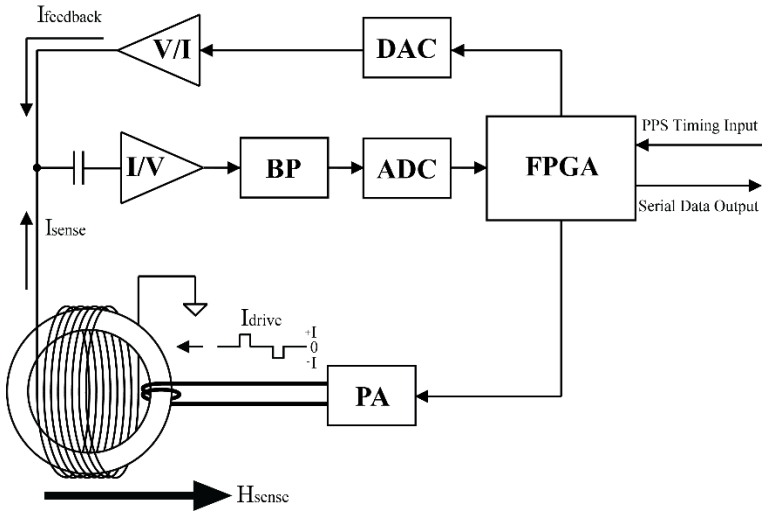

Figure 3-4: Schematic showing the major components of the fluxgate magnetometer. Adapted from Miles et al. [2013].

The presented instrument is a power, mass, and volume optimized version of a well-established Canadian fluxgate design [*Narod and Bennest*, 1990; *Miles et al.*, 2013; *Wallis et al.*, 2015]. This optimization is straightforward in principle but in practice, it is increasingly difficult to make the sensor uniform and symmetrical as its size is reduced. Such miniaturization driven challenges may be a broadly experienced challenge as more instruments are tailored to CubeSat platforms.

3.5.1 Sensor Assembly

The miniature fluxgate sensor is based on two custom ferromagnetic ring-cores, which are periodically driven into magnetic saturation using toroidal drive windings connected in series (Figure 3-5). A tuning capacitor across the drive windings provides a low-impedance source for

the peak current required as the cores go into magnetic saturation. Channels X, Y, and Z are each derived from orthogonal sense/feedback coils wound solenoidally around the two rings. Channel Z was designed to be derived from the serial connection of the two parallel z-axis coils. However, one z-axis coil was found to pick up excessive transformer coupled drive signal, so it was taken out of circuit, and each channel was derived from a single sense winding (Figure 3-5). Double winding each ring-core is an established technique [*Acuña and Pellerin*, 1969] to reduce power, volume, and mass by removing the need for a third ferromagnetic core.

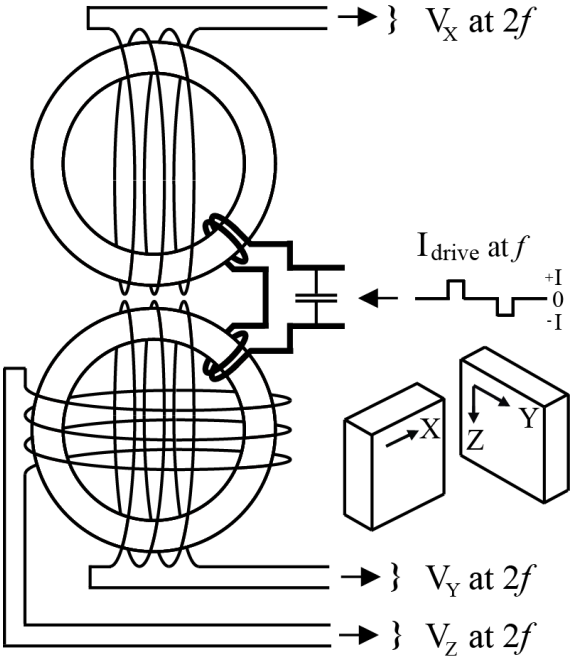

Figure 3-5: Wiring diagram for the fluxgate sensor showing two orthogonal (as inset) ring-cores. The combined sense/feedback windings sense the local magnetic field and provide magnetic feedback. Adapted from Wallis et al., 2015.

The ferromagnetic ring-cores used in the sensor were purpose built for the CubeSat application (Figure 3-6 top left). Each ring-core consists of a 7.4 mm outer diameter bobbin machined from Inconel 718 supporting a ferromagnetic foil. The ferromagnetic element was manufactured from a custom ingot of 6.0-81.3 Molybdenum-Nickel Permalloy. A 3 mm slice was cut from the ingot and homogenized at 1100 °C for one week. The material was then successively cold-rolled to a thickness of 100 μm. The foil was slit along the cold roll axis, to a width of 6.3 mm, matching the groove set into the outer surface of the Inconel ring. The foil strip was coated with a magnesium oxide insulating layer, spot welded to the ring, wound once around the ring, and spot welded to itself to secure it in place. The foil and Inconel ring assemblies were then annealed in a reducing atmosphere of 5% Hydrogen and 95% Argon. The pieces were rapidly inserted into the oven's

hot-zone and held at 1,100 °C for four hours with the intention of homogenizing the crystal structure. The furnace was cooled to 600 °C, and then ramped at -35 °C per hour to room temperature. The metallurgical process, foil thickness, and heat treatment were intended to minimize the magnetic noise floor of the ferromagnetic foil. The process is based on ongoing research into the origin of magnetic noise [*Narod*, 2014], and has subsequently been shown to be a suboptimal treatment. Work continues to optimize the core manufacturing process to achieve the expected < 50 pT / √Hz at 1 Hz level.

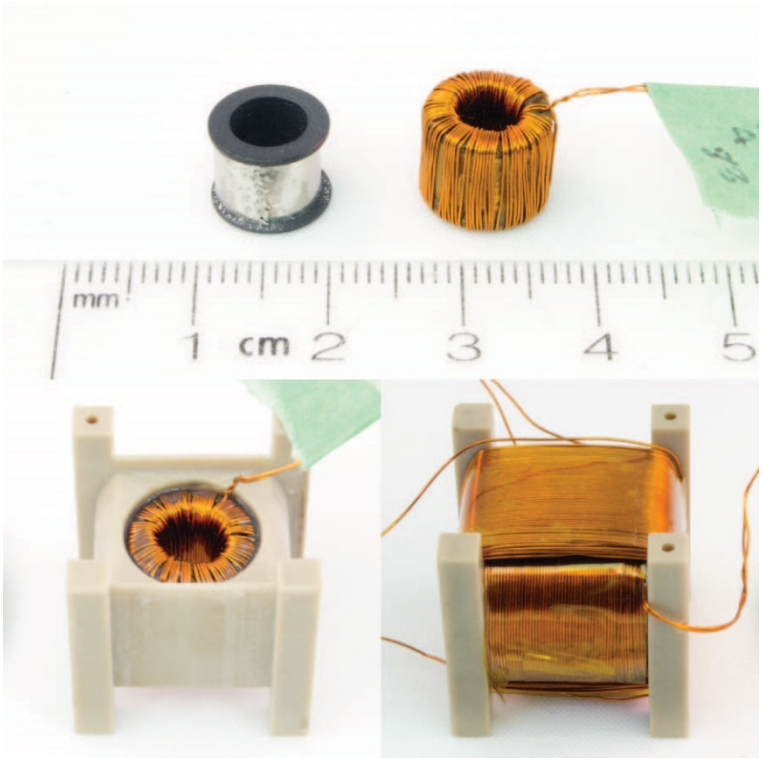

Figure 3-6: Construction of a miniature fluxgate sensor. (Top Left) Ring-core comprising silver colored 6.0-81.3 Molybdenum-Nickel Permalloy foil wound around a black Inconel 718 ring. (Top Right) Toroidal drive winding used to saturate the ferromagnetic core. (Bottom Left) Ferromagnetic ring-core and toroidal drive winding secured inside the 30% glass filled PEEK bobbin using vacuum tolerant epoxy. (Bottom Right) Two orthogonal sense/feedback windings wound solenoidally on bobbin.

Each ring-core was wound toroidally with a drive winding of 82 turns of AWG 32 enameled copper wire (Figure 3-6 top right). Kapton was placed between the ring-core and the wires to prevent shorting against the machined edge of the Inconel. Unfortunately, this caused bunching in the drive winding which may have contributed to coupling of the drive signal to the sensor output.

Each ferromagnetic ring-core and drive winding assembly was inserted into a 30% glass filled PEEK bobbin, which is used to support the two sensor windings (Figure 3-6 bottom left). The bobbins have a cylindrical cavity matched to the outer diameter of the drive windings. This allows

the ring core to be aligned at the center of the bobbin without applying significant mechanical stress. This is important because the magnetic noise of the permalloy foils has been observed to increase when the foil is stressed or deformed. Mechanical stress was further mitigated by using vacuum tolerant epoxy to secure the drive windings to the cylindrical walls of the bobbin, thereby locking the drive winding in place without creating a rigid bond to the ring-core. This mounting approach is intended to prevent the different coefficients of linear thermal expansion of the Inconel and 30% glass filled PEEK from stressing the permalloy foil as the materials expand and contract with temperature.

Two combined sense/feedback windings were wound solenoidally onto each bobbin (Figure 3-6 bottom right). The two orthogonal wire guides in the bobbin are inset, allowing a ~0.5 mm gap between the inner winding and the orthogonal outer winding. Each winding is ~260 turns of AWG 32 enameled copper wire in five layers. Kapton on the outside of each solenoid holds the wires in place.

The two complete double-wound bobbin assemblies are mounted at right angles, to measure three orthogonal projections of the vector magnetic field (Figure 3-7 top). The drive and sense/feedback wires are terminated on a small printed circuit board. This board also holds magnetically clean surface mount ceramic capacitors in parallel with the drive winding, which provide the peak saturation current. A magnetically clean resistor is used as a current-snoop for the drive winding. Finally, an integrated circuit acting as a temperature dependent current source is used to measure the sensor's temperature. Before launch, the sensor was wrapped in Kapton to protect the electronic components and covered in reflective metalized Mylar.

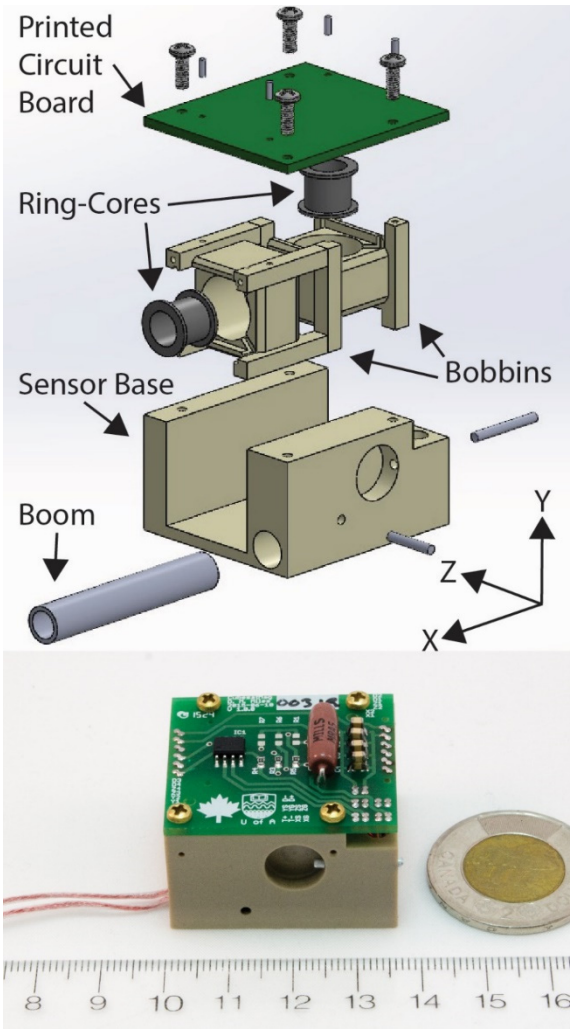

Figure 3-7: Miniature fluxgate sensor assembly. (Top) Blow up of the CubeSat sensor assembly showing major components. (Bottom) Miniature fluxgate sensor assembly occupying 36 x 32 x 28 mm and massing 47 g.

The double wound bobbin assemblies are pinned in place through the printed circuit board, which is secured to a 30% glass filled PEEK base. For flight, all pieces are cemented in place using vacuum tolerant epoxy. The boom is inserted into a hole in the base and pinned in place through the sidewall to prevent the sensor from rotating. Each of the sense windings is connected to one of three twisted pairs formed from AWG 34 enameled copper wire, which are then spiral bundled and inserted into a braided nylon mesh tube. The drive signal is carried by two additional AWG 34 twisted wire pairs connected in parallel, and the temperature measurement is carried by a third twisted pair which is bundled into a second braided Nylon tube. Both wiring bundles are fed through the sensor base, through the boom, and back to the spacecraft.

3.5.2 Excitation Current

This is a simplified and power optimized version of the drive circuit used in previous terrestrial and space design. The circuit has been re-tuned for the miniaturized sensor and the impedance of the custom miniature wiring harness. Figure 3-8 (top) shows the bridge circuit used to periodically saturate the ferromagnetic ring-cores. By alternately closing Field Effect Transistor (FET) pairs A+/B- and B+/A-, the FET bridge creates a 6.6 V_{pp} drive signal from a unipolar 3.3 V supply. Closing a FET pair charges the shunt capacitor at the boom end through two inductors connected in series, providing 2 mH. The charging capacitor increases the voltage across the drive windings, and hence the current through the drive windings. Eventually, the magnetic field created by the toroidal drive winding exceeds that which can be carried by one of the ferromagnetic cores, forcing it into magnetic saturation. As the first ring-core saturates, the inductance of that drive winding collapses, the voltage across it and the other drive winding spikes, and the shunt capacitor provides a low-impedance current source, which rapidly forces the second core into saturation.

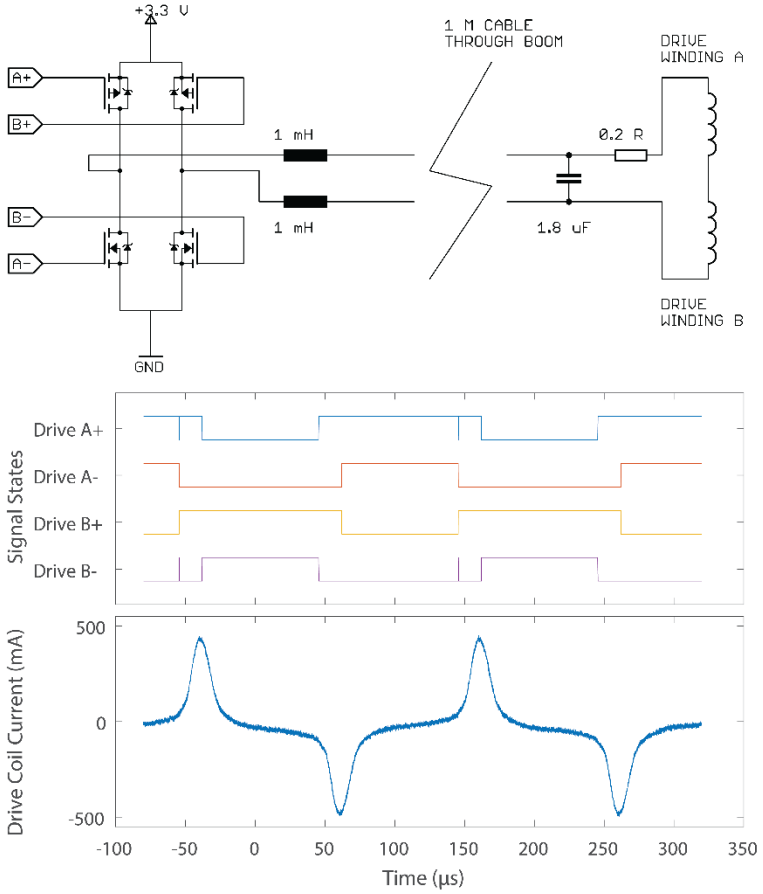

Figure 3-8: Fluxgate drive circuit. (Top) Field effect transistor bridge circuit used to periodically drive the ferromagnetic ring-cores into magnetic saturation. (Middle) Control lines for the FET bridge drive circuit. The transient features in Drive A+ and B- are artifacts of the logic probes used to capture the signals. (Bottom) Current pulses used to saturate the ring-cores.

Figure 3-8 (middle) shows the four control lines driving the FET bridge. A short dead-space between the signals creates break-before-make switches. This topology was tuned to create high amplitude, low duty cycle current spikes, as shown in Figure 3-8 bottom. The high peak current forces the ring-core into deep magnetic saturation to reduce magnetic noise, while the low duty cycle reduces the power required. The saturating ring-core changes the relative permeability inside the sense winding, thereby gating the ambient magnetic field. This in turn changes the flux through the sense winding, and creates EMF across the sense winding.

3.5.3 Analog Signal Conditioning, Digitization, and Processing

The output of the solenoidal sense winding is conditioned to isolate and amplify the fluxgate signal before digitization (Figure 3-9). A capacitor in series with the sense winding blocks any quasi-static signal, while passing the 10 kHz fluxgate signal. A transimpedance (current-to-voltage) amplifier holds the output of the sense winding in a virtual ground, flattening the frequency dependent sensitivity of the coil. A 10 ppm/°C temperature coefficient feedback 1,000 Ohm resistor minimizes the impact of temperature on the transfer function of the transimpedance amplifier.

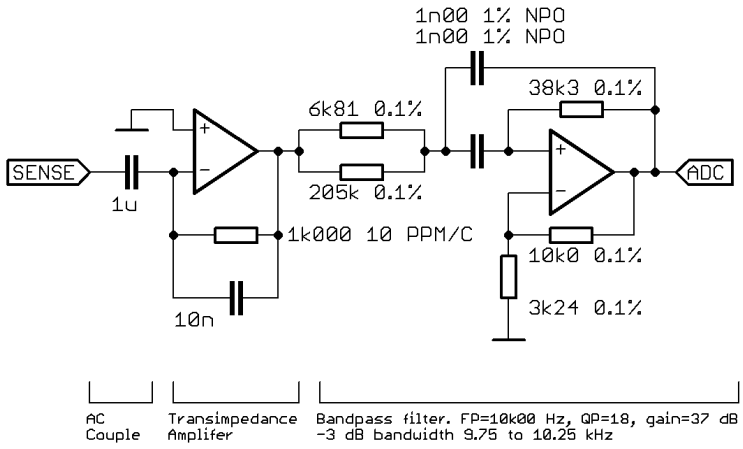

Figure 3-9: Analog conditioning of the sense winding output comprising a capacitive couple to block the quasi-static feedback current, a transimpedance amplifier, and a high Q band pass filter at the 2f fluxgate frequency.

The miniature fluxgate sensor was discovered to have significantly more drive signal contaminating the output of the sense winding compared to previous, larger instruments using 25.4 mm rings. The origin of this contamination is not clear but possibilities include: poorer symmetry in the smaller sensor, the imperfect toroidal drive windings, the alignment of the terminations of the ferromagnetic foil within the solenoidal pickup windings, stray field from the termination of the windings, and coupling in the sensor harnessing. Unfortunately, the drive signal was so large

that it dominated the output of the sensor. This limited the analog gain that could be applied, and risked saturating the analog-to-digital converter (ADC). A high Q band pass filter at the 10 kHz fluxgate frequency was implemented to suppress the 5 kHz drive interference, and to simultaneously boost the fluxgate signal. Figure 3-10 shows the amplitude and phase response of the implemented filter, which provides 37 dB of gain at the 10 kHz fluxgate frequency and a -3 dB bandwidth of about ± 200 Hz. This has the effect of suppressing the 5 kHz drive tone by 31 dB, compared to the fluxgate signal.

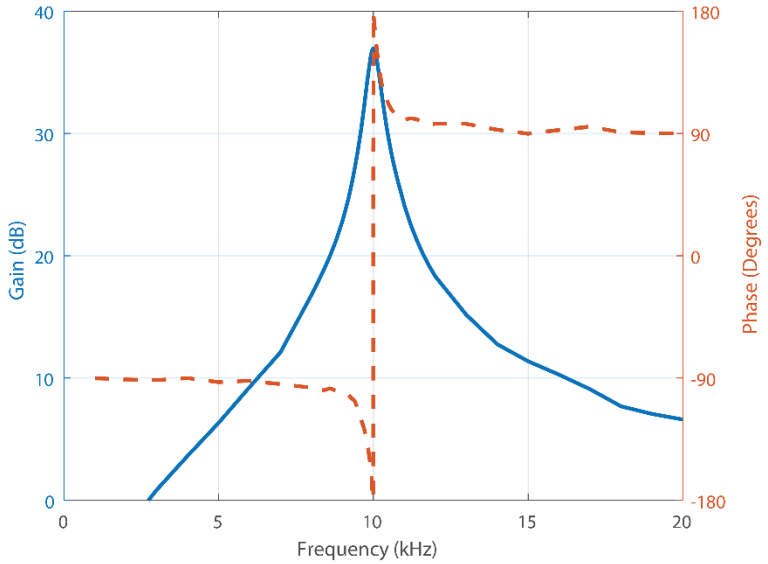

Figure 3-10: Frequency response of the 10 kHz band pass filter showing amplitude (blue solid line) and phase (red dashed line).

Figure 3-11 shows the output of the preamplifier (top) and of the band pass filter (bottom) with the different line colors corresponding to the applied static magnetic test signals ranging from +2,500 to -2,500 nT. The fundamental frequency and multiple harmonics are clearly present for both the drive signal and the fluxgate action. However, the band pass filter adequately isolates the fluxgate action.

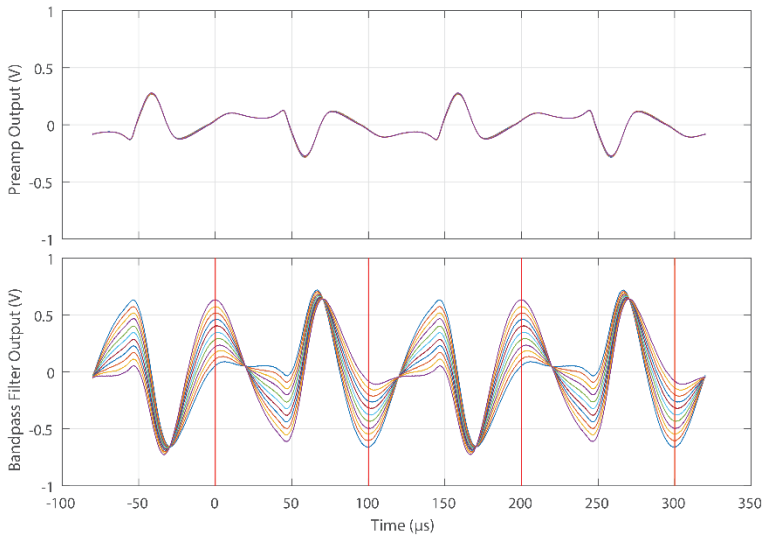

Figure 3-11: Superposed time series of the output of the preamplifier (top) and band pass filter (bottom) where the envelope of different colored traces shows the applied magnetic fields ranging from -2,500 to +2,500 nT. The output of the band pass filter is sampled by the analog-to-digital converter at the vertical red lines.

The output of the band pass filter is sampled by the analog-to-digital converter at the times indicated by the vertical red lines in Figure 3-11, creating a synchronous 10 kHz detector, which is phase, locked to the extrema of the fluxgate signal. One hundred sequential analog-to-digital conversions are averaged and truncated into a 16-bit measure of the residual magnetic field in the sensor. The least significant bit corresponds to ~30 pT, allowing the sensor to span a magnetic range of ±1,000 nT.

3.5.4 Magnetic Feedback

Digital magnetic feedback (Figure 3-12) is used to extend the magnetic range of each axis beyond the ± 1,000 nT provided by the forward signal path. A 16-bit digital-to-analog converter (DAC) creates a bipolar offset voltage, which is converted into an offset current by a transconductance amplifier. This current is fed back into the sense winding to drive the corresponding component of the magnetic field in the sensor towards zero. The transconductance amplifier is scaled such that the least significant bit of the digital-to-analog converter corresponds to 2 nT of magnetic feedback, thereby expanding the magnetic range of each axis to ±65,536 nT, or full Earth field. The digital-to-analog converter was selected to be noise free well below its 16-bit resolution, to avoid introducing noise through the digital feedback. The software allows the feedback to be updated by 2, 8, 32, 128, or 512 nT after each sample in order to keep the sensor and the forward loop within range.

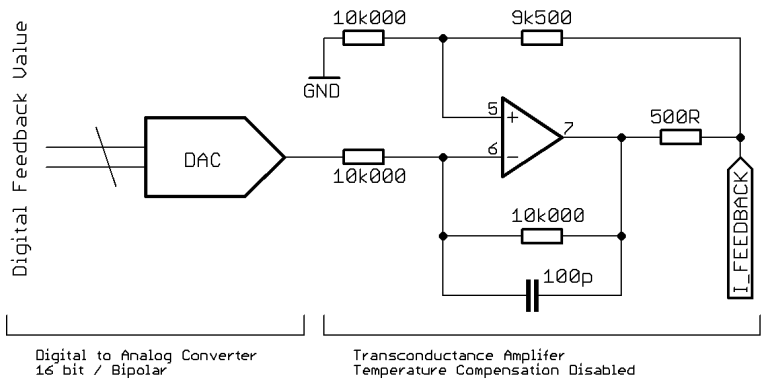

Figure 3-12: A 16-bit digital-to-analog converter and transconductance amplifier create a controllable feedback current scaled to 2 nT / bit, expanding the instrument's range to ± 65,536 nT on each channel.

The topology of the transconductance amplifier can be used to compensate for the change in sensor gain arising from the change in fluxgate sensor geometry with temperature (thermal gain sensitivity, nT/nT/°C). The transconductance amplifier could have been tuned to provide temperature compensation by exploiting the change in copper sense winding resistance with temperature [*Primdahl*, 1970; *Acuña et al.*, 1978], However, preliminary tests revealed that the thermal gain sensitivity varied substantially between the three axes, and this feature was not incorporated into the present design. These variations in thermal gain sensitivity imply that the miniature sensors have a more complex response than the principally linear response in previous larger ring-core sensor such as those used in Cassiope/e-POP.

3.5.5 Characterization and Calibration

The ratio between the digital-to-analog converter in the feedback circuit and the analog-to-digital converter for the sensor output was characterized for each measurement axis by placing the sensor in a five-layer mumetal magnetic shield, toggling each digital-to-analog converter by ±256 counts, and measuring the apparent change in magnetic field captured by the analog-to-digital converter. The absolute scaling of instrumental counts to magnetic units for each axis was done using a calibrated solenoid in a magnetic shield to apply 30 known static fields, and then fitting a linear trend to the measured values. Finally, the zeros of the instrument were estimated by flipping the sensor on each axis within the magnetic shield. The resulting calibration coefficients are summarized in Table 3-2.

Table 3-2: Linear calibration coefficients for the miniature fluxgate magnetometer.

	X	**Y**	**Z**
C_1 (DAC nT/bit)	1.75742	2.03184	1.93438
C_2 (ADC nT/bit)	-0.0353	-0.0267	-0.0302
C_3 (Sensor Zero nT)	39.4	-77.4	47.3

Data for each channel are therefore reconstructed as

$$B_{measured} = C_1 DAC + C_2 ADC - C3$$

In normal operation, the digital feedback circuit will hold the sensor in near-zero field. Consequently, the linearity of the magnetometer will be directly related to the linearity of the 16-bit DAC [*Linear Technology Corporation*, 2014] used in the circuit. This gives the instrument a typical (worst-case) integral non-linearity error of ±0.5 (2) LSB or approximately ±0.5 (4) nT in each component.

The dependence of sensitivity on frequency was tested by applying constant amplitude sinusoidal test signals with frequencies ranging from 0.1 to 40 Hz. The apparent magnetic signal was digitized on one channel, and the voltage applied to the solenoid on another channel. The gain dependence was estimated using the ratio of the RMS amplitude of the two signals, as measured using quantitative spectral analysis [*Heinzel et al.*, 2002]. The phase dependence was estimated using cross power spectral density. No significant loss of sensitivity was observed over this frequency range (Figure 3-13), reproducing the previously observed flat sensitivity obtained using an open-loop AC coupled transimpedance amplifier [*Primdahl et al.*, 1994; *Miles et al.*, 2013]. The slight -0.3 dB loss in gain above 10 Hz is likely due to the roll-off of the analog band pass filter.

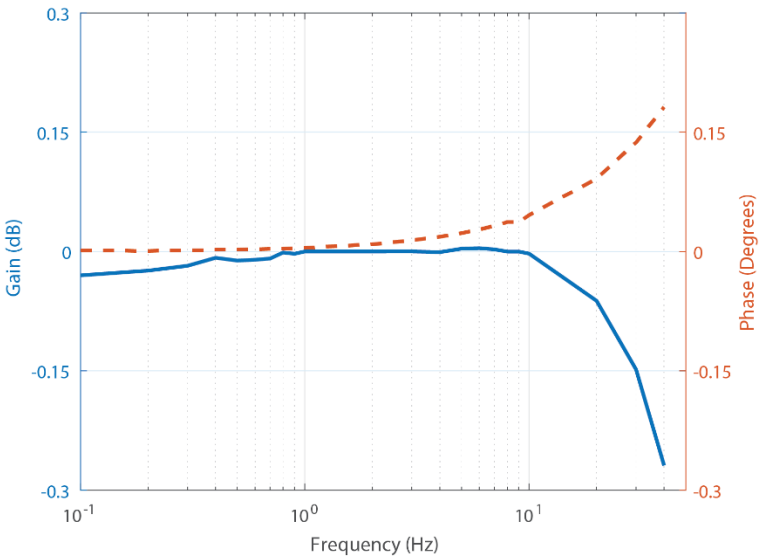

Figure 3-13: Phase and amplitude response of the instrument, showing minimal variation over frequency.

The power spectral density noise floor of the instrument was estimated using six minutes of data taken with the sensor inside a five-layer mumetal magnetic shield, and was found to range from ~150 to 200 pT/√Hz at 1 Hz for the three axes (Figure 3-14). The discrete spikes at 20 and 40 Hz are 60 Hz line noise aliased around the 50 Hz Nyquist frequency and 0 Hz due to the 100 Hz sample rate.

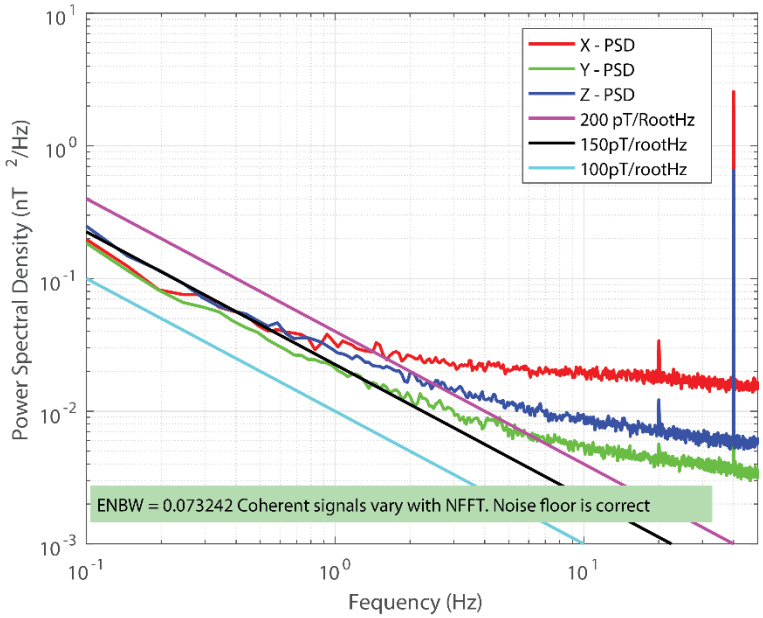

Figure 3-14: Power spectral density noise floor of the instrument ranging from 150 to 200 pT/√Hz at 1 Hz.

Figure 3-15 shows laboratory data illustrating the sensitivity and noise floor of the instrument. The sensor is inside a three-layer magnetic shield with a solenoid applying a magnetic test signal comprising a series of 50, 20, 10, and 5 nT peak-to-peak square waves.

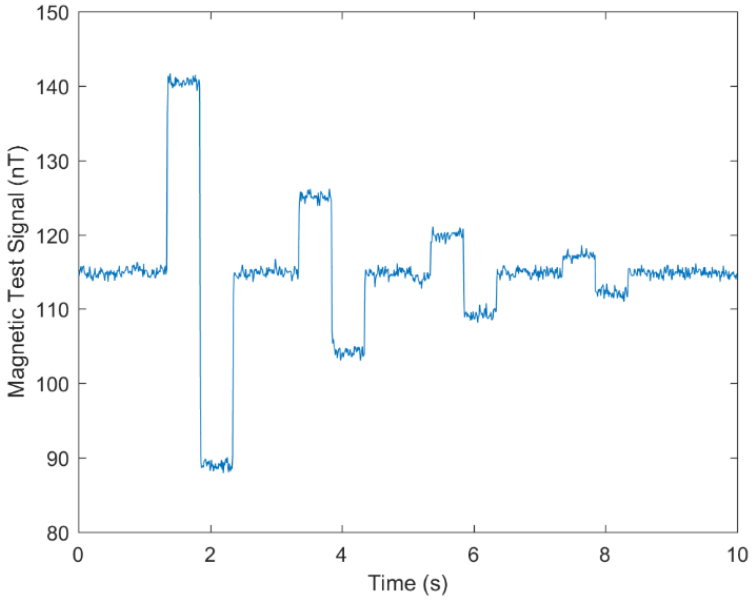

Figure 3-15: Laboratory data taken inside a three layer magnetic shield with a solenoid applying a magnetic test signal of 50, 20, 10, and 5 nT peak-to-peak square waves.

3.5.6 Magnetometer Boom

Figure 3-16 shows the 60 cm magnetometer boom assembly developed at the University of Alberta for the Ex-Alta 1 CubeSat. The mount and deployment mechanism occupies one ~10 x 10 cm external panel of the CubeSat. The boom comprises two 30 cm aluminum tubes stowed along the long axis of the 3U CubeSat body. When stowed, the boom is held in place by a single filament of ultra-high density polyethylene wire maintained under tension and in contact with a resistor. When current is passed through the resistor, the resulting heat melts the filament and releases the boom, which is then pushed outwards by a compressed spring. A captive spring acts as a joint for the two aluminum tubes, straightens the boom, and holds the outer tube in place. Figure 3-16 shows the boom and sensor in stowed (a) and deployed (b) positions, the sensor cabling (c) manufactured from custom twisted pairs of AWG 34 enameled copper wire retained in a braided nylon tube, and the captive spring (d), which both deploys and then stabilizes the elbow joint.

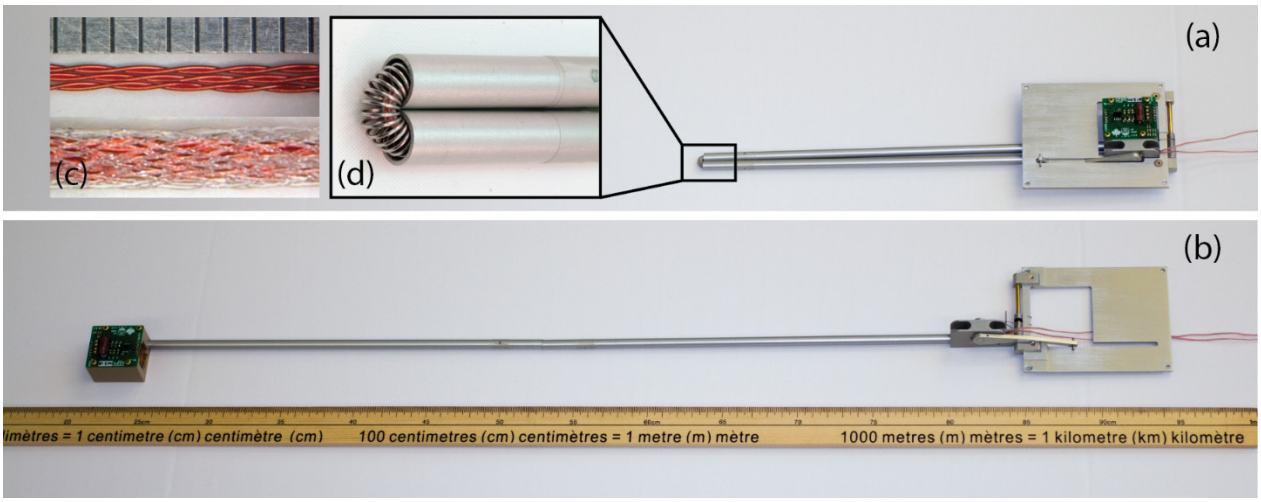

Figure 3-16: Magnetometer boom in stowed (a) and deployed (b) positions. Mounting panel has been flipped between pictures to expose the internal mechanisms of the boom. Inset (c) shows the sensor cabling comprising (middle) custom twisted pairs of AWG 34 enameled copper wire jacketed in a nylon sleeve (bottom). Each tick in (c) is 1 mm. Inset (d) shows the captive spring, which forms the elbow of the boom, and deploys the sensor and outer boom segment into position.

In the stowed position, the boom is mounted outside the spacecraft and held 1 mm above the solar panels. The sensor is stowed principally within the volume of the exterior panel, impinging only 12.7 mm into the interior volume of the spacecraft. This minimal volume intrusion allows it to be co-located with most standard CubeSat circuit boards, thereby preserving space for other spacecraft systems and instruments.

Figure 3-17 shows the threaded retaining post, which uncouples the sensor head as the boom, deploys, allowing the elbow joint to straighten (see movie provided as Supplementary). In the stowed position, the threaded retaining post tensions the sensor against the shoulder of the boom, and therefore against the spacecraft body. This secures the sensor, and allows the boom to survive the shock and vibration of launch.

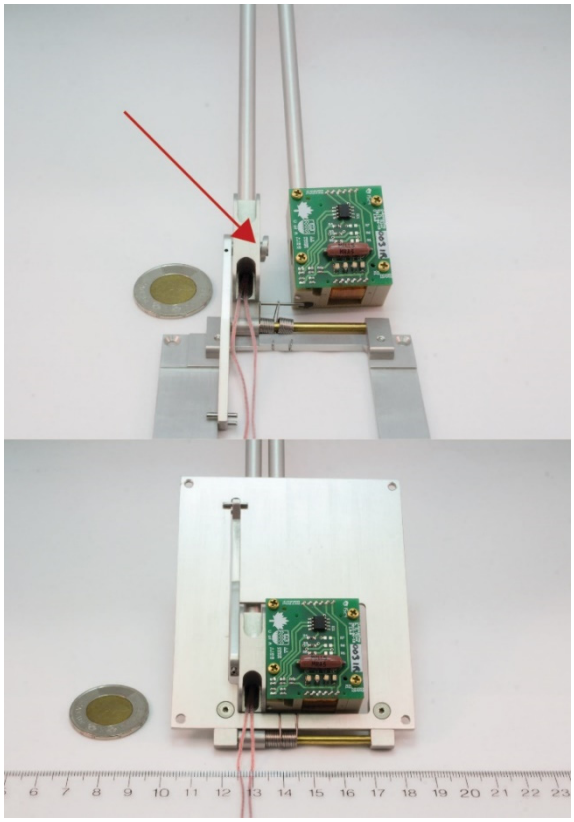

Figure 3-17: Boom assembly showing the sensor and shoulder joint uncoupled (top) and coupled (bottom). Arrow shows the threaded retaining post, which couples the sensor to the shoulder in the stowed position.

3.6 Spacecraft Noise Characterization

The rapid integration and launch schedule of the Ex-Alta 1 mission allowed limited opportunities to characterize the stray magnetic field of the spacecraft. The available time was focused on characterizing the noise generated by the one reaction wheel and the three magnetorquers in the Attitude Determination and Control System (ADCS). The integrated spacecraft was not permitted to leave the assembly cleanroom, so the spacecraft was tested in the magnetically noisy lab. Quantitative spectral analysis was used to estimate the dominant magnetic signatures of the ADCS in the presence of the other environmental noise sources.

Figure 3-18 shows the dynamic spectra of the sensor channels X, Y, and Z during the test. At the start of the test, the boom was deployed and the spacecraft was inactive. In region (a) the spacecraft was powered, but the ADCS was disabled. In region (b) the one reaction wheel was activated and set to 2 RPS, 5 RPS, and 20 RPS for five minutes each. In region (c) the magnetorquers were energized at 50% duty cycle (1 second repetition interval) on the spacecraft X, Y, and Z axes for five minutes each. The magnetometer boom was then stowed, and the reaction wheel and

magnetorquer activations were repeated–as above, in regions (d) and (e), respectively. The sensor Y channel saturated (> 65,536 nT) when the magnetometer boom was stowed, corresponding to the red shaded region in Figure 3-18.

Quantitative spectral analysis was used to estimate the magnetic noise at the relevant first, second, and third harmonics of each test, and is summarized in Table 3-3 for the boom-deployed configuration.

Table 3-3: Magnetic noise generated by the CubeSat reaction wheel and magnetorquers, as experienced by the sensor at the end of the 60 cm deployed boom.

Test Configuration	**Magnetic Noise (nT)**								
	First Harmonic			Second Harmonic			Third Harmonic		
	X	Y	Z	X	Y	Z	X	Y	Z
Wheel at 2 RPS	0.58	0.34	0.13	0.26	0.27	0.15	0.14	0.08	0.11
Wheel at 5 RPS	0.55	0.31	0.12	0.19	0.26	0.14	0.22	0.12	0.39
Wheel at 20 RPS	1.32	0.38	0.11	1.21	0.37	1.04	above Nyquist		
Torquer X	31.35	2.41	2.12	0.18	0.12	0.11	10.62	0.81	0.69
Torquer Y	4.04	1.07	30.00	0.17	0.11	0.12	1.44	0.35	10.15
Torquer Z	5.99	27.93	0.96	0.17	0.12	0.13	0.17	9.40	0.37s

The reaction wheel generated the most magnetic noise (about 0.6 nT at both 2 and 5 RPS) in the sensor X channel, and has reduced power in the second and third harmonic. The notably high estimated 1.32 nT level measured with the wheel at 20 RPS may result from Nyquist frequency folding of the third and higher harmonics aliasing power to 20 Hz. If so, this could be mitigated by improving the anti-alias filter in the magnetometer.

The magnetorquers have a one-second repletion period, with a configurable duty cycle of 0 to 80%. For this test, each torquer was set in sequence to a 50% duty cycle. At the boom end, this corresponded to a ~30 nT_{rms} square wave in the corresponding sensor axis, and to a ~1 to 6 nT_{rms} square wave in the other axes. The duty cycle of the magnetorquer creates a square wave with ~10 nT_{rms} in the third harmonic, and significant power in the higher odd numbered harmonics that are visible in the dynamic spectra shown in Figure 3-18.

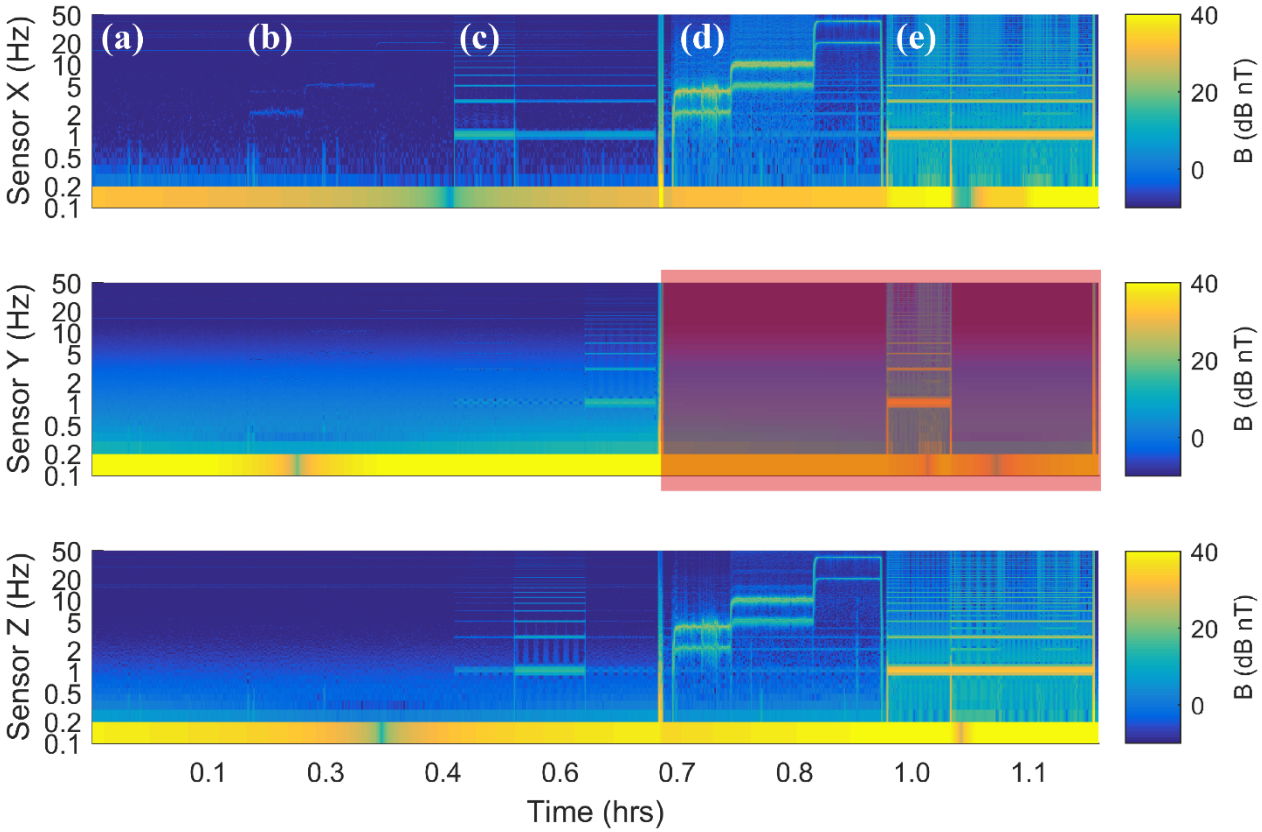

Figure 3-18: Dynamic spectra taken with the ADCS off (a), while exercising the reaction wheel (b) and (d), and while firing the magnetorquers (c) and (e). The magnetometer boom is deployed for (a), (b), and (c,) and is stowed for (d) and (e). The color scale corresponds to $10 \times log_{10}\left(\frac{B}{1\,nT}\right)$ *or dB nT.*

With the boom stowed, the sensor is directly adjacent to the ADCS subsystem, and the stray field is extremely large. The reaction wheel generated ~130 to 150 nT_{rms} at its rotation speed, and ~40 to 60 nT_{rms} at its second harmonic. The 1 Hz square wave generated by the magnetorquers exceeds the bandwidth of the magnetic feedback circuit. Consequently, the instrument is perpetually saturated, since it cannot track the transient field, which exceeds 7,500 nT peak-to-peak and affects all sensor axes.

Overall, the 60 cm deployable boom provides a surprisingly clean magnetic environment for the nominal case where the magnetometer is running and the spacecraft is preserving its pitch-orientation using the reaction wheel alone (i.e., region (b) in Figure 3-18). The apparent 0.6 to 1.3 nT narrow band tone of the reaction wheel is acceptable for many applications, and can likely be further mitigated in ground processing by either notch filtering or adaptive filtering. However, the ~30 nT square wave corresponding to the magnetorquers, with significant power in the higher odd

harmonics, significantly degrades the magnetic data. Fortunately, in the normal operations, the magnetorquers should never be activated while the magnetometer is running.

3.7 Data Reduction and Data Products

The miniature fluxgate magnetometer continuously produces 100 sps magnetic data whenever it is powered. The data are collected into one-second-long packets and transmitted to the spacecraft over the serial interface. Each packet contains an offset between the first sample and the 1 pulse-per-second output of the spacecraft's GPS unit. In orbit, the spacecraft will tag each packet with the absolute spacecraft time (which will be synchronized to GPS time once per orbit), and then place the fluxgate data in a first-in first-out ring buffer. Spacecraft software will low-pass filter and down sample the data to a nominal 1 sps product for routine transmission to the ground station as the survey data product. A burst-mode data-product comprising the raw 100 sps data, or at other programmable on-board cadence, can be pulled from the ring buffer. Burst mode data can either be down-linked using pre-scheduled time-tags uploaded from the ground segment, or can be retroactively pulled from the ring buffer (before it is overwritten by ongoing data collection) by request of the ground-segment after the science team has identified an interesting event in the downlinked survey data. An averaged spectral survey data product is planned to be implemented after launch and commissioning, once the instrument performance and orbit are characterized.

3.8 Example Application: Resolving Spatio-Temporal Dynamics of the Coupled Magnetosphere-Ionosphere System

Field-aligned currents are long-observed [*Birkeland*, 1908] and well-established [*Iijima and Potemra*, 1976] phenomena which couple energy and charge between the magnetosphere and the ionosphere. Instead of being measured directly, they are typically inferred from measurements of perturbations of the local magnetic field, and from assumptions about the scale, geometry, and spatial and temporal dynamics of the current system. Here, we use example measurements from the European Space Agency Swarm mission [*Friis-Christensen et al.*, 2008], which demonstrate that this coupled magnetosphere-ionosphere system can involve small scale spatio-temporal features which cannot be resolved by single, or even small numbers of spacecraft. However, a constellation of CubeSats in LEO with high-cadence magnetometers could be a powerful means to investigate the nature of this coupled system.

Ongoing research continues to expose both temporal and spatial complexity in the coupled magnetosphere-ionosphere system. The recently launched Swarm constellation deployed three spacecraft, of which two spacecraft (Swarm A and C) are on approximately parallel polar orbits with a cross-track separation of ~1.4 degrees. Figure 3-19 illustrates an auroral crossing on May 28, 2014 comparing the magnetic perturbations in the geographic east magnetic component from Swarm A and C. Figure 19 (top) is calculated from the 50 sps Level 1b data product, transformed into Geographic coordinates, and has a background field model [*Olson and Pfitzer*, 1977] removed using the IRBEM library [*Boscher et al.*, 2010]. Swarm C is lagged by 12 seconds to account for along-track spacing between the Swarm A and C spacecraft and angle of attack effects. Both spacecraft resolve the same large-scale magnetic features typical of field-aligned currents in the auroral region. However, the fine structure with ~100 nT amplitude varies dramatically between the spacecraft. This can be interpreted as one spacecraft intersecting fine filament currents, which are missed, by the other spacecraft, transient temporal fluctuations in the field-aligned current, the presence of large amplitude Alfvén waves, or some combination of the above.

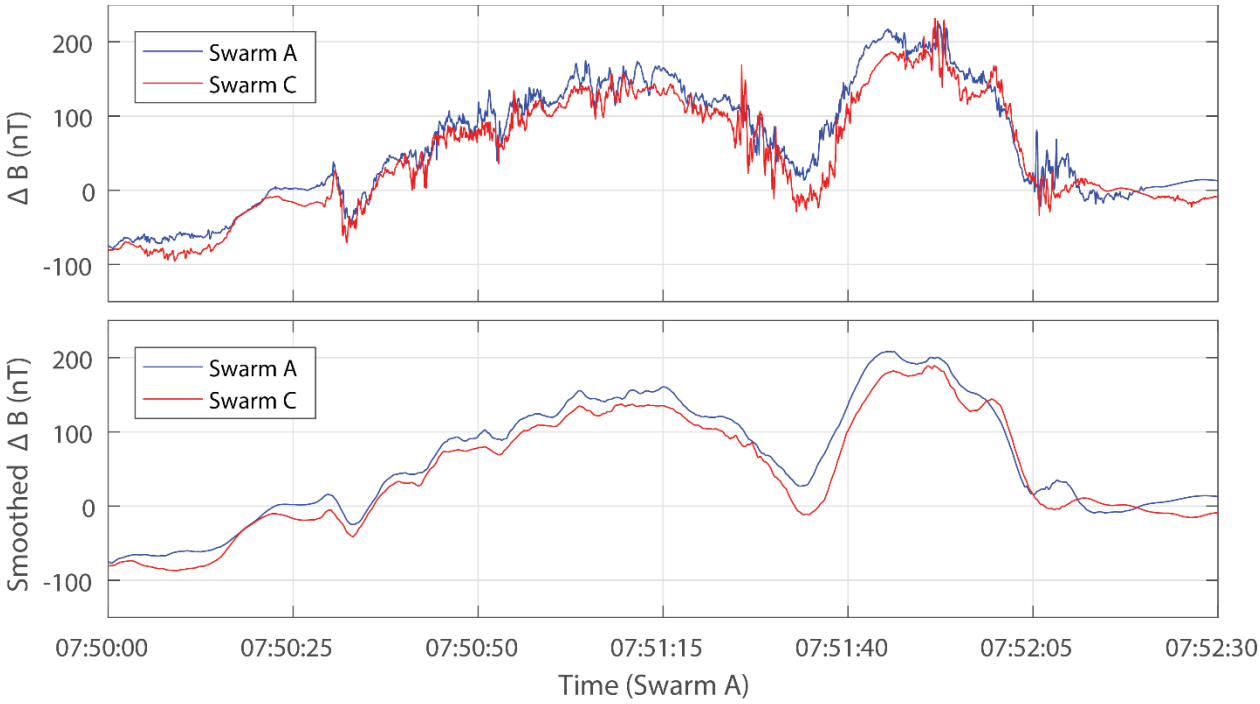

Figure 3-19: Cross-track magnetic perturbations from Swarm A and C spacecraft on May 28, 2014 (top). Data from Swarm C is lagged by twelve seconds to account for along-track separation and angle of attack. (bottom) Same but smoothed with a three second running mean to approximate the spin-averaging used in Gjerloev et al. [2011].

It is impossible to definitively determine what is happening in such an event with only two data points – let alone one as is traditionally done with single spacecraft estimates of field-aligned

current [*Lühr et al.*, 1994, 1996]. However, the dual spacecraft Swarm approach [*Ritter et al.*, 2013] represents an improvement over previous single spacecraft and/or lower cadence data where it would not be possible to determine that such complexity even existed.

This Swarm event also illustrates the potential for even modern constellation missions to neglect or misinterpret small scale phenomena if the magnetic field are spatially or temporally under-sampled. For example, Gjerloev et al. [2011] concluded that large scale field-aligned currents dominate energy transfer based on statistics of three months data from the three ST-5 spacecraft in a string-of-pearls constellation. However, this analysis was completed with 1 sps data spin-averaged at ~3 s, which the authors acknowledge makes the data questionable for scales below ~20 km due to the spacecraft orbital velocity in LEO.

Figure 3-19 (bottom) is smoothed with a three second running mean to approximate the effect of averaging at the three second spin-rate used in Gjerloev et al. [2011]. The local peak-to-peak amplitude of the signal is reduced by a factor of two at times around 07:51:25. Additionally, periodic structures, suggestive of a wave phenomenon, with peak-to-peak amplitudes around 100 nT are essentially removed at 07:51:55 and 07:52:10. If events such as the one presented are common, analyses such as Gjerloev et al. [2011] may be missing an entire regime of large amplitude signal due to under sampling.

A future CubeSat constellation mission could investigate the spatio-temporal nature of such phenomena using, for example, the four-spacecraft constellation concept shown in Figure 3-2. Spacecraft pairs a/c and b/d each have negligible cross-track separation allowing them to test for temporal variation in two orbital planes. Cross-comparing the measurements from each orbital plane also allow both an estimate of spatial structure, and, in the case that the magnetic measurements are inter-calibrated, can also be used to estimate the instantaneous FAC on the scale of the spacecraft separation using the multi spacecraft curlometer technique [*Ritter et al.*, 2013]. Most likely, the CubeSats in such a constellation would not have active propulsion; however, control of along-track separation using drag and natural orbital drift separation may allow the mission to investigate a variety of spatial scales and test for wave processes. Such a CubeSat constellation mission requires a sensitive fluxgate magnetometer such as the one whose design is outlined in this chapter.

3.9 Summary and Conclusions

A miniature boom-mounted fluxgate magnetometer has been developed with sufficient measurement fidelity to be scientifically useful, but small and low-mass enough to help enable future CubeSat magnetospheric constellation missions. The instrument comprises a sensor and 60 cm deployable boom, which stow along the outside of a 3U CubeSat and mount via a single exterior panel. The 150-200 pT/√Hz at 1 Hz noise floor of the fabricated sensor flown on Ex-Alta-1 was higher than expected and is significantly larger than that of other low mass sensors such as THEMIS (10 pT/√Hz but volumetrically larger) or SMILE (30 pT/√Hz). However, the performance should be sufficient to demonstrate the utility and initial feasibility of magnetic measurements from miniaturized fluxgate sensors on a CubeSat platform. Work is ongoing to produce lower noise cores for future fluxgate sensors by optimizing their manufacturing processes and the heat treatment of the permalloy foil. At the current noise levels, other technologies such as AMR sensors [*Brown et al.*, 2012; *Leitner et al.*, 2015] provide competitive performance and are well suited for CubeSat applications. However, with new core development work we believe that fluxgate sensors with significantly lower noise will be available for future applications. The electronics are implemented as a single 10 x 10 cm printed circuit board drawing 400 mW of power. The instrument produces 100 sps of vector magnetic data at 35 pT resolution over full Earth's field of up to ±65 μT. The instrument will be demonstrated on the Ex-Alta 1 CubeSat as part of the international QB50 mission.

Finally, we use Swarm data to illustrate the potential scientific utility of such an instrument, accommodated on a CubeSat, as the basis for a potential low-cost LEO constellation class mission to study magnetosphere-ionosphere coupling and eventually even high altitude magnetospheric constellation (MagCon) missions.

3.10 Acknowledgments and Data

Work on the project was supported by the Canadian Space Agency under grants 13STFAAB17 and 14SSTQB50. D. M. Miles is supported by an NSERC PGSD graduate scholarship, and by funding from the Canadian Space Agency. I. R. Mann is supported by a Discovery Grant from Canadian NSERC. I. P. Pakhotin is supported by the ESA STSE Swarm+ Innovation grant 4000114090/15/NL/MP awarded to the University of Alberta. This study makes use of data from the Swarm spacecraft mission, which is funded and managed by the European Space Agency.

Swarm data can be accessed online at: http://earth.esa.int/swarm. Data used to characterize the miniature fluxgate magnetometer may be acquired by contacting David Miles (david.miles@ualberta.ca). The authors wish to thank A. Vinagreiro and P. Zimmerman for machining components for the fluxgate sensor. Miles and Mann are the authors of a USPTO preliminary patent # 62/386,786 on a method of providing simultaneous attitude actuation and magnetic field sensing on a CubeSat using a modified fluxgate magnetometer.

Chapter 4: The Effect of Construction Material on the Thermal Gain Dependence of Fluxgate Magnetometers[4]

4.1 Abstract

Fluxgate magnetometers are an important tool in geophysics and space physics, but are typically sensitive to variations in sensor temperature. Changes in instrumental gain with temperature, thermal gain dependence, are thought to be predominantly due to changes in the geometry of the wire coils that sense the magnetic field. Scientific fluxgate magnetometers typically employ some form of temperature compensation, and support and constrain wire sense coils with bobbins constructed from materials such as MACOR machinable ceramic (© Corning) which are selected for their ultra-low thermal deformation rather than for robustness, cost, or ease of manufacturing. We present laboratory results comparing the performance of six geometrically and electrically matched fluxgate sensors in which the material used to support the windings and for the base of the sensor is varied. We use a novel, low-cost thermal calibration procedure based on a controlled sinusoidal magnetic source and quantitative spectral analysis to measure the thermal gain dependence of fluxgate magnetometer sensors at the part-per-million per degree Celsius level in a typical magnetically noisy university laboratory environment. We compare the thermal gain dependence of sensors built from MACOR, polyetheretherketone (PEEK) engineering plastic (virgin, 30% glass filled, and 30% carbon filled), and Acetal to examine the trade between the thermal properties of the material, the impact on the thermal gain dependence of the fluxgate, and the cost and ease of manufacture. We find that thermal gain dependence of the sensor varies as one half of the material properties of the bobbin supporting the wire sense coils rather than being directly related as has been historically thought. An experimental sensor constructed from 30% glass filled PEEK (21.6 ppm°C^{-1}) had a thermal gain dependence within 5 ppm°C^{-1} of a traditional sensor constructed from MACOR ceramic (8.1 ppm°C^{-1}). If a modest increase in thermal dependence can be tolerated or compensated, then 30% glass filled PEEK is a good candidate for future fluxgate sensors as it is more economical, easier to machine, lighter, and more robust than MACOR.

[4] This chapter is based on [*Miles et al.*, 2017b] with contributions as described in the preface for this thesis.

4.2 Introduction

Fluxgate magnetometers [*Primdahl*, 1970] are widely used in geophysics and space physics to measure static and low-frequency magnetic fields. However, they have long been known to be sensitive to the temperature of the sensor [e.g., *Trigg et al.*, 1971] with the dominant effect thought to be a change in gain with temperature due to variations in the geometry of the coils of wire used to sense the magnetic field. In particular, fluxgate sensors measure the static magnetic field by periodically driving a ferromagnetic element (core) into magnetic saturation, and then detecting the resulting change in the magnetic field as current or voltage in a surrounding sense winding. Negative magnetic feedback can be provided by driving current back into either the sense winding itself or into a separate feedback winding. Fluxgate magnetometers can be affected by temperature in a variety of ways, including: alteration of the magnetic properties of the core, mechanical stress on the core due to thermal mismatch between the ferromagnetic core and its support structures, change in the geometry of the ferromagnetic core, change in the geometry of the sense windings, changes in the geometry of the feedback windings, changes in the orthogonality or alignment of the sense windings, changes in the resistance of the sense or feedback windings, and/or changes in the drive current used to saturate the ferromagnetic core. However, the dominant factor has historically been taken to be the thermal expansion of the sense and feedback windings [*Acuña et al.*, 1978]. Specifically, expansion or contraction of the bobbin with temperature changes the winding density (turns of wire per unit length), modulating the sensitivity of the coil. Expansion or contraction also causes changes to the cross-section area of the sense coil which may introduce another temperature effect in low aspect ratio windings such as in miniaturised sensors [e.g., *Miles et al.*, 2016].

Primdahl [1970] and then Acuña et al. [1978] described a method whereby the temperature dependent resistance of the feedback winding was successfully used to compensate for temperature dependent variation in the feedback coil dimensions. Other geometries and coil topologies have been explored with the intention of minimising cross-axis effects by creating a “magnetic vacuum” within the sensor where the field is homogeneous and zeroed in all components [*Primdahl and Jensen*, 1982]. However, almost all designs rely on materials with ultra-low coefficients of linear thermal expansion such as quartz or MACOR machinable glass ceramic (© Corning), to minimise the thermal effects and to allow linear temperature compensation to be successful.

MACOR machinable ceramic has been used extensively and successfully in a variety of fluxgate applications. The specific materials used in sensor construction are often not provided in instrument publications. However, MACOR is explicitly mentioned or known to be used in: the NASA MAGSAT satellite [*Acuña et al.*, 1978]; the S100, STE and PC104 observatory magnetometers developed by Narod Geophysics Ltd. [*Narod and Bennest*, 1990] and used in both the Canadian CARISMA ground network [*Mann et al.*, 2008] and the US EMScope magnetotelluric network [*Schultz*, 2009]; the Danish Oersted satellite [*Nielsen et al.*, 1995]; the miniaturised SMILE instrument [*Forslund et al.*, 2007]; a prototype radiation tolerant fluxgate [*Miles et al.*, 2013]; and the Canadian Space Agency Cassiope/e-POP satellite [*Wallis et al.*, 2015]. Unfortunately, MACOR is expensive, difficult to machine, and brittle. Several authors have recently begun to use modern polyetheretherketone (PEEK) engineering plastic, either virgin or partially filled with glass or carbon, for fluxgate sensors [e.g., *Butvin et al.*, 2012; *Petrucha and Kašpar*, 2012; *Petrucha et al.*, 2015; *Miles et al.*, 2016]. PEEK derivatives should be a less expensive, easier to manufacture, and more robust alternative, albeit with a larger thermal expansion coefficient. The authors wanted to isolate and measure the effect on thermal gain dependence of changing different components of the sensor from MACOR to PEEK based plastic alternatives. This chapter presents laboratory results comparing the performance of six geometrically and electrically matched fluxgate sensors in which the material used to support the windings and for the base of the sensor is varied. The goal is to construct a sensor which is more robust, has a lower materials cost, and is easier and less expensive to manufacture without significantly compromising the thermal gain stability of the instrument.

4.3 Fluxgate Theory

4.3.1 Introduction

A fluxgate magnetometer [e.g., *Primdahl*, 1970] assembles a vector magnetic measurement from three solenoidal sense windings, each sampling an independent orthogonal component of the magnetic field. Each solenoid contains a ferromagnetic core which concentrates the ambient magnetic field, and which is periodically forced into magnetic saturation to modulate (gate) the field experienced in the sensor. This gating creates time varying magnetic flux, which in turn induces electromotive force in the solenoidal sense winding. Figure 4-1 illustrates one axis of a ringcore implementation: the ferromagnetic core is formed into a closed ring, the gated field

creates electromotive force in a rectangular solenoidal sense winding, and a toroidal drive winding minimises the transformer coupling between the saturating current in the drive winding and the resulting fluxgate signal output by the sense winding.

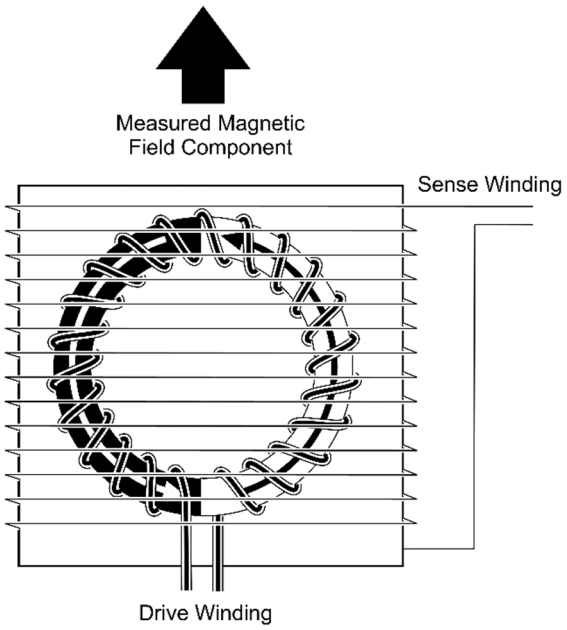

Figure 4-1: Schematic illustration of a single sensor axis of a ringcore fluxgate magnetometer. Image credit: Andy Kale

4.3.2 Expected Effect of Temperature-Induced Changes in Geometry

Global negative feedback can be used to linearize a fluxgate magnetometer, and to increase the range of magnetic fields that can be sensed without saturating the instrument. A feedback current, I_F, proportional to the measured magnetic field on each axis, is driven back into the sense winding to force the average magnetic field along that axis towards zero. Changes in the geometry of the sense windings will therefore create a thermal dependency in two ways: by affecting the forward gain of the solenoid as a sensor; and, more significantly, by affecting the feedback gain which scales the conversion of feedback current, I_F, into feedback flux, B_F. Following and expanding on the approach in Acuña et al. [1978], we approximate the sense winding as a finite solenoid (Figure 4-2) of n turns, length L, and radius R.

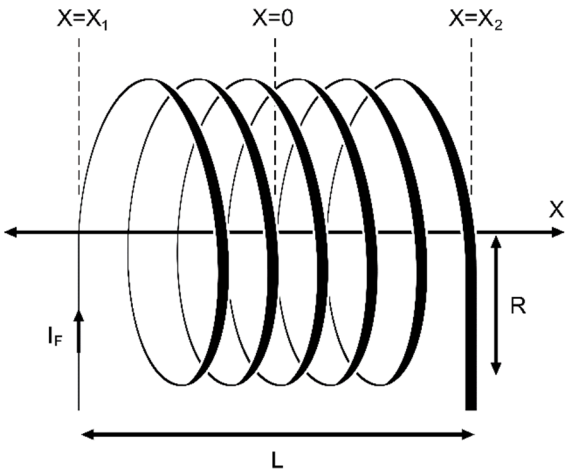

Figure 4-2: Approximating the sense winding as a finite solenoid of length L and radius R.

In this expanded Acuña et al. [1978] approximation, we consider the magnetic field along the axis of the solenoid, x. The field within the solenoid, B_F, is then dependent on the permeability of free space, μ_o, the current in the coil, I_F, and is given by

$$B_F = \frac{\mu_o n I_F}{2L}\left(\frac{x - x_1}{\sqrt{(x-x_1)^2 + R^2}} - \frac{x - x_2}{\sqrt{(x-x_2)^2 + R^2}}\right) \tag{1}$$

The sensor output will effectively be the volume integral of the magnetic flux inside the sense winding. This approximation ignores the complicating factor that flux is concentrated by the ferromagnetic ring as it periodically enters and leaves magnetic saturation. For simplicity, and given the limitations of this approximation, the overall trend of the sensor is assumed to match that of a point at the center of the coil on the solenoidal axis ($x_2 = -x_1$, $x = 0$). The field is then

$$B_F = \frac{\mu_o n I_F}{2L}\left(\frac{-x_1}{\sqrt{(-x_1)^2 + R^2}} - \frac{x_1}{\sqrt{(-x_1)^2 + R^2}}\right) = \frac{-\mu_o x_1 n}{\sqrt{(-x_1)^2 + R^2}}\frac{I_F}{L} \tag{2}$$

For simplicity, we define K to collect variables and note that $x_1 = R$ at the center of a square winding such as is shown in Figure 4-1. Therefore,

$$K = \frac{-\mu_o x_1}{\sqrt{(-x_1)^2 + R^2}} = \frac{-\mu_o x_1}{\sqrt{{x_1}^2 + {x_1}^2}} = \frac{-\mu_o}{\sqrt{2}} \tag{3}$$

which is constant with temperature. Note that the ferromagnetic ringcore shown in Figure 4-1 is bonded to a supporting metal ring that also has a temperature dependence. This introduces additional potential temperature dependencies in that the geometry of the ring may change, or the

ring may deform the geometry of the sense winding – both are ignored in this approximation. The effect of temperature, T, can be included by assuming that the length, L, of the coil is controlled by the bobbin on which it is wound. L will therefore vary around an assumed length, $l = L$ when $T = 0$, due to the coefficient of linear thermal expansion of the bobbin material, α_m.

$$L = l(1 + \alpha_m T) \tag{4}$$

Substituting Eq. (3) and Eq. (4) into Eq. (2) gives

$$B_F = \frac{K I_F}{l(1 + \alpha_m T)} \tag{5}$$

which recreates the result from Acuña et al. [1978]. To quantify the effect of temperature on instrument sensitivity, we define α_g, the coefficient of thermal gain dependence (ppm $°C^{-1}$), as the change in the measured amplitude of a fixed test signal with sensor temperature. This coefficient is then related to the sensor materials via their coefficients of linear thermal expansion, α_m (ppm $°C^{-1}$), which is a manufacturer provided estimate of the expansion or contraction of the material with temperature. Mathematically, α_g can be expressed as

$$\alpha_g = \frac{1}{B_F}\frac{dB_F}{dT} = \frac{l(1 + \alpha_m T)}{K I_F}\frac{-K\alpha_m I_F}{l(1 + \alpha_m T)^2} = \frac{\alpha_m}{\alpha_m T + 1} \tag{6}$$

α_m ranges from 8.1×10^{-6} to 85×10^{-6} for each of MACOR, the PEEK derivatives, and Acetal (see Section 4.4.1 for material datasheet references). Therefore, $\alpha_m T \ll 1$, and to a good approximation

$$\alpha_g = \frac{\alpha_m}{\alpha_m T + 1} \approx \alpha_m \tag{7}$$

This was first proposed by Acuña et al. [1978], and indicates that, to a first approximation, the coefficient of thermal gain dependence of the sensor should be equal to the coefficient of linear thermal expansion of the bobbin on which the sense winding is wound. These approximations are linked to the geometry of the sensor, and do not easily generalise. Other approximations are possible, including modelling the sense windings as a flat solenoid.

4.3.3 Electronic Temperature Compensation

Acuña et al. [1978] described a method of temperature compensating the feedback current, I_F, to correct the linear component of the sensor's temperature dependence. Figure 4-3 shows simplified feedback amplifier design, adapted from Acuña et al. [1978] and used in the instrument described in Section 4.4.2 where a transconductance amplifier has been modified such that the normally constant voltage-to-current transfer function is engineered to respond to the load resistance. The appropriate scaling of this transfer function allows, to first order, the effect of temperature on the load resistance offered by the sense winding to compensate for the effect of temperature on the sensor geometry.

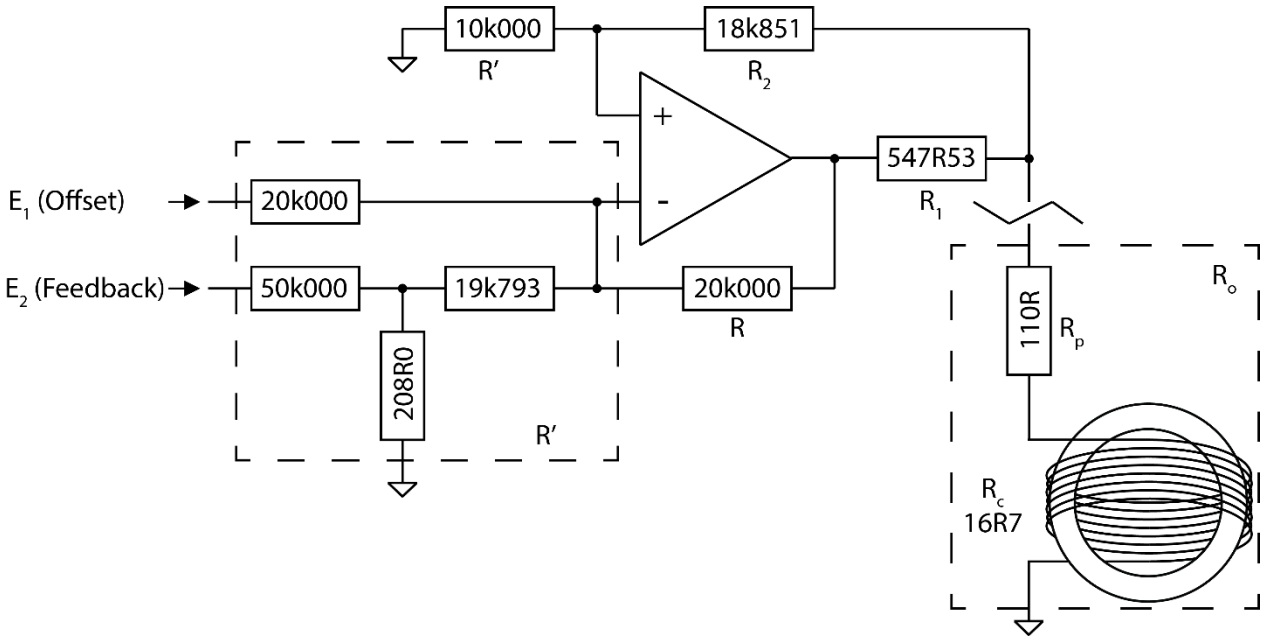

Figure 4-3: Modified transconductance amplifier providing temperature compensation to a single magnetometer channel.

The Acuña et al. [1978] design used platinum wire for the windings, whereas here the windings are copper in series with a platinum resistor. Detailed analysis of this circuit design was first prepared in an informal technical report [*Narod*, 1982] which has been reproduced and expanded in Appendix A. Based on Eq. (A10) in Appendix A, and expanding all terms using the nomenclature in Figure 4-3, the temperature compensation of the feedback amplifier is given by

$$\frac{1}{I_F}\frac{dI_F}{dT} = \frac{-\alpha_p \left[\frac{R_1 + R_2 - R}{R' + R_2}\right] R_o}{R_1 + \left[\frac{R_1 + R_2 - R}{R' + R_2}\right] R_o} \tag{8}$$

The coefficient of thermal resistivity of the sense/feedback winding and series platinum resistor is well approximated by ($\alpha_p = 3.93 \times 10^{-3}$ °C^{-1}).

4.4 Method

4.4.1 Experimental Fluxgate Sensors: Testing Different Structural Materials

Six geometrically and electrically matched fluxgate sensors were constructed where the material used to support the windings and for the base of the sensor was varied. Virgin PEEK, 30% glass filled PEEK, or 30% carbon filled PEEK are candidate materials to replace MACOR in new sensors due to their temperature stability, robustness, ease of machining, and cost. Acetal is included as a control with a large coefficient of linear thermal expansion.

Table 4-1 summarises the properties of the materials used in this experiment. The MACOR was all manufactured by Corning and the manufacturer's datasheet is assumed to apply to all samples. Three PEEK materials were procured from Professional Plastics (http://www.professionalplastics.com): virgin PEEK (SPEEKNA2.000D), 30% glass fiber PEEK (SPEEKGL30NA.500), and 30% carbon fiber PEEK (SPEEKCF30.375). The acetal (Delrin) sensor used existed from an earlier experiment so the exact plastic used in its construction is unknown and hence no manufacturer's datasheet was available. References values for general purpose acetal were assumed [*Oberg*, 2012]. Properties for the Inconel X-750 used to support the ferromagnetic core were taken from several sources including the Special Metals Group of Companies datasheet (© Special Metals Group of Companies, Unified Numbering System for Metals and Alloys reference UNS N07750).

Table 4-1: Properties of the materials used in the sensors.

Material	**Coefficient of Linear Thermal Expansion (ppm °C^{-1})**	**Young's Modulus (GPa)**	**Density (g/cm^3)**
MACOR	8.1	66.9	2.52
30% Carbon PEEK	18.0	9.7	1.41
30% Glass PEEK	21.6	6.9	1.51
Virgin PEEK	46.8	3.5	1.31
acetal	85.0	3.0	1.41
Inconel X-750	12.6	214	8.28

All the sensors in this experiment use the physical dimensions, design, and construction of the Narod Geophysics Ltd. STE magnetometer [*Narod and Bennest*, 1990], with three ringcore sensors mounted orthogonally on a common base (Figure 4-4). This matches the geometry used by Acuña et al. [1978].

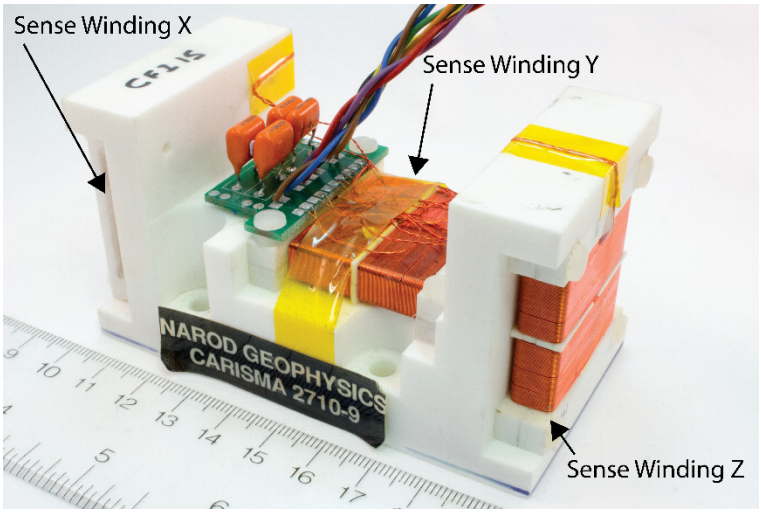

Figure 4-4: The Narod Geophysics Ltd. STE observatory magnetometer constructs a measurement of the vector magnetic field from three orthogonal sense windings.

The magnetic flux experienced by each of the three sense windings is varied by periodically saturating a 25.4 mm ferromagnetic ringcore composed of Permalloy foil wrapped on an Inconel x750 support. The ringcore is covered with a single layer of Kapton, and then wrapped toroidally with approximately 350 turns of Belden© 8056 AWG 32 magnet wire to form the drive winding used to saturate the ringcore. The toroidally wound ringcore is positioned on a centering disk within a rectangular bobbin. The outside of the bobbin supports a separate solenoidal winding, made from 360 turns of Belden© 8056 AWG 32 wire in two sections (Figure 4-5), which serve as both the sense and feedback coils. Figure 4-5 shows the length, L, defined by the two channels in the bobbin that contain the parallel sense windings. This length is analogous to that shown schematically in Figure 4-2.

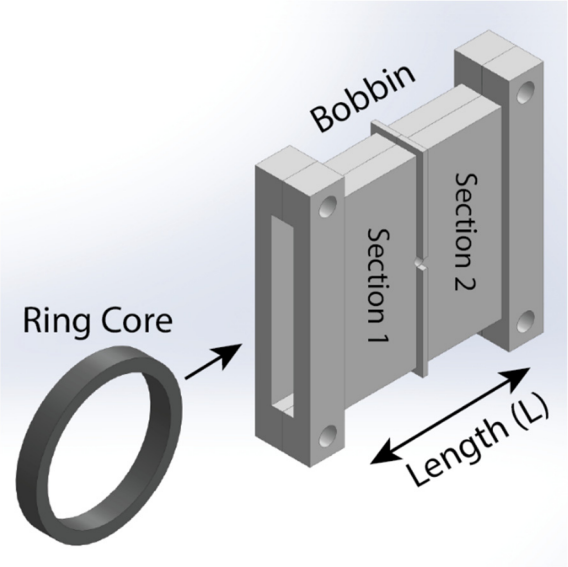

Figure 4-5: Sensor axis constructed from a ferromagnetic ring core with a toroidal drive winding inserted in a bobbin which supports the combined sense/feedback windings.

Figure 4-6 shows the six sensors used in this experiment. The name, composition, and roll in the experiment are shown in Table 4-2.

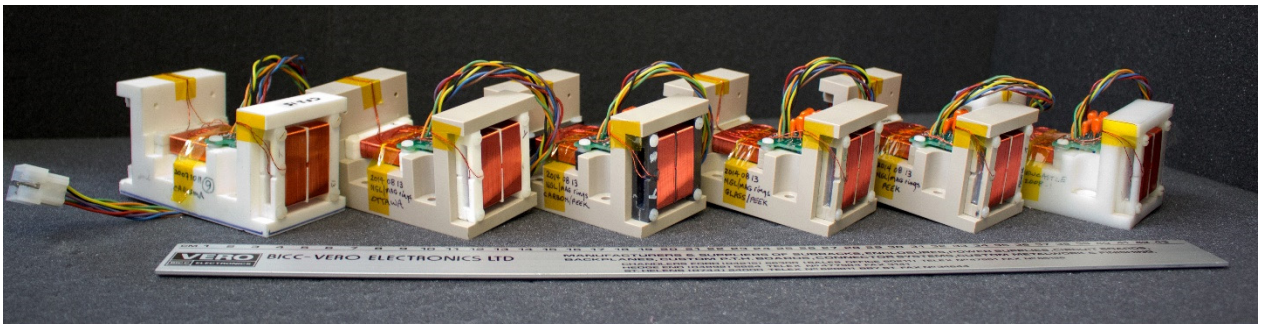

Figure 4-6: Fluxgate sensors used in this experiment: (Left to Right) MACOR Bobbin / MACOR Base, MACOR Bobbin / PEEK Base, Carbon PEEK Bobbin / PEEK Base, Glass PEEK Bobbin / PEEK Base, PEEK Bobbin, PEEK Base, acetal Bobbin / acetal Base. Note the various colours of material used in the winding bobbins and the base. For example, third from left is Carbon PEEK Bobbin / PEEK Base, distinguished by charcoal-coloured bobbins. The 914.4 mm long ruler is included for scale.

MACOR is considered the standard reference material for this experiment. A standard STE fluxgate sensor constructed from a MACOR bobbin and a MACOR base (referred to as MACOR/MACOR) was therefore used as the reference against which to compare the other sensors. A MACOR sensor on a virgin PEEK base (MACOR/PEEK) was constructed to distinguish between the effect of the change in dimensions of the sense winding and the change in orthogonality of the three sense windings due to deformation of the base. Three sensors were constructed with virgin PEEK bases and winding bobbins constructed from each PEEK type: virgin PEEK (PEEK/PEEK), 30% carbon filled PEEK (Carbon/PEEK), and 30% glass filled

PEEK (Glass/PEEK). A pre-existing sensor with an acetal base and acetal sense windings (acetal/acetal) was used as a negative control due to its known poor temperature stability (large coefficient of linear thermal expansion).

Table 4-2: Sensors used in this study and their makeup.

Sensor Name	**Bobbin Material**	**Base Material**	**Role in Experiment**
MACOR/MACOR	MACOR	MACOR	Reference Instrument
MACOR/PEEK	MACOR	PEEK	Discriminate between bobbin and base effects
Carbon/PEEK	30% Carbon PEEK	PEEK	Quantify performance of bobbin material.
Glass/PEEK	30% Glass PEEK	PEEK	Quantify performance of bobbin material.
PEEK/PEEK	PEEK	PEEK	Quantify performance of bobbin material.
ACETAL/ACETAL	acetal	acetal	Control with poor thermal stability.

4.4.2 Fluxgate Electronics

All the sensors in this experiment were driven and sampled by a single, unmodified set of STE magnetometer electronics. The STE magnetometer uses a classic second harmonic analog fluxgate design [e.g., *Geyger*, 1962], with its range expanded by the addition of variable offset feedback current (Figure 4-7). The ferromagnetic ring core is driven at a fundamental frequency f = 15.625 kHz, creating a fluxgate signal at $2f$ = 31.250 kHz. The voltage from the pickup windings is capacitively coupled to block any quasistatic feedback current, and is bandpass filtered twice at $2f$ using tuned passive resistor, inductor, and capacitor (RLC) filters. A phase locked analog switch inverts every other half wave period, creating a synchronous detector to demodulate the sensor output. Finally, a low pass filter and analog integrator create an analog voltage proportional to the magnetic field in the sensor, which is then captured by the analog to digital converter (ADC).

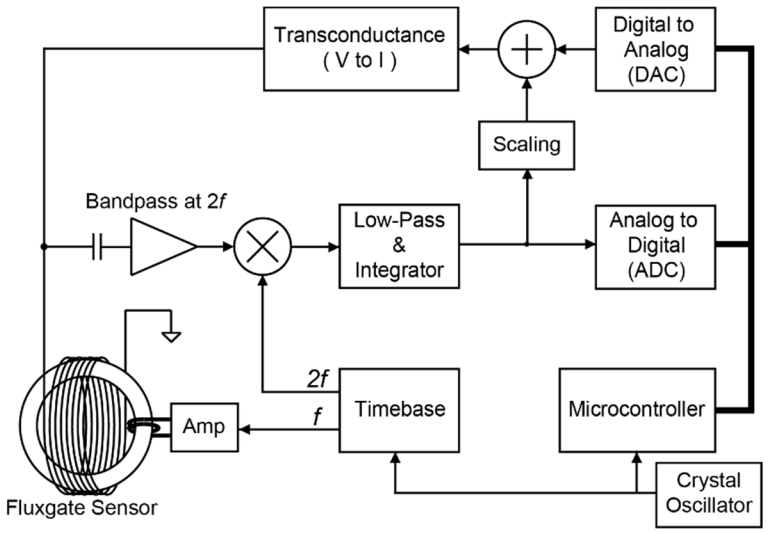

Figure 4-7: Single channel block diagram of the fluxgate magnetometer. Adapted from Wallis et al. [2015].

This output voltage is attenuated using a resistor T-network (Figure 4-3), and is summed with an offset voltage from the digital to analog converter (DAC) to create an analog feedback voltage. A modified transconductance amplifier (Appendix A) converts this voltage into a temperature compensated feedback current that is driven back into the pickup windings, nulling the magnetic field in the sensor. The global negative feedback loop, made up of the analog output of the sensor and the applied offset, is thereby temperature compensated by the transconductance amplifier. The measured value of the magnetic field is then the scaled sum of the offset applied with the DAC and the residual field digitised by the ADC.

The feedback amplifier in the STE magnetometer should give a temperature correction of 19.1 ppm °C^{-1} using Eq. (8) and the resistor values from Figure 4-3. This is approximately twice the correction suggested by the Acuña et al. [1978] calculation for the standard MACOR/MACOR sensor ($\alpha_g \approx \alpha_m = 8.1$ °C^{-1}). This correction was determined empirically from temperature testing completed in the 1980s. The experiment completed here examines the validity of both the temperature compensation applied by the modified transconductance amplifier and the Acuña et al. [1978] approximation of sensor's temperature dependence.

4.4.3 Experimental Setup

Accurately measuring the effect of temperature on fluxgate performance is technically challenging. The sensor assemblies have both sufficiently high thermal mass and low thermal conductance that the cooling and heating cycles must be slow (hours) to ensure that the sensor

temperature is homogeneous, and that the temperature probe is at the same temperature as the sensor itself. On these timescales, the natural variations in the Earth's magnetic field are large compared to the thermal effects being characterized. The sensor can be isolated from the Earth's varying field using expensive purpose-built nested high-permeability shields. However, temperature variations can change the dimensions of the shields, causing variation in the leakage field that penetrates the shield. Temperature characterisation is usually completed by either: placing a calibration coil inside a thermally regulated chamber within a magnetic shield, and ensuring that the fixtures are thermally isolated (e.g., the temperature test facility at the Magnetometer Laboratory at the Institute for Space Research in Graz, Austria); or in a magnetically quiet location with active compensation for Earth field variation (e.g., National Resources Canada {NRCan} Geomagnetic Laboratory Building 8 in Ottawa, Canada).

Here, we demonstrate a novel and low-cost method of measuring thermal gain sensitivity at the ppm $°C^{-1}$ level in an uncontrolled, magnetically noisy laboratory using a simple controlled sinusoidal source and apply the technique to characterising and comparing sensor constructed from different materials. As a fluxgate sensor under test changes temperature, its gain is affected causing the measured amplitude of the constant test signal to vary. Quantitative narrow frequency band spectral analysis is used to isolate and measure the apparent amplitude of the test signal, irrespective of other laboratory magnetic noise sources.

A thermally insulating box was constructed from 2" thick extruded polystyrene rigid foam insulation with a double layer base and removable lid, creating a controlled temperature environment for the fluxgate sensors. Four foam tabs were glued to the floor of the box to provide a repeatable placement and alignment location for each fluxgate sensor. The analog sensor cable was passed through a hole in the sidewall of the box and was wrapped in additional insulation to reduce heat flow. The fluxgate electronics provide an analog input for a sensor temperature measurement. A common Analog Devices LM34 temperature sensor integrated circuit, on a small separate printed circuit board, was used to measure temperature for all six experimental sensors. The LM34 was taped to the base of each sensor, adjacent to the sense coil aligned with the sinusoid magnetic test signal.

Approximately 1.1 kg of dry ice was used to cool the sensor for each trial, to ensure comparable thermal cycles. This cooled the sensor to approximately -40 °C in about four hours, when the

majority of the dry ice had sublimated and the temperature stabilised. The sensor warmed back towards room temperature (~21 °C) over the following 20 hours, reaching about 15 degrees before the experimental run would be terminated and reset. The temperature of the electronics was monitored by a second temperature sensor built into the STE magnetometer electronics, and was measured to vary by less than ± 1°C during the period of most experimental runs, with a worst case of ± 2°C .

Figure 4-8 shows the sensor under test in the insulating foam box. The lid, the plastic bag, and the desiccant have been removed for the photograph. Fluxgate data were gathered during the warming period of each experimental run. The temperature was cycled three times for each measurement axis, to check the consistency of the results and to estimate the error in the measurement.

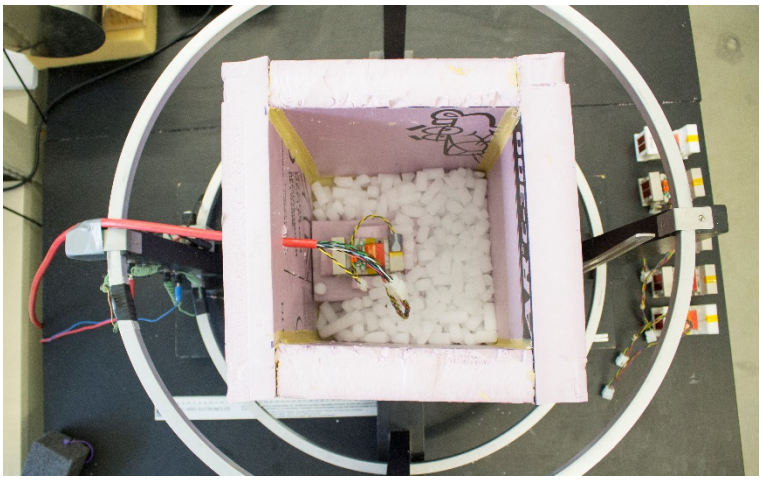

Figure 4-8: Sensor placed in a foam box within a Helmholtz coil. Dry ice was used to chill the sensor, and measurements were taken after the dry ice had sublimated and the sensor was slowly warming. The foam lid, plastic bag, and desiccant have been removed for the photograph.

Figure 4-9 shows the experimental setup. The controlled source magnetic test signal was generated by placing the sensor, in the insulating foam box, inside a Helmholtz coil consisting of two circular 66.4 cm diameter coils of ~54 turns, each with a total series resistance of 3.2 ohms. A 5k000 0.2 ppm $°C^{-1}$ resistor was placed in series with the coils. A 12 V_{rms} at 1 Hz sine wave from a Stanford Research DS360 ultra low distortion function generator created a 234 nT_{rms} test signal that was used for all sensor tests.

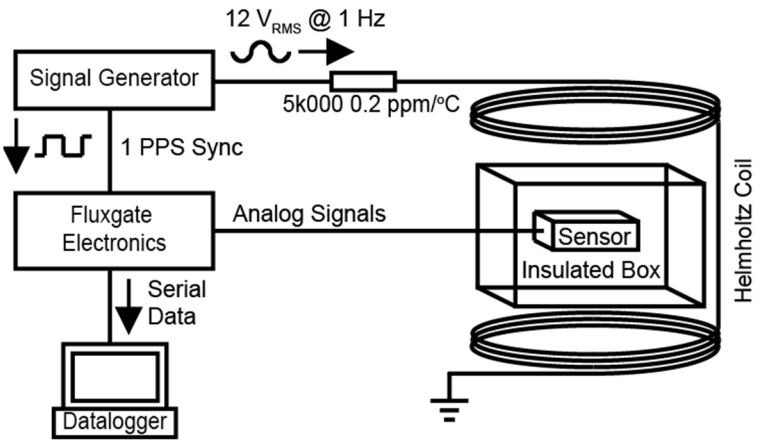

Figure 4-9: Experimental setup - each sensor was placed in an insulating foam box within a Helmholtz coil. The coils were driven with a sinusoidal magnetic test signal which was phase locked to the magnetometer electronics using the 1 pulse per second GPS timing input. Dry ice was used to cool the sensor and measurements were taken as the sensor warmed. The sensitivity of the sensor changes with temperature causing the measured amplitude of the constant test signal to vary with the sensor's temperature.

The small temperature coefficient of resistance (0.2 ppm $°C^{-1}$) of the resistor was intended to reduce the effect of the much larger temperature coefficient (3930 ppm $°C^{-1}$) of the copper wire in the Helmholtz coil. The stable series resistor limits the change in the applied signal due to the worst-case ± 2°C room temperature variation to

$$\frac{5000\ \Omega \times 0.2\ ppm\ °C^{-1} \times \pm 2\ °C + \ 3.1\ \Omega \times 3930\ °C^{-1} \times \pm 2\ °C}{5000\ \Omega + \ 3.1\ \Omega} = 9.8\ ppm \qquad (9)$$

The combined temperature coefficient of resistance of the copper coil and series resistance should contribute no more than

$$\frac{9.8\ ppm}{15\ °C - \ (-40\ °C)} = \ 0.2\ \text{ppm}\ °C^{-1} \qquad (10)$$

over the 55 °C temperature range in the experiment.

Some experimental runs were contaminated due to severe local interference such as construction crews vibrating the building. However, useful data were obtained for greater than 80% of trials despite the presence of typical ambient magnetic noise in the University laboratory environment during the calibration tests.

Figure 4-10 shows the daily temperature variation of a sensor under test. Each morning, the dry ice was added to the foam box to start the sensor cooling. The warming rate was slow near both the minimum and room temperatures. This generated a large amount of data that dominated the fit

line, compared to the middle temperature range where the rate of warming was faster. Therefore, data collection for each run was started at 5 °C above the minimum observed temperature. Similarly, the experiment was timed to end when the sensor was a few degrees below room temperature giving a usable warming interval between approximately -40 °C and +15 °C of about 20 hours.

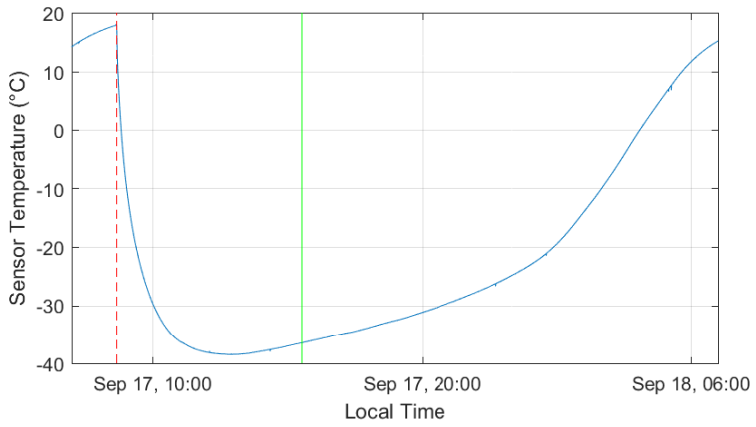

Figure 4-10: Temperature profile of sensor head. Dry ice is added to the experiment at 08:30 local time (red dashed line). Data was collected for analysis once the sensor temperature reached five degrees above the minimum temperature (green solid line). The experiment terminated at 07:55 local time the next day (right edge of graph).

The same STE magnetometer electronics were used in all the experiments. A five-meter analog cable was used to connect the sensors to the electronics box, rather than the transmission line transformer and ~80-meter cable often used in field deployment. This configuration was selected to minimise the effect of cable length and temperature, as 80 meters of cable would not fit in the foam box. The electronics were no longer driving a matched impedance; however, the short cable length minimised this impact.

The synchronisation output from the signal generator was driven into the pulse-per-second (PPS) timing input of the fluxgate electronics, which would normally be connected to a GPS time base. This synchronised and phase locked the 8 sps measurements from the fluxgate to the test signal, reducing frequency beating effects.

4.4.4 Observations and Data Analysis

Figure 4-11 (blue) shows a Welch's averaged periodogram showing the amplitude spectrum of the magnetic noise in the laboratory. Figure 4-11 (red) shows the same spectra with a 1 Hz test signal applied using the Helmholtz coil. The room is magnetically noisy; however, there are no coherent sources near 1 Hz, giving a signal to noise ratio of 68 dB in the 1 Hz frequency bin. The controlled

source at 1 Hz and careful spectral analysis should therefore allow relatively noise free measurement despite the general background noise of the laboratory. The large amplitude of the harmonics of the drive signal was not expected and remains unexplained.

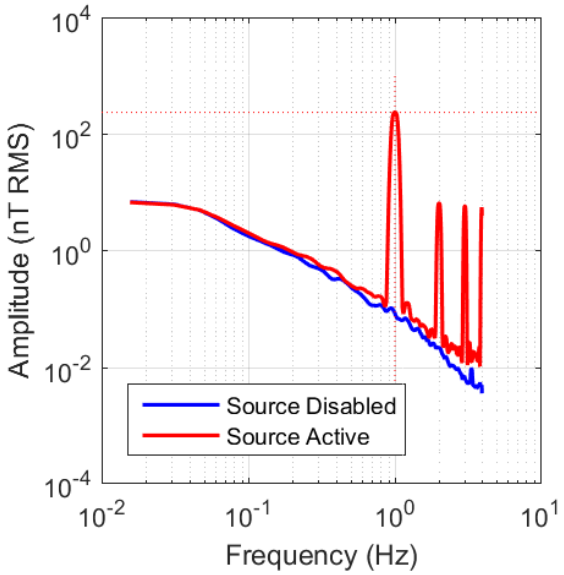

Figure 4-11: Amplitude spectra showing representative noise environment of the laboratory.(Blue) Equivalent spectra with a sinusoidal test signal applied using the Helmholtz coil. (Red)

The STE magnetometer generates 8 sps measurements of the magnetic field. This was analysed by subdividing into a series of non-overlapping blocks of 16384 samples (34 minutes). The choice of block length is a significant trade-off in the data analysis. Longer blocks sample more periods of the 1 Hz test signal, allowing a more precise estimation. However, a longer block length increases the chance that a transient noise event from the laboratory, with power at 1 Hz, will occur and contaminate the block. Increasing the number of points in the Fast Fourier Transform (FFT) decreases the likelihood that environmental noise sources will fall into the same spectral bin as the test signal, but decreases averaging for a fixed block size. The measured amplitude of the 1 Hz test signal for the block was calculated using Welch's method of overlapping periodograms (Matlab pwelch), a 512 bin FFT, an overlap of 50%, and an HFT248D flattop window function [*Heinzel et al.*, 2002]. The data shown in Figure 4-11 were obtained using these parameters. The apparent magnitude of the test signal was found to be robust over block lengths between 10 and 60 minutes and FFT lengths between 128 and 1024 points suggesting the selected FFT parameters are a reasonable compromise.

For each block of data, the sensitivity of the instrument was determined by the apparent amplitude of the test signal as measured by the FFT bin corresponding to 1 Hz in the averaged periodogram. The sensor and room temperatures were taken as the simple mean of the readings of the respective LM34 temperature sensors for the same period. Figure 4-12 illustrates the result for Trial 1 of the reference MACOR/MACOR sensor showing the measured amplitude of the applied magnetic test signal, the sensor temperature, and the room temperature. Note that the Y-axis scaling of the sensor and room temperature plots are different to allow the trend in each to be observed. The sensor temperature axis spans 60 °C while the room temperature axis spans 1°C.

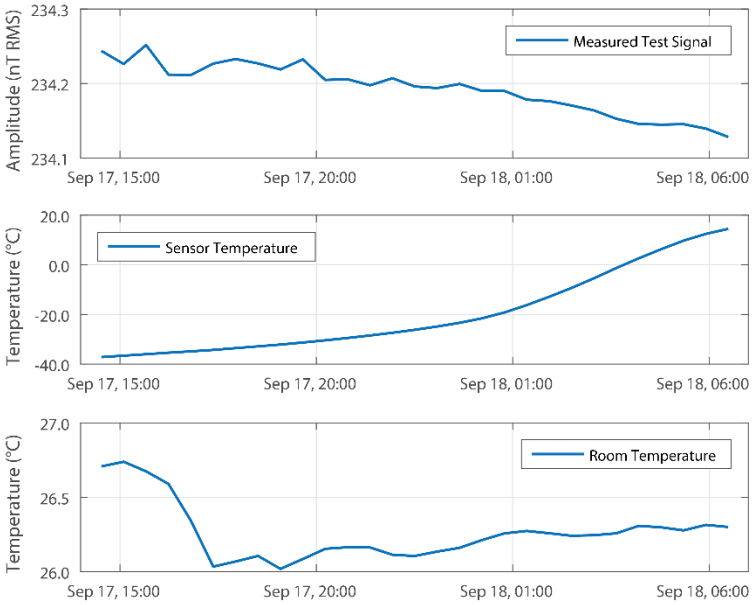

Figure 4-12: Trial one for MACOR/MACOR sensor. (top) Amplitude of applied sinusoidal test signal measured by the value of the 1 Hz bin the Welch's averaged periodogram. (middle) Temperature of warming fluxgate sensor. (bottom) Room temperature.

The sensor's change in sensitivity with temperature causes the measured amplitude of the test signal to vary as the sensor warms. The coefficient of thermal gain change was determined by plotting the measured test signal amplitude against sensor temperature and fitting a linear trend. Figure 4-13 shows such a plot for the MACOR/MACOR sensor. Robust linear regression (Matlab robustfit) was used for each trial to estimate a linear fit and minimize the impact of occasional outlying data. Robustfit iteratively reduces the weighting given to points away from the emerging linear trend line, allowing it to ignore the effect of outliers. This allows the linear temperature dependence to be estimated despite outlying points contaminated with local noise from the laboratory. Each sensor was tested three times to estimate the uncertainty of the measurement. The MACOR/MACOR sensor produced linear trends with similar slopes between the three trials (-8.2

± 0.5, -8.6 ± 0.3, -7.6 ± 0.5 ppm $°C^{-1}$). The visible Y offset between the trials are not well understood but may be related to drift in the function generator, changes in the geometry or alignment of the Helmholtz coil, or changes in the background magnetic noise of the laboratory. However, the measured slopes agree, within experimental error, across the three trials.

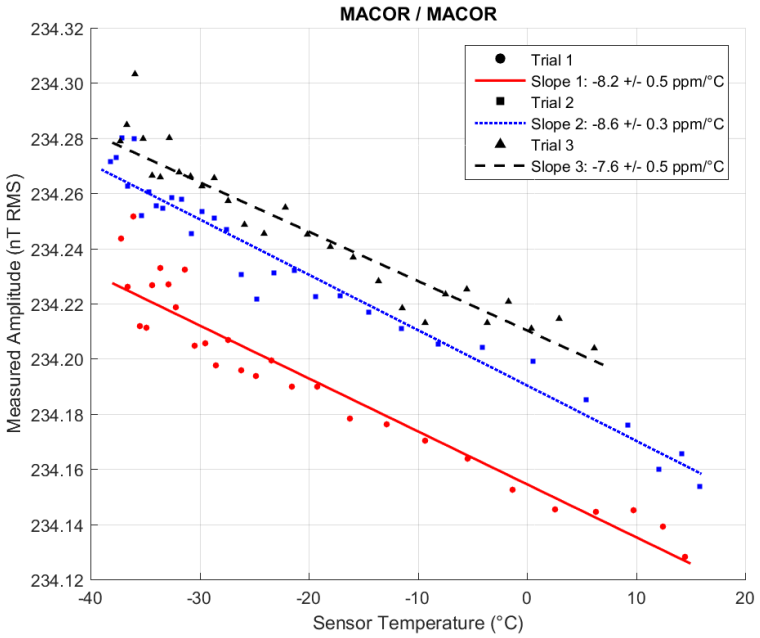

Figure 4-13: Results the MACOR/MACOR sensor trials 1 (red) 2 (blue) and 3 (black) for showing the measured amplitude of the test signal (scatter plot) and the linear trend (solid and dashed lines) determined by robust linear regression. The slope of each trial estimates the coefficient of thermal gain dependence for the sensor.

Figure 4-14 presents the equivalent scatter plot to Figure 4-13 but comparing the measured amplitude of the test signal to the room temperature when no dry ice was placed in the experiment. The scatter and shape of the room temperature data varied between trials as the building heating changed with the weather. In all cases, the room temperature was regulated to within two degrees and no consistent trends were observed in the room temperature. This suggests that there was minimal impact from the changes in room temperature on the amplitude of the magnetic test signal created by the signal generator and Helmholtz coil.

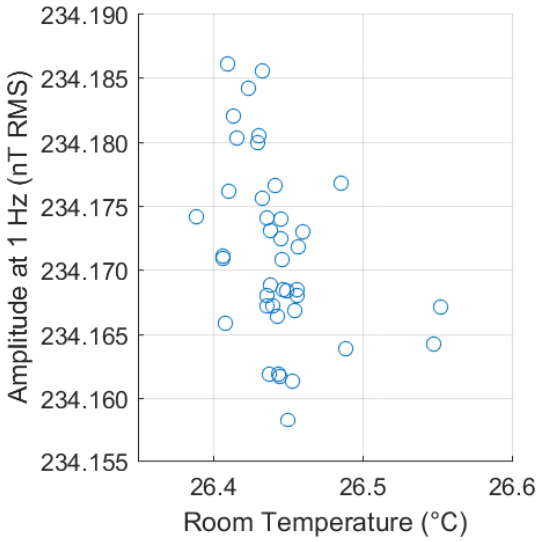

Figure 4-14: Measured signal amplitude plotted against room temperature. No consistent trends were observed between the different trials, suggesting that room temperature did not have a significant effect on the measured amplitude.

Part way through the experimental trials, it was discovered that the sinusoidal test signal could saturate the ADC. The test signal averages to zero at DC and therefore does not affect the instrument's decision to step the feedback offset in order to hold the instrument within range. The instrument can therefore clip when the environment's quasi-static field drifts before the instrument triggers a step in the offset voltage. Experimental trials that were clipped were discarded and repeated to obtain clean data. A smaller test signal would prevent this issue, albeit with a corresponding decrease in the signal-to-noise ratio of the measurement.

4.5 Results

Figure 4-15 compares the results of three trials using each of the six sensors. The Y-axes of the plots are offset to account for variation between sensors. However, the vertical span of the Y-axis is common to all plots. Therefore, the apparent slopes, which give α_g, can be meaningfully compared. The results for each sensor are reproducible between the three runs. Conversely, the results for the six sensors vary visibly in sign, magnitude, and apparent curvature.

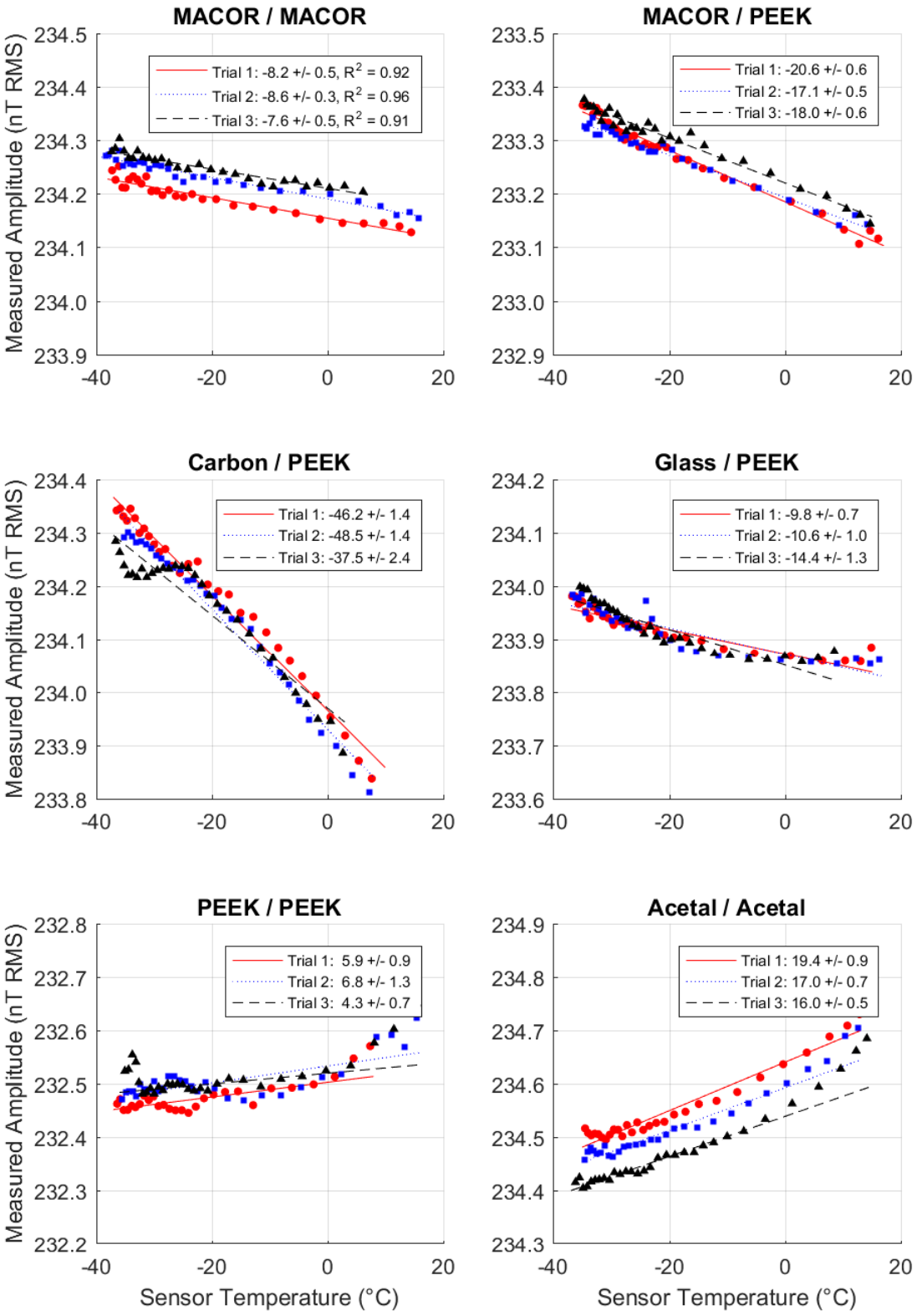

Figure 4-15: Measured amplitude of the constant 1 Hz test signal for three trials (red, blue, black) of all test sensors. Y-axes are offset to account for systematic variation between the instruments but have a common span so the slopes, which give the coefficient of thermal gain dependence, can be meaningfully compared between sensors. These data are raw measurements, and have not been post-process corrected for the temperature compensation built into the electronics unit.

The measured coefficient of thermal gain dependence, α_g, for the sensor in each trial was taken to be the slope, as determined by robust linear regression. The uncertainty in the slope was taken as plus or minus the standard error from the linear regression. The mean of the three slopes for each sensor was plotted against the coefficient of linear thermal dependence, α_m, of the material used in the bobbin, in order to compare the different sensors and materials (Figure 4-16).

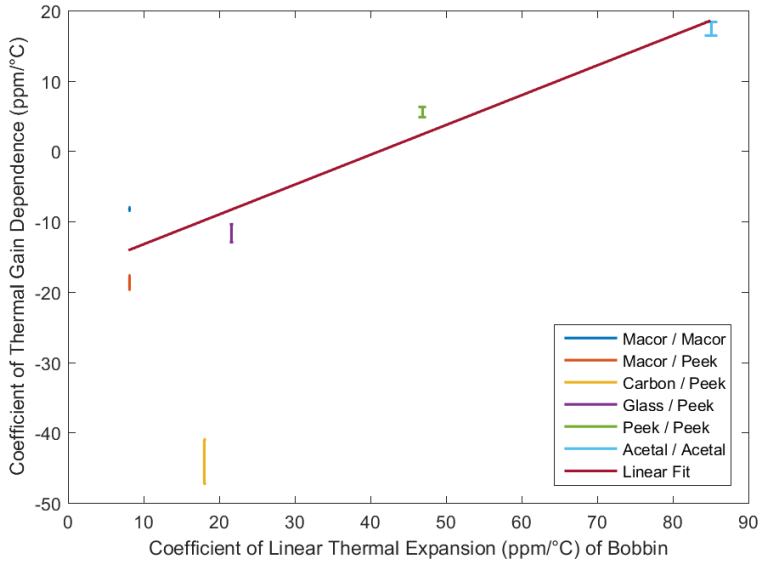

Figure 4-16: The measured coefficient of thermal gain dependence, α_g, for each sensor is approximately proportional to the manufacturer specified coefficient of linear thermal expansion of the bobbin material, α_m. Robust linear regression of the points gives a slope of 0.42 ± 0.09 and an offset of -17 ± 4 ppm °C^{-1}. The data for Carbon/PEEK is considered unreliable and was not included in the calculation of the trend line.

The Carbon/PEEK sensor had very different thermal stability than would have been expected from its specified coefficient of linear thermal expansion. As described in more detail in Appendix B, 30% carbon filled PEEK was found to be anomalously conductive, creating short-circuits within the sensor. Therefore, the results obtained for the 30% carbon filled PEEK sensor are shown for completeness, but the Carbon/PEEK sensor has been excluded from the calculation of the trend line on Figure 4-16.

The uncertainty for each point in Figure 4-16 was calculated as plus or minus one half of the difference between the minimum and maximum values of the three trials, including the uncertainty. Robust linear regression of these points gives a slope of 0.42 ± 0.09 ppm °C^{-1} and an offset of -17 ± 4 ppm °C^{-1}.

The fluxgate electronics provide linear temperature compensation, so non-linear temperature effects in the sensor cannot be compensated. Quantifying the non-linear temperature dependence

of the sensors is challenging due to the scatter in the data. A numerical estimate of curvature was calculated for each run, but gave high uncertainties that masked the apparent curvature visible by eye in some runs. As an alternative, the r^2 linear correlation coefficient was calculated, and is provided to estimate the quality of fit for the thermal trends. However, since robust linear regression uses iterative weighting to reduce the effect of outliers, it does not minimise r^2 as conventional linear fit does so the r^2 coefficients are expected to larger than would be expected from a linear fit despite the trend likely being a better fit to the data.

Table 4-3 summarises the results from this experiment giving: α_m provided by the manufacturer, which is taken to be equal to the theoretical α_g from (7); the measured α_g; and an estimate of the r^2 linear correlation coefficient. The measured α_g was calculated as the mean of the fit slope from the three trials, minus the zero intercept from Figure 4-16 (-17 ppm °C^{-1}) to remove the correction applied by the electronics. The discrepancy between the theoretical and measured values of α_g is discussed below.

Table 4-3: Parameters of materials used in this study. The measured coefficient of thermal gain dependence for each sensor has been corrected by -17 ppm °C^{-1} to remove the measured correction applied by the electronics. The sensor name corresponds to the material in the sensor bobbin and base respectively.

Sensor Name	**Manufacturer's Coefficient of Linear Thermal Expansion of bobbin material / Theoretical Coefficient of Thermal Gain Dependence (ppm / °C)**	**Measured Coefficient of Thermal Gain Dependence (ppm / °C)**	**Coefficient of Determination r^2**
MACOR/MACOR	8.1	9.3 ± 4	0.927
MACOR/PEEK	8.1	-1.1 ± 5	0.979
Carbon/PEEK	18.0	-27 ± 7	0.955
Glass/PEEK	21.6	5.9 ± 5	0.827
PEEK/PEEK	46.8	23.1 ±4	0.598
ACETAL/ACETAL	85.0	35.0 ± 5	0.950

4.6 Discussion

The measured coefficient of thermal gain dependency of the sensors was generally proportional to the coefficients of linear thermal expansion of the materials used to construct the sensor's bobbins. The zero offset of -17 ± 4 ppm °C^{-1} in Figure 4-16 implies a systematic temperature effect across all sensors that matches the 19.1 ppm °C-1 of compensation expected from the modified

transconductance amplifier within experimental error. Accounting for this compensation, the trend line would intersect zero/zero, implying that a sensor constructed from material with no deformation due to temperature would have no thermal gain sensitivity. Despite the observed difference between the MACOR/MACOR and the MACOR/PEEK sensor, this supports the assumption that the bobbin material has the dominant effect on the α_g of a sensor.

The slope of the trend line in Figure 4-16 indicates that the coefficient of thermal gain dependence is approximately one half the coefficient of linear thermal expansion of the bobbin material, rather than being equal to it as suggested by Acuña et al. [1978]. This discrepancy seems reasonable given the simplicity of the theoretical derivation, the lack of a ferromagnetic core in the derivation, potential mechanical effects from the Inconel foil bobbin, and the succession of approximations. It would be interesting to attempt a physics driven model of the magnetic field within the sensor to see if a more sophisticated treatment would better reproduce the measured relationship between the coefficient of linear thermal expansion of the material and the thermal gain dependence of the sensor. Such a model could also explore the relationship for other sensor geometries, such as the long circular solenoidal coils often wound on a tubular shaft containing racetrack shaped cores. Notably, the theoretical α_g calculated using the method of Acuña et al. [1978] agrees with the measured value of the MACOR/MACOR sensor (matching the material used in the Acuña instrument), but diverges as the α_m of the bobbins increase.

The significant difference between the measured α_g for the MACOR/MACOR sensor and the MACOR/PEEK sensor is in some way surprising. A possible explanation might be the sensor base deforming under test as the sensor base changes temperature, thereby rotating the sense axis of the bobbin with respect to the test signal. Such an effect may be due, in part, to the mismatch in α_m between the material used to construct the bobbin and the base. Unfortunately, the presence of this effect cannot be tested using the current dataset. A future experiment could repeat these tests using a three component Helmholtz arrangement. Simultaneously applying test signals at three different frequencies to the three axes could test for bobbin tilt by checking for an increase in the apparent amplitude of the test signals applied orthogonally to the nominal sense axis of the bobbin. Nevertheless, the discrepancy between the MACOR/MACOR and MACOR/PEEK sensors highlights the importance of maintaining the orthogonality of the three axes.

It is challenging to compare or interpret the linearity of the thermal dependence of the different sensors. An estimate of the r^2 coefficient of determination was calculated. However, it likely underestimates the quality of the fit and, does not discriminate between scatter and nonlinear effects. By eye, it would appear that the Glass/PEEK sensor is less linear than the reference MACOR/MACOR sensor; however, the numerical uncertainties are so large that no difference can be firmly established between the linearity of the thermal dependence of the different sensors.

The measured α_g of the 30% glass filled PEEK bobbin was within 5 ppm °C^{-1} of that of the MACOR bobbins. A sensor constructed from both 30% glass filled PEEK bobbins and a 30% glass filled base would likely have a slightly different thermal dependence (c.f., MACOR/MACOR and MACOR/PEEK). If a modest increase in thermal dependence can be tolerated or compensated, then 30% glass filled PEEK is a good candidate for future fluxgate sensors as it is more economical, easier to machine, lighter, and more robust than MACOR.

4.7 Conclusions

1. The coefficient of thermal gain dependence varied roughly linearly with the coefficient of linear thermal expansion of the material used to support the sense and feedback windings in the STE magnetometer. However, the coefficient of thermal gain dependence varied as approximately one half of the coefficient of linear thermal expansion of the bobbin rather than being equal as suggested by Acuña et al. [1978].
2. The small manufacturer specified coefficient of linear thermal expansion for 30% carbon filled PEEK made it appear to be an attractive material. However, carbon filled peek was found to be highly conductive, and created short circuits which made the sensor unusable.
3. 30% glass filled PEEK is, on paper, modestly more sensitive to temperature than MACOR, but its robustness, cost, and ease of machining make it an attractive material for manufacturing the bobbin supporting the sensor and/or feedback windings of the fluxgate and for the base of the senor. A 30% glass filled peek bobbin yielded a sensor with a measured thermal coefficient of 5.9 ± 5 ppm °C^{-1} versus 9.3 ± 4 ppm °C^{-1} for MACOR after removing the effect of electronic temperature compensation.

4. Highly precise (<0.1 nT) calibration measurements have been achieved in a magnetically noisy laboratory using a simple and inexpensive experimental setup comprising a constant sinusoidal magnetic test signal and temperature cycling via dry ice, and quantitative spectral analysis.

4.8 Author Contributions

D. M. Miles led the experiment, designed and built the experimental apparatus, executed the experiment, analysed the data, and prepared the manuscript with contributions from all authors. I. R. Mann provided supervision and funding and assisted in the interpretation of the data. A. Kale helped execute this and earlier versions of the experiment and developed the software tools to automate the data acquisition. B. B. Narod designed the STE magnetometer, helped construct the experimental sensors, and provided the acetal/acetal sensor. J. R. Bennest assembled the experimental sensors. D. Barona created the computer-aided design models used to manufacture the experimental sensors, and helped interpret the data. D. K. Milling oversaw the execution of the experiment and guided the data analysis and interpretation. M. J. Unsworth provided supervision, instrumentation, and assisted in the interpretation of the data.

4.9 Acknowledgements

Work on the project was supported by the Canadian Space Agency under grant 13SUGONGEN. D. M. Miles is supported by an NSERC PGSD graduate scholarship and by funding from the Canadian Space Agency. I. R. Mann is supported by a Discovery Grant from Canadian NSERC. The authors wish to thank A. Vinagreiro and P. Zimmerman for machining the components in the experimental sensors and C. Z. Miles for helping construct the thermal test chamber.

Chapter 5: Alfvénic Dynamics and Structuring of Discrete Auroral Arcs: Swarm and e-POP Observations[5]

5.1 Abstract

The electrodynamics associated with dual discrete arc aurora with anti-parallel flow along the arcs were observed nearly simultaneously by the enhanced Polar Outflow Probe (e-POP) and the adjacent Swarm A and C spacecraft. Auroral imaging from e-POP reveal 1-10 km structuring of the arcs, which move and evolve on second timescales and confound traditional single and dual spacecraft field-aligned current algorithms. High-cadence magnetic data from e-POP shows 1-10 Hz, presumed Alfvénic, perturbations co-incident with, and at the same scale size as, the observed dynamic auroral structures. Analysis of high-cadence E- and B- field data from the adjacent Swarm A spacecraft reveals non-stationary electrodynamics involving reflected and interfering Alfvén waves and signatures of modulation consistent with trapping in the Ionospheric Alfvén Resonator (IAR). Taken together, these observations suggest a role for Alfvén waves, perhaps also the IAR, in discrete arc dynamics on 0.2 - 10s timescales and ~1-10 km spatial scales.

5.2 Introduction

A number of auroral acceleration mechanisms have been proposed and described in the literature which can be broadly divided [see e.g., review by *Mottez*, 2015] into acceleration by quasi-static electrical potential [e.g., *Evans*, 1974] and acceleration by interaction with Alfvén waves [e.g., *Lysak*, 1990]. Discrete auroral arcs are traditionally thought to be related to keV electrons accelerated by quasi-static electric fields [see e.g., review by *Swift*, 1981]. However, Alfvénic acceleration is increasingly proposed particularly in relation to small scale and dynamic aurora [*Stasiewicz et al.*, 2000] and multi-arc aurora observed from the ground [*Trondsen et al.*, 1997]. More broadly, authors such as Wygant et al. [2000] and Keiling et al. [2003] have shown that there is sufficient power in Earthward Alfvén wave Poynting flux (at ~6 Re altitudes) to power the aurora.

In the frame of a spacecraft travelling in low-Earth orbit satellite, it can be difficult to distinguish the magnetic and electric perturbations caused by genuine temporally evolving wave processes from those caused by the spatial structure. For example, small-scale filamented static field-aligned

[5] This chapter is based on [*Miles et al.*, 2017a] with contributions as described in the preface for this thesis.

currents (FAC) can appear as temporal variations in the frame of the spacecraft because of the spacecraft's motion. This makes studies of the relative importance of different acceleration mechanisms, of currents at different scale sizes, and of the role of Alfvén waves more challenging. However, the recently launched European Space Agency Swarm constellation of three spacecraft [*Friis-Christensen et al.*, 2008] has proven to be a powerful tool to study scale and dynamics of magnetospheric processes [*Goodwin et al.*, 2015; *Spicher et al.*, 2015; *Miles et al.*, 2016; *Forsyth et al.*, 2017]. Here we exploit the multi-spacecraft nature of the Swarm mission to investigate the dynamics and processes associated with structured discrete auroral arcs.

A robust and routine quantitative characterization of the magnetosphere-ionosphere coupling (MIC) processes controlling the aurora would require a dense constellation of spacecraft carrying plasma-physics instrumentation, complemented by high-cadence, co-located auroral imaging. No-such mission currently exists; however, here we present a case study where during one pass a nominal version of such a constellation was created temporarily using conjunctions between existing spacecraft. This was done by scheduling observations from the Canadian Space Agency's enhanced Polar Outflow Probe (e-POP) [*Yau and James*, 2015] to coincide with a near magnetically conjugate crossing by the Swarm A and C spacecraft. The three spacecraft crossed a region characterized by highly structured and rapidly evolving discrete aurora providing a unique opportunity for a multi-spacecraft electrodynamic study of the evolution of discrete arc substructure which was being characterized at the same time by a space-borne imager. In particular, combing the high cadence electric and magnetic field measurements from Swarm provides the basis for identifying periods of Alfvénic activity associated with the discrete arc dynamics.

5.3 Data and Instrumentation

We present a case study of a period characterized by dynamic discrete aurora sampled by both e-POP and the Swarm A and C spacecraft on March 11, 2016 between 06:47 and 06:50 UTC over northern Canada. This is one of approximately forty auroral region conjunctions between e-POP and the Swarm A and C spacecraft in early 2016. This event was selected for the interesting auroral dynamics observed during the early phase of a modest substorm with onset around 06:30 UTC. The e-POP spacecraft was eclipsed by the Earth and was travelling poleward at about 750 km altitude. The e-POP Fast Auroral Imager (FAI) [*Cogger et al.*, 2014] captured images at 1 second

cadence and the Magnetic Field Experiment (MGF) [*Wallis et al.*, 2015] measured the local magnetic field at 160 sps. The MGF magnetic data is down-sampled to 20 sps for this study to avoid magnetic contamination arising from the reaction wheels on the e-POP spacecraft. Swarm A and C were travelling equatorward at about 440 km altitude and crossed the same geographic latitude about 120 seconds later and about two degrees east. Swarm A and C both recorded magnetic field data at 50 sps using the Vector Field Magnetometer (VFM) instrument [*Merayo et al.*, 2008]. Swarm A also captured 16 sps data from the Electric Field Instrument (EFI) instrument [*Knudsen et al.*, 2017]. No electric field data is available from Swarm C or e-POP because the respective EFI and Suprathermal Electron Imager (SEI) [*Knudsen et al.*, 2015] instruments were not operating. The aurora were obscured from terrestrial all-sky imagers by cloud during the interval. Figure 5-1a gives a mapped overview of the event showing the tracks of the three spacecraft, an FAI auroral image taken at 06:49:36 UTC, and the cross-track magnetic perturbations (as a proxy for inferring FACs) plotted as quivers on the spacecraft tracks (the magnetic perturbations are normalized on a common scale so the quivers can be compared). Throughout the manuscript, magnetic and electric perturbations were calculated by subtracting a twenty-second running mean to remove the background field. The latitude and longitude of all spacecraft data is traced magnetically to an assumed auroral emission height of 110 km using tools available from the International Radiation Belt Environment Modeling (IRBEM) library [*Boscher et al.*, 2010] implementing the Olson and Pfitzer [1977] magnetic field model.

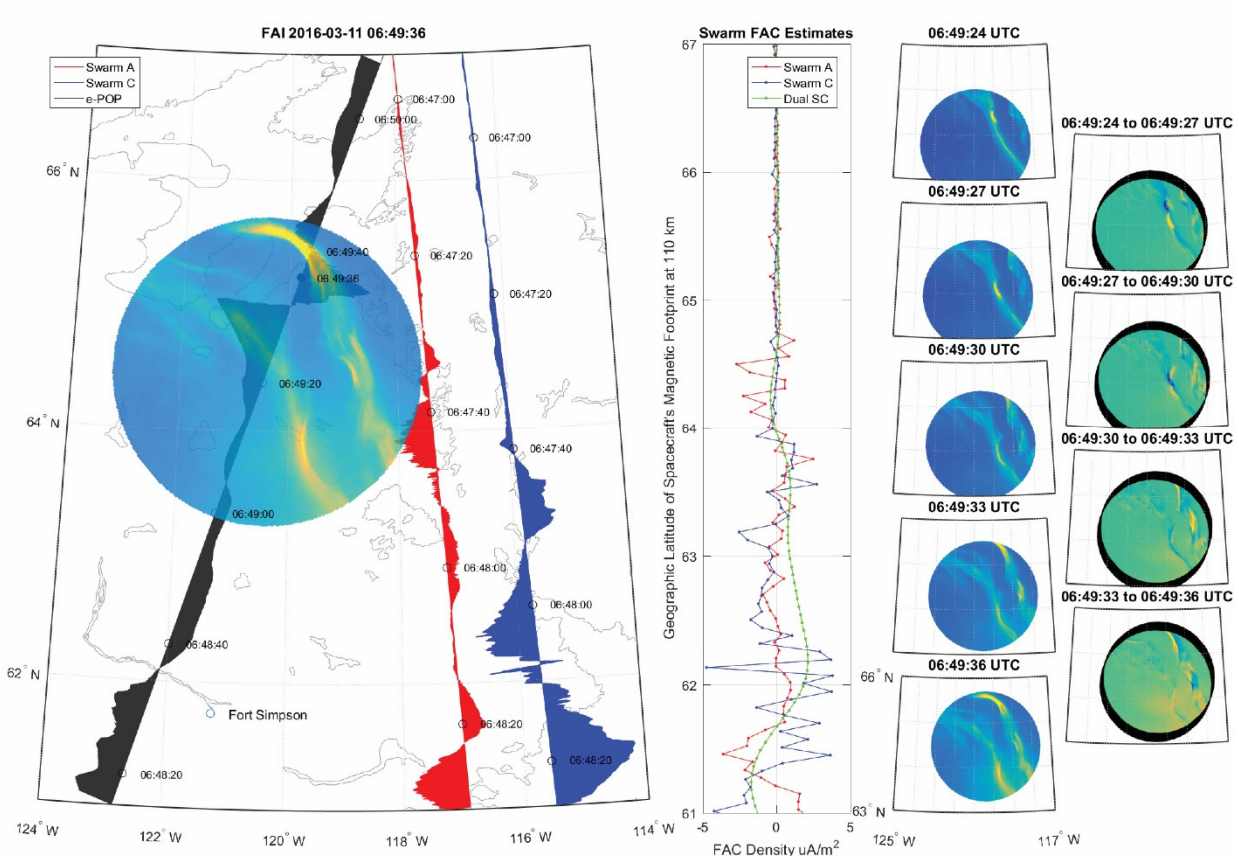

Figure 5-1: Near conjugate measurements on March 11, 2016 from e-POP (black) and Swarm A (red) and C (blue) spacecraft. (a) Spacecraft tracks overlaid on a coastline map to show geography, static FAI image from 06:49:36 UTC, with superposed cross-track magnetic perturbations with a common normalization. (b) FAC density as estimated by single spacecraft methods for Swarm A (red), Swarm C (blue) and by the Swarm dual spacecraft integral method (green); see text for details. (c) e-POP FAI images at 2 second intervals showing dynamic aurora. (d) Differenced FAI images showing along-arc motion of auroral emission travelling equatorward along the southern arc and poleward along the northern arc.

The challenges associated with disentangling the spatio-temporal characteristics of the MIC, which is active at this time, is immediately clear in Figure 5-1. The cross-track magnetic data from the Swarm A (red quiver) and C (blue quiver) spacecraft show remarkable differences in both amplitude and polarity as a function of latitude (Figure 5-1a). In the absence of either auroral context, or a combined analysis of the electric and magnetic fields, it is clear that it would be almost impossible to understand the nature of the MIC processes that are encountered. This illustrates some of both the challenges but also the scientific opportunities associated with using multiple spacecraft constellations for understanding MIC.

5.4 Results

5.4.1 Discrete Auroral Arc Dynamics

During this interval the e-POP spacecraft overflew two dynamic discrete auroral arcs – the equatorward arc at around 06:49:25 UTC and the poleward arc at around 06:49:40 UTC (Figure 5-1a). Immediately outside of the arc region, the cross-track magnetic field is relatively smooth. Co-incident with and between the two arcs the cross-track magnetic field has short-timescale perturbations. The e-POP spacecraft appears to have intersected the two arcs at an angle of approximately 45°; however, a single angle cannot be defined exactly as the portions of the two arcs visible in the FAI image are not perfectly straight.

The Swarm C spacecraft leads Swarm A by about 5 seconds along-track and the spacecraft were separated by ~1.5° cross-track with Swarm A being farther west and closer to e-POP. The Swarm spacecraft were outside the field of view of FAI on e-POP and crossed the region of interest 120 seconds before e-POP, so we cannot definitively determine at what angle they crossed auroral features that are assumed to extend east to intersect the Swarm satellite orbits. However, linearly extending the two arcs and assuming they did not move significantly in 120 seconds (this is likely an oversimplification given the visible arc dynamics) allows us to estimate that the Swarm A orbit likely intersected the arcs at a small angle some time around 06:47:40 to 06:47:50 UTC. For Swarm C, estimating the likely intercept is even more challenging. Swarm C is even farther from the FAI image and the trends in the cross-track magnetic field do not seem to match those of Swarm A in either amplitude or polarity despite the small azimuthal separation of their orbits and their very short along-track relative time lag.

The sequences of auroral images shown in Figure 5-1c are each separated by 3s and are mapped to an assumed emission height of 110 km. Figure 5-1c demonstrates clearly that the discrete auroral arcs had significant internal fine structure and were neither static nor stationary, even on second timescales. The FAI images show that the dual-arc system was ~80 km wide, both arcs were ~10 km wide, and smaller features were visible on scales of 1-10 km. Meshing the auroral images onto a common grid and differencing the 3s frames (Figure 5-1d) characterizes the darkening/brightening of these auroral features in blue/yellow. The differenced images show southeast flow of a localized bright region along the equatorward arc, with similar but opposing north-west flow of brighter features along the poleward arc.

5.4.2 Field-Aligned Current Estimates

The Swarm FAC algorithms for single spacecraft [*Lühr et al.*, 1994, 1996] and dual spacecraft [*Ritter and Lühr*, 2006; *Ritter et al.*, 2013] analyses require several simplifying assumptions to infer FAC from the magnetic field measurement. FAC phenomena are assumed stationary, static, and homogenous over the transit time, separation time, and physical separation of the spacecraft. The Swarm single spacecraft algorithm assumes the spacecraft crosses as long, straight current sheet. The Swarm dual spacecraft algorithm low-pass filters the data at ~20 s requiring the assumption that the currents are related to static or low frequency phenomena that would pass this filter. As Figure 5-1 indicates, none of these assumptions are met for the active, curved, structured, and dynamic auroral region crossed at small angles by the Swarm and e-POP spacecraft.

From the map (Figure 5-1a) we see that the discrete auroral arcs are not homogenous on the spacing of the spacecraft. Although the global structure comprises two parallel highly inclined discrete arcs, each arc displays very significant internal fine structure and dynamics. e-POP intersected the arcs at an angle of attack of ~45° and, by extrapolation, it appears that Swarm A and C crossed the arcs at small angles of attack. Each spacecraft crossed the projected location of the two discrete arcs at significantly different latitudes. Perhaps unsurprisingly, based on the arc dynamics revealed by the e-POP FAI, the single spacecraft FAC estimates for Swarm A, C, and that derived with the Swarm dual spacecraft technique (Figure 5-1b, red, blue, and green respectively) differ significantly not only in magnitude but also in polarity. For this interval and considering lagged correlations between the three estimates of up to ± 50 seconds the highest possible correlation between any two estimates is only 0.36. All FAC estimates shown in Figure 5-1b were mapped magnetically from each spacecraft's location to 110 km to match the assumed emission height in the auroral images. The magnetic conjunction of e-POP and Swarm A and C provides an opportunity to examine why the three magnetic Swarm FAC estimates for the period have poor internal consistency. Similarly, it can be used to investigate why the inferred FAC spatial structure from e-POP magnetic data was not consistent with the auroral features observed by the FAI.

As we discuss further below, the observations indicate the importance of Alfvén waves for MIC during this time. Such Alfvén waves would create a dB/dt signal that the single spacecraft FAC algorithm would misinterpret along track as small-scale static currents. The dual spacecraft algorithm includes a ~20s filter which removes smaller scale signals. However, not only does this have the effect of throwing away information, if the magnetic perturbations and FAC at these

scales dominate the related MIC then such filtering means that the algorithm cannot be used to characterize the MIC. During this case-study, both the single and dual spacecraft Swarm FAC algorithms fail because the Alfvénic nature of the MIC violates the quasi-stationarity assumptions required for the Lühr et al. [1996] and Ritter et al. [2013] algorithms to be valid.

5.4.3 Magnetic Dynamics Conjugate to the Auroral Arcs

The e-POP magnetic measurements show short time scale perturbations, inferred below to be Alfvénic, superposed on a longer time scale deflection typically assumed to be quasi-static and at large spatial scales characteristic of the Iijima and Potemra [1976] global FAC system (Figure 5-2a). Band-pass filtering the e-POP magnetic data from 0.2 to 4.0 Hz and comparing it to the auroral intensity seen by the FAI magnetically conjugate to the spacecraft shows that ±10-15 nT peak-to-peak perturbations occurred coincident with but also between the two discrete auroral arcs (Figure 5-2b). The auroral intensity recorded by FAI magnetically conjugate to e-POP clearly resolves the two arcs, the dark space between them, and the brightening background as the spacecraft exits eclipse around 06:49:50 UTC. Perturbations of similar frequencies and amplitude in the 0.2 to 4.0 Hz band were observed in the Swarm A and C magnetic data, and in electric field data available only for Swarm A (Figure 5-3).

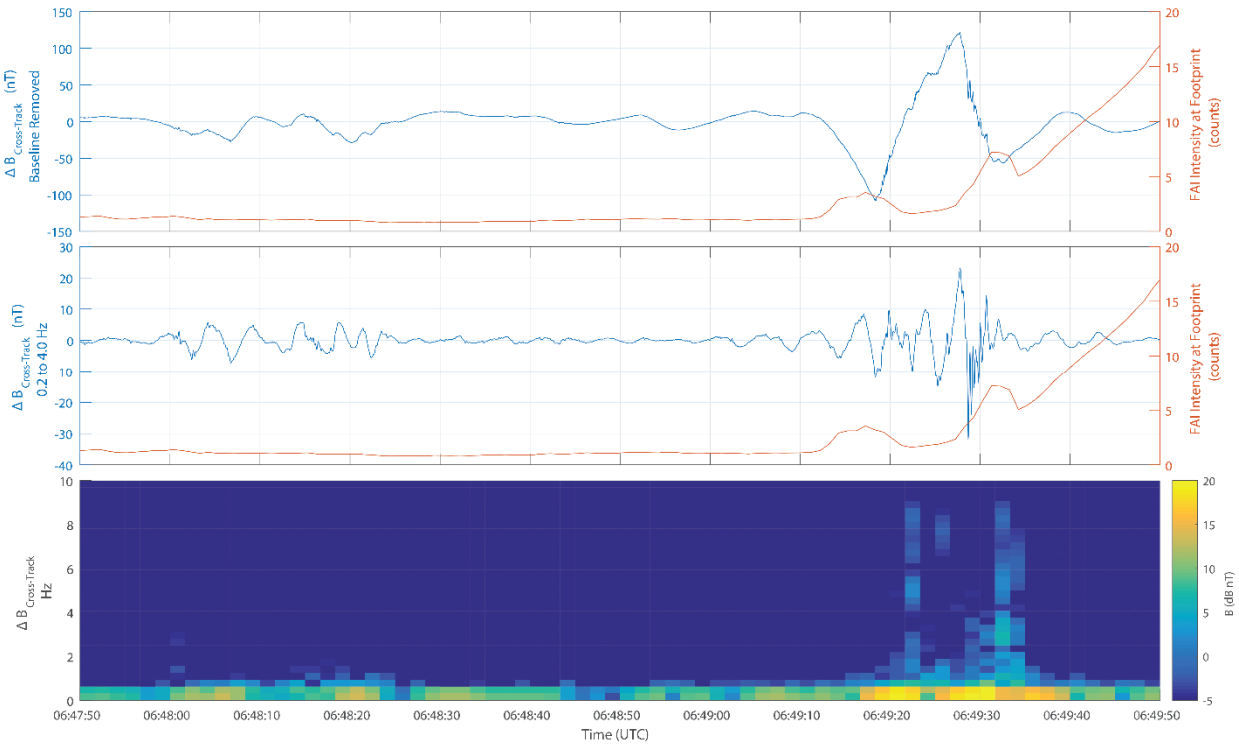

Figure 5-2: e-POP measurements showing: (a) Cross-track magnetic perturbations and the auroral intensity magnetically conjugate to e-POP. (b) Same data as (a), but with the magnetic data band pass filtered from 0.2 to 4.0 Hz. (c) Amplitude spectrum of the cross-track magnetic perturbations.

Figure 5-2c shows an amplitude spectrum of the un-filtered magnetic perturbations. Broadband enhancement from ~ 1 Hz up to the 10 Hz Nyquist frequency is apparent throughout the auroral crossing. Notably, there are no narrow-band spectral features. The spacecraft is travelling at ~7.7 km/s so waves in the 1 to 10 Hz range would correspond to a spatial scale of about 7.7 to 0.77 km, respectively, if they correspond to spatial structures. This would match the ~1-10 km scale size of the fine structure seen within the two discrete arcs in the auroral images. Magnetic perturbations are also observed earlier in the orbit, further equatorward than the two discrete arcs, between 06:48:00 and 06:48:30 UTC. The magnetic perturbations in the band pass filtered data are around half as large in magnitude as those measured in magnetic conjunction with the arcs (only ±5 nT peak-to-peak), but there is no auroral enhancement observed in the FAI intensity at the footprint of e-POP at these lower latitudes.

5.4.4 Alfvén Waves Electrodynamics

Swarm A and C both detected magnetic perturbations comparable in amplitude to those observed by e-POP as they crossed the extrapolated location of the dynamic discrete auroral arcs. Swarm A was operating its EFI instrument at this time at 16 sps and hence also resolved the perturbations in

the electric field associated with the discrete arc dynamics and related MIC. Note that the Swarm spacecraft were travelling equatorward while e-POP was travelling poleward so the observed measurement sequences are reversed. Figure 5-3 illustrates the characteristics of the time series and spectra of the Swarm A electric and magnetic field measurements. We define two regions, discussed below, to test for the presence of Alfvén waves. The solid vertical lines define a quiet twenty-second-long interval from 06:47:05 to 06:47:25 UTC and the dashed vertical lines define an equivalent twenty-second-long interval conjugate to the assumed region of the poleward dynamic discrete auroral arc from 06:47:35 to 06:47:55 UTC.

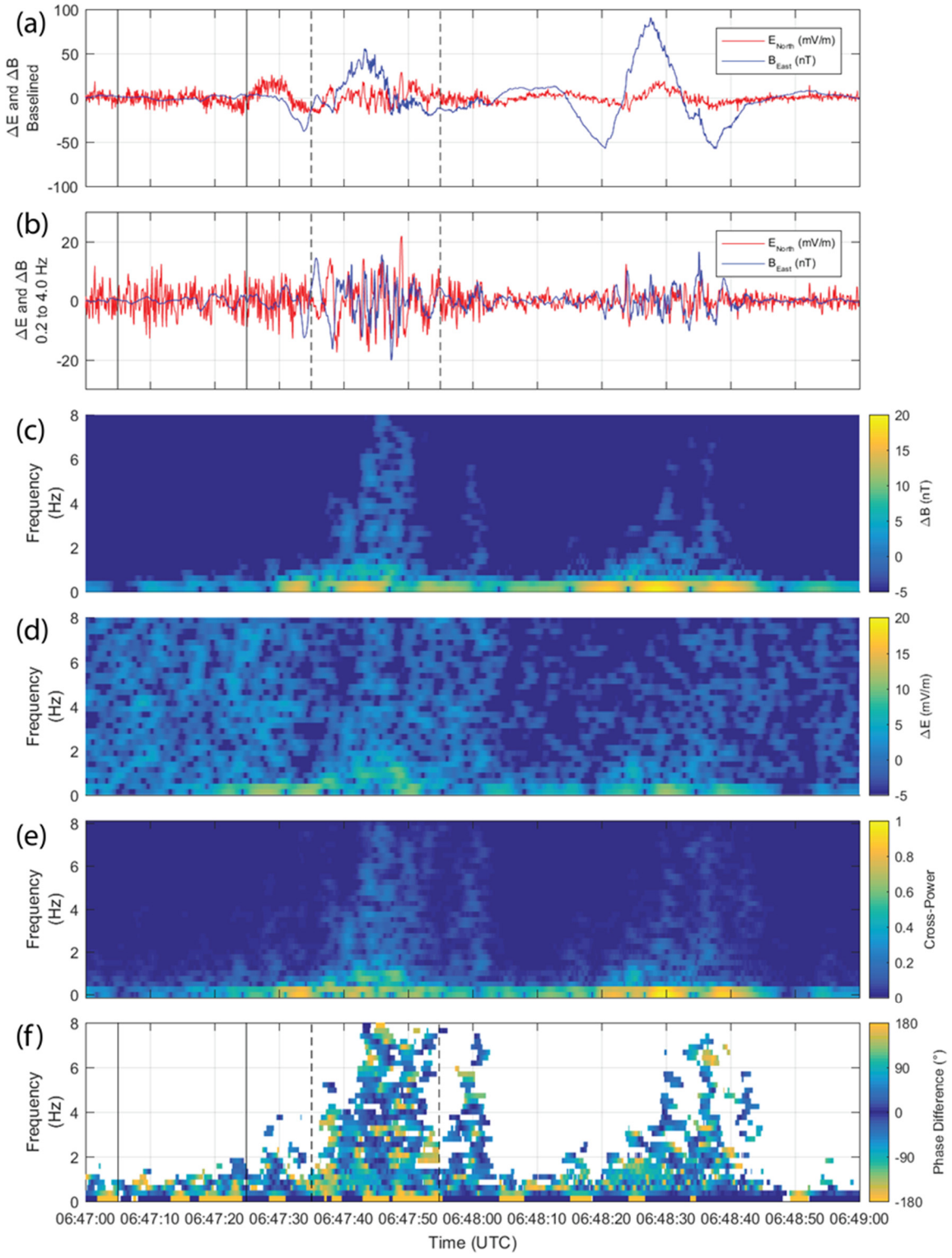

Figure 5-3: Electric and magnetic field measurements from Swarm A in Geographic coordinates. (a) North electric component and east magnetic component with background field removed. (b) Same but band-pass filtered from 0.2 to 4.0 Hz. (c) Amplitude spectrum of the northward component of the magnetic field. (d) Amplitude spectrum of the eastward component of the electric field. (e) Cross-power spectrum of the electric and magnetic fields shown in panels (c) and (d). (f) Phase difference between the electric and magnetic field showing only regions where the cross-power exceeds 0.3 nT/√Hz. The solid and dashed lines define the quiet and active auroral intervals, respectively (see text for details).

Figure 5-3a shows the north electric component and east magnetic component (geographic coordinates) measured by Swarm A with the background fields removed by subtracting a twenty second running mean. Figure 5-3b shows the same interval but band pass filtered from 0.2 to 4.0 Hz. In the more poleward active region, from 06:47:35 to 06:47:55 UTC, Swarm A detected perturbations superposed on a static offset similar to that observed by e-POP when it was conjugate to the active discrete auroral arcs. For Swarm, this occurred eastward and outside the field of view of the e-POP FAI, and separated in time by ~120 seconds, but the location of the large amplitude fluctuations along the orbit generally agrees with where the extrapolated auroral arcs would be expected to be located. Interestingly, Swarm A also detects a second set of perturbations equatorward of the active aurora, comparable to that observed by e-POP. As in the e-POP data, the band-pass magnetic amplitude is about half as large (±10 nT) in this lower latitude region as seen in association with the active aurora, but the Swarm A data also show an additional larger scale magnetic deflection not observed by e-POP.

Figure 5-3c shows a magnetic amplitude spectrum showing a broad spectral enhancement from ~1 Hz up to the Nyquist frequency, similar to that observed by e-POP. Figure 5-3d shows a similar broadband enhancement in the eastward component of the Swarm electric field data, albeit with a much noisier background. Figure 5-3e shows a cross-power spectrum for these two electric and magnetic field components reproducing the same broad-spectrum enhancement coincident with the inferred location of the discrete auroral arc crossings. Figure 5-3f further estimates the phase difference between the electric and magnetic field data from Figures 3c and 3d as a function of frequency. To separate the enhanced power from the noise electric background, the phase difference is shown only when the associated cross-power exceeds a threshold of 0.3 nT/√Hz. The phase difference spectrum appears rather noisy but clusters around -45° in the regions of broadband power enhancements from ~1 Hz to the Nyquist frequency. As we describe below, this appears to be consistent with a mixture of incident and ionospherically reflected Alfvén waves.

All three spacecraft detect similar magnetic perturbations when they are assumed magnetically conjugate to the dynamic discrete auroral arcs. These perturbations could be interpreted either as the magnetic signatures of small-scale static FAC which are crossed by the spacecraft, or as the signature of Alfvén waves. We applied the technique of Knudsen et al. [1990, 1992] to the Swarm A electric and magnetic field data to quantitatively test for the presence of Alfvén waves. Knudsen et al. argue that for static currents the ratio of the electric to magnetic field is controlled by the

height integrated Pedersen conductivity of the ionosphere, Σ_P, with the phase difference between these fields being close to zero. In contrast, for ionospherically reflected and interfering Alfvén waves the ratio will alternate between $1/\Sigma_P$ and $\mu_o V_A \Sigma_P$ as a function of frequency, with the phase difference between the E- and B-fields similarly changing as a function of frequency, because of the wave interference. For a single travelling Alfvén wave the E/B ratio will be given by the Alfvén speed, V_A.

Unfortunately, we do not have a direct way of measuring the height integrated Pedersen conductivity. The ranges available from models and the literature vary significantly from 0.25 S in the International Reference Ionosphere model [*Bilitza et al.*, 2014], through ~2.5 S [*Sheng et al.*, 2014], to ~10 S [*Hardy et al.*, 1987; *Gjerloev and Hoffman*, 2000] depending on latitude, and geomagnetic conditions. Here we assume Σ_P = 2.5 S. Figure 5-4 compares the ratio of the electric and magnetic perturbations from the quiet interval (Figure 5-3, solid vertical lines; Figure 5-4 left column) to the more active discrete auroral arc region (Figure 5-3, dashed vertical lines; Figure 5-4 middle and right columns). For the active region we examine both the ratio of E_{North}/B_{East} (middle column) and E_{East}/B_{North} (right column) which might correspond to Alfvén waves with different polarizations [*Grzesiak*, 2000].

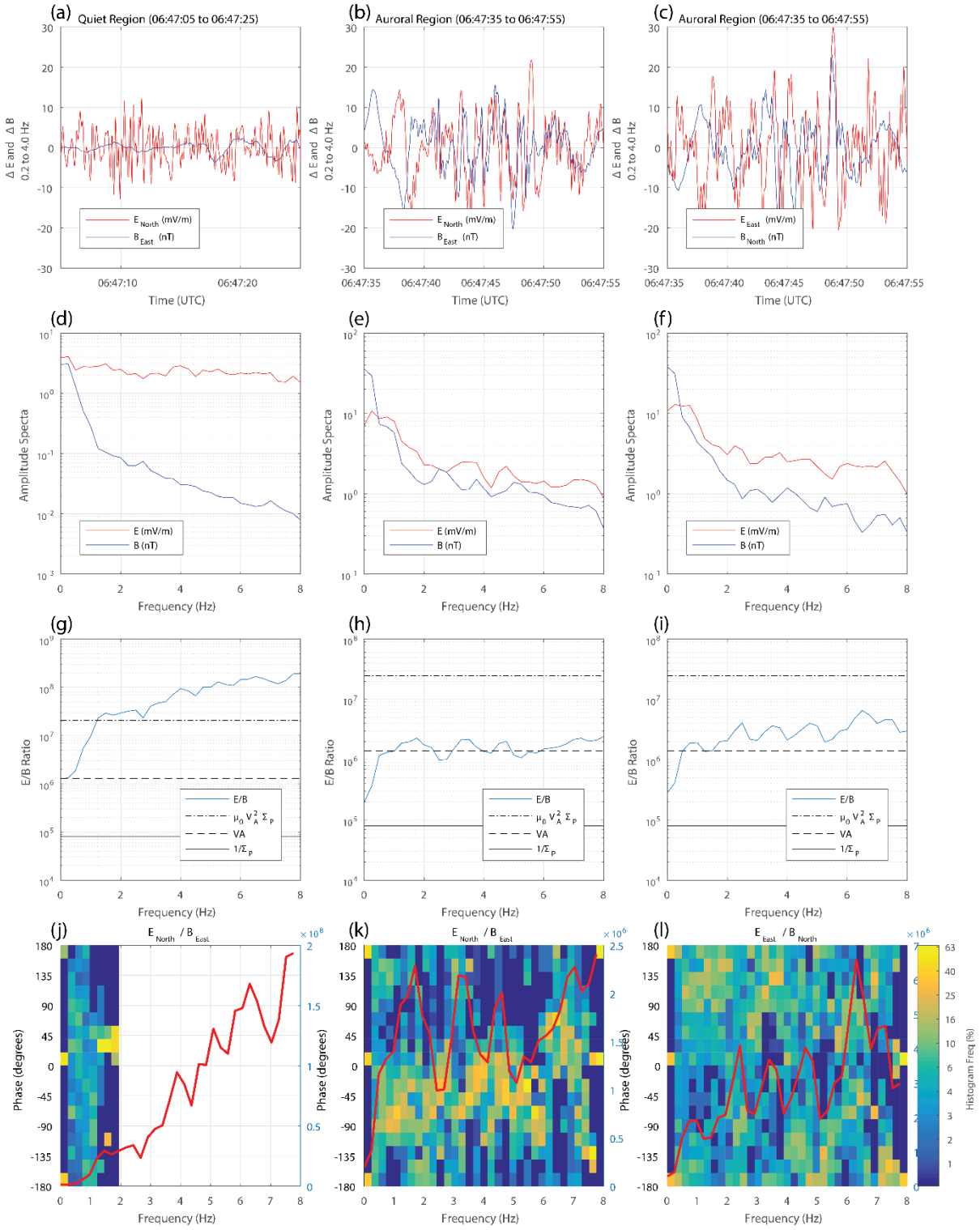

Figure 5-4: Analysis of electric and magnetic data from Swarm A (a, b, c). Band-pass filtered magnetic and electric perturbations. (d, e, f). Same data as (a, b, c) shown as an amplitude spectrum calculated by Welch's method of overlapped periodograms. (g, h, i) Ratio of electric field divided by magnetic field (E/B) with the dotted line showing the estimated local Alfvén Speed. (j, k, l) Histogram of the phase difference between the magnetic and electric field. Red shows the E/B ratio at an arbitrary linear scale. The left column covers twenty seconds in the pre-auroral quiet region. The middle and left column cover twenty seconds in the active auroral region considering the E_{North}/B_{East} and E_{East}/B_{North} Geographic components, respectively.

The band-pass filtered data (Figure 5-4, panels a, b, c) clearly show that the electric field data contains significant noise in the relevant frequency band, with much lower signal to noise than the magnetic field. Nonetheless, the electric field perturbations overcome the noise floor in the region of the active discrete auroral arcs (Figure 5-4, panels b, c) and similar signals are observed in both the electric and magnetic data. It is clear in Figure 4 (panels b and c) that there is a closer relationship between the northward E (E_{North}) and eastward B (B_{East}) waveforms (panel b), than between the eastward E (E_{East}) and northward B (B_{North}) (panel c). In both polarizations there appears to be a superposition of multiple frequency components suggesting that frequency domain analysis is needed to examine the electromagnetic characteristics of the arc-related perturbations at the altitude of Swarm A. Nonetheless, these magnetic and electric fields appear to be almost certainly associated with the dynamics of the fine structure in the discrete auroral arcs seen by the e-POP FAI.

Figure 5-4 (panels d, e, f) show amplitude spectra for both regions computed used the method of averaged overlapped periodograms [*Welch*, 1967]. The electric field spectrum is dominated by white noise in the quiet interval with the amplitude being approximately constant with frequency. However, it shows the same spectral shape as the magnetic data within the active discrete auroral arc region (middle and right columns in Figure 4) confirming that the perturbations are large enough to be detected in both the electric and magnetic data.

Figure 5-4 (panels g, h, i) show the electric to magnetic field ratio as a function of frequency, calculated by dividing the amplitude spectra of the electric and magnetic fields from Figure 5-4 (panels d, e, f). In the quiet region, the noise in the electric field data dominates and the ratio does not appear to converge to a physically meaningful value. However, in the regions of the active discrete auroral arcs the ratio trends to an almost constant value of $\sim 1.5 \times 10^6$ for frequencies above ~1 Hz.

In order to compare the E/B ratio spectra with the theoretical estimates of the spectra generated by interfering Alfvén waves, we estimate the local Alfvén speed using the average ion density, n_i, measured by the Langmuir probe and which was $3.94 \times 10^4 \text{cm}^{-1}$ for the quiet zone and $3.40 \times 10^4 \text{cm}^{-1}$ for the active auroral region. Assuming that the local plasma is dominated by Oxygen ions [e.g., *Johnson*, 1969] we calculate the Alfvén speed, V_A, as

$$V_A = \frac{B}{(\mu_0 \rho)^{\frac{1}{2}}} = \frac{B}{(\mu_0 n_i 16u)^{\frac{1}{2}}}$$

where B is the local scalar magnetic field, ρ is the local mass density, μ_0 is the magnetic permeability of free space, and u is the unified atomic mass unit. This gives local Alfvén speeds of 1.30×10^6 m/s for the quiet region and 1.40×10^6 m/s in the active auroral region.

Figure 5-4 j, k, l show how the measured electric to magnetic field ratio (E/B) fluctuates around the derived Alfvén speed (shown as horizontal dashed lines) in the active auroral region. This is consistent with what Knudsen et al. [1990] predict for Alfvénic signal and suggests that the perturbations observed by e-POP and Swarm co-incident with the active discrete auroral arcs were associated with Alfvén waves.

5.4.5 Signatures of the Ionospheric Alfvén Resonator?

The Alfvén waves sensed by Swarm A could exist in three likely configurations. They could be exclusively downwards travelling and fully absorbed by the ionosphere. They could be partially or fully reflected by the ionosphere creating a mixture of upward and downward travelling waves. Finally, they could become (probably partially) trapped in the Ionospheric Alfvén Resonator (IAR) [*Belyaev et al.*, 1990; *Lysak*, 1991] cavity formed between the E or F layer of the ionosphere at the bottom and a peak in the Alfvén speed at the top. The comb-like spectral feature indicative of the IAR in ground-based induction coil magnetometer dynamic spectra was observed between ~02:00 and ~08:00 UTC in induction coil data from the Ministik Lake and Pinawa stations (Figure 5-5) of the CARISMA ground magnetometer array [*Mann et al.*, 2008].

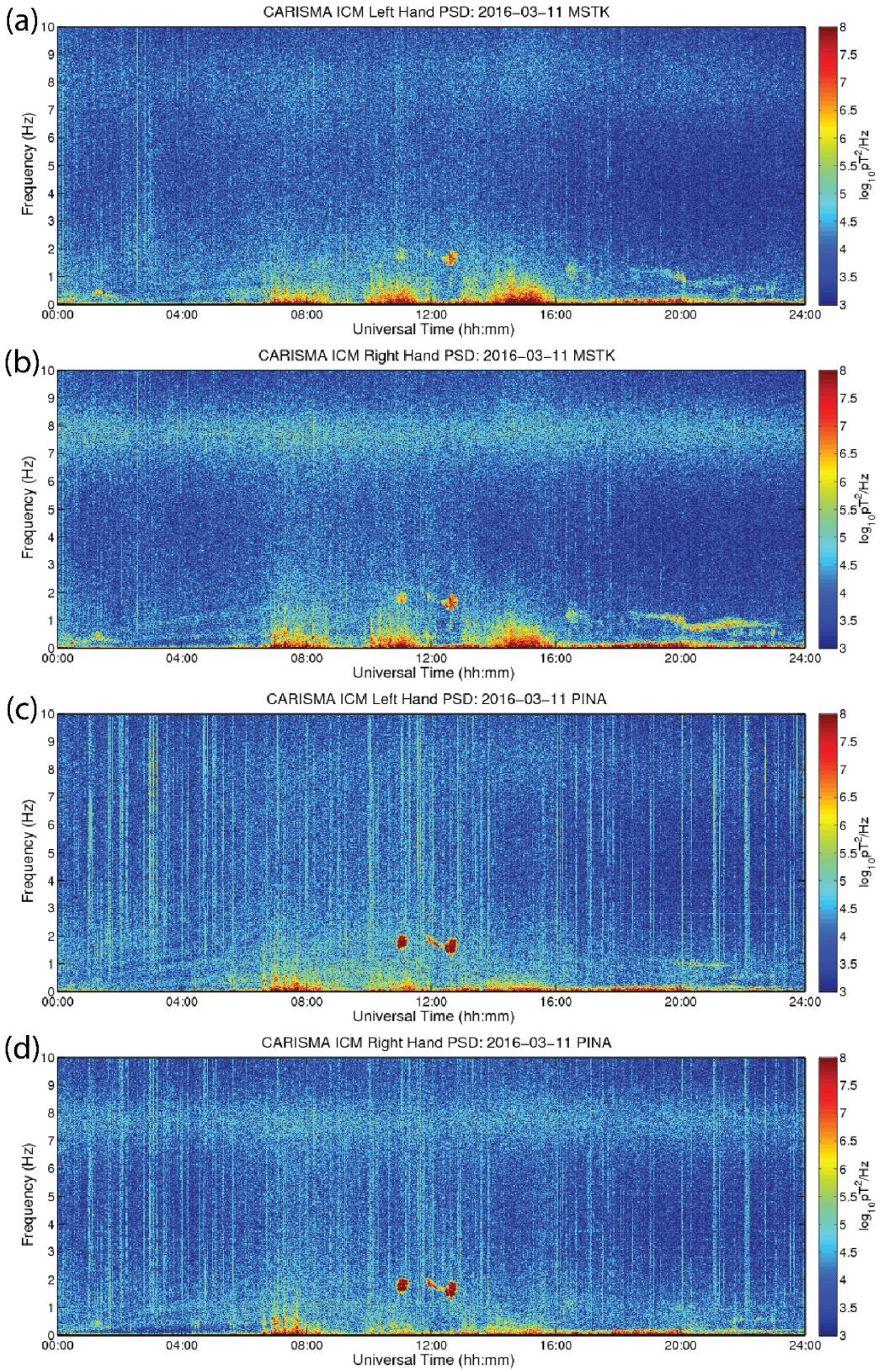

Figure 5-5: Ground induction coil data showing comb-like spectral features associated with the IAR from ~02:00 to 07:00 UTC. (a, b, c, d) Show right hand and left hand polarization for the Ministik Lake (MSTK) and Pinawa (PINA) stations respectively.

This shows that the ionospheric Alfvén resonator was likely active during the interval of the e-POP/Swarm conjunction, albeit being observed at significantly different and lower mid-latitudes than the arcs observed by e-POP. Unfortunately, the CARISMA induction coil magnetometers closer to the spacecraft conjunctions with the discrete auroral arcs were either noisy or inactive during the interval.

No clear evidence for similar spectral comb structures which could be related to the IAR were observed in any of the in-situ satellite magnetic field data (e.g., Figure 5-3 c) although this would not necessarily be expected given the rapid transit of the spacecraft and the limited magnetic resolution of the Swarm VFM compared to the terrestrial induction coil magnetometers. However, modelling of the IAR [*Lysak*, 1991] makes predictions about the ratio and relative phase of the electric and magnetic fields. In the case of a pure travelling wave, the E/B ratio would tend to the Alfvén speed and the fields would be nearly 180° out of phase. For the strongly ionospherically reflected case, where incident and reflected waves interfere inside the IAR, the phase difference would be within ±90° and the E/B ratio would have large, periodic variations as a function of frequency corresponding to the Eigen frequencies of the IAR.

Grzesiak [2000] previously reported observations (Figure 5-6, left) of phase structures similar to those predicted by the Lysak IAR model (Figure 5-6, right) by calculating histograms of the phase difference between electric and magnetic data captured by the Freja spacecraft [*Freja Magnetic Field Experiment Team*, 1994; *Marklund et al.*, 1994].

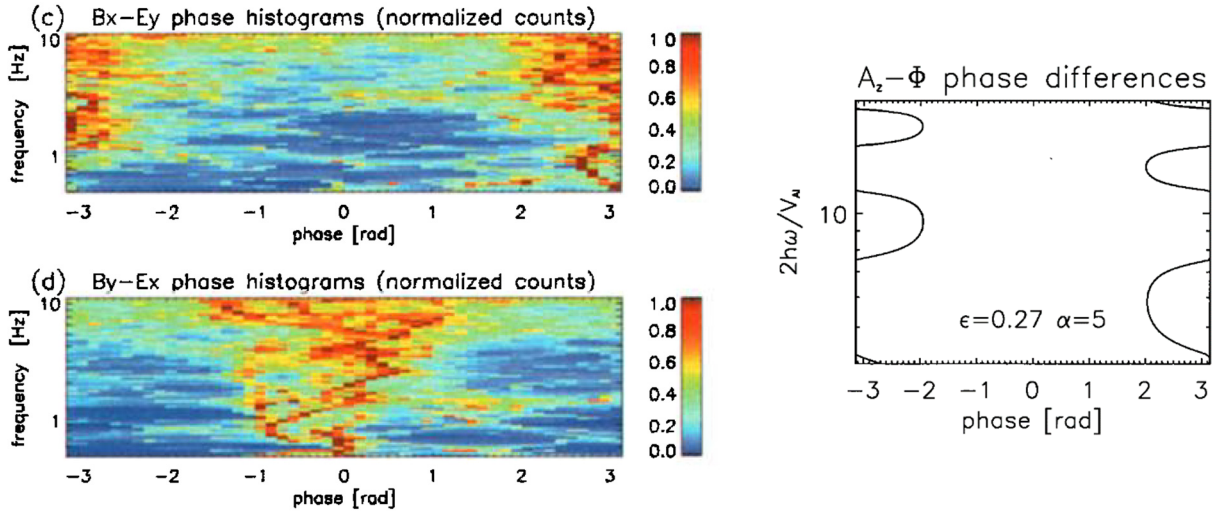

Figure 5-6: Previous in-situ Freja observations attributed to the presence of the IAR. Observed phase histogram structures (left) similar to those predicted by the Lysak IAR model (right). Reproduced from Grzesiak [2000].

Figure 5-4 applies the same phase histogram technique used by Grzesiak [2000] to the Swarm A data for the quiet interval in E_{North}/B_{East} coordinates (Figure 5-4 panel j) and the auroral region in E_{North}/B_{East} and E_{East}/ B_{North} coordinates (Figure 5-4, panels k and l respectively). Phase differences are only included in the histogram of occurrence when they exceed the same cross-power threshold used in Figure 5-3 f to exclude non-physical background noise. In the quiet interval (Figure 5-4 j) this gives no phase information above ~1 Hz as expected. However, in the auroral interval the histogram shows results similar to those found by Grzesiak [2000] and predicted by Lysak [1991]. The phase difference between the electric and magnetic fields is clustered around -45° for E_{North}/B_{East} (Figure 5-4, panel k) while the phase difference for E_{East}/ B_{North} (Figure 5-4, panel l) was noisier but clustered around 135°. The shift of 180° resulting from our calculating from fixed components, rather than the Alfvénic potentials themselves and the difference in sign of the cross product between the coordinates.

While noisy, both of the polarization histograms for the discrete arc interval show evidence of the structured fluctuations in the phase expected for the IAR and predicted in the Lysak [1991] model. It should be noted that since Swarm A crosses the auroral region in only ~20 seconds, there are only 320 samples (16 sps) of data available. This significantly restricts the statistical power of the phase histogram technique compared to Grzesiak [2000]. Nevertheless, despite this limited interval and the noise present in the electric field data, the Swarm A observes the same phase structuring observed by Grzesiak [2000] and predicted by Lysak [1991].

In this model, the harmonics of the IAR should create a modulation in phase which has the same structure and is hence coincident with the extrema in the E/B amplitude ratios (which are over-plotted in red on an arbitrary linear scale) as a function of frequency. Although the data are noisy, there is some evidence for this feature in the data – and on a linear scale there are clear (albeit small amplitude) somewhat periodic modulations in the E/B amplitude ratio. These are potentially consistent with a role for the IAR in at least some of the dynamic fine structure seen inside the discrete auroral arcs.

Taken together the e-POP and Swarm observations show Alfvénic wave activity, potentially modulated by the IAR, coincident with and at the same spatial and temporal scales as the structuring and dynamics of the discrete arcs observed by the e-POP FAI magnetically conjugate below. These observations are also compatible with a potentially causative role for Alfvén waves

in discrete auroral arc electron acceleration in the low density (high Alfvén speed) region at the top of the IAR, such as proposed by Chaston et al. [2002].

5.5 Discussion and Conclusions

We have presented a case study of the dynamics of the fine structure inside two discrete auroral arcs observed during a near magnetic conjunction between e-POP and the Swarm A and C spacecraft. High cadence imaging from e-POP allowed us to resolve dynamics of the fine structure inside double discrete auroral arcs that showed anti-parallel flows of internal features along the arcs, as well as 1-10 km scale features that evolve on second timescales. The e-POP spacecraft observed magnetic perturbations, inferred to be Alfvén waves, when the spacecraft was magnetically conjugate to these dynamic auroral features. The scale-size of these presumed waves, as seen in the e-POP magnetic field, matches that of the small-scale dynamic optical features observed in fine structure inside both discrete arcs. Similar perturbations were also observed magnetically by both the Swarm A and C spacecraft, and in electric field perturbations by Swarm A, at locations inferred to be close to the discrete arcs extrapolated from e-POP to the nearby Swarm A and C passes. The characteristics of the amplitude and phase of the ratio of electric and magnetic perturbations seen by Swarm A as a function of frequency closely matches the calculated local Alfvén speed at frequencies above ~1 Hz providing strong evidence that these perturbations were Alfvén waves. Moreover, there was some evidence of periodic modulations in the amplitude ratio and the phase difference between the electric and magnetic fields measured by Swarm A that match the predictions of Lysak [1991] for the structuring of the fields by the Ionospheric Alfvén Resonator. These modulations are very similar to the previous in-situ observations made by the Freja satellite and reported by Grzesiak [2000]. Taken together, these observations suggest that the structuring and dynamics of the discrete arcs observed in this event was related to the electrodynamics of incident and ionospherically reflected and interfering Alfvén waves, potentially modulated by structuring as a function of frequency introduced by reflections from both the top and the bottom of the Ionospheric Alfvén Resonator.

5.6 Acknowledgments, and Data

Work on the project was supported by the Canadian Space Agency under grants CARISMA-MIC. D. M. Miles is supported by an NSERC PGSD graduate scholarship, and by funding from the Canadian Space Agency. I. R. Mann is supported by a Discovery Grant from Canadian NSERC.

I. P. Pakhotin was supported by the ESA STSE Swarm+ Innovation grant 4000114090/15/NL/MP. This study makes use of data from the e-POP spacecraft mission, which is funded by the Canadian Space Agency. e-POP data can be accessed online at http://epop.phys.ucalgary.ca/data.html. This study makes use of data from the Swarm spacecraft mission, which is funded and managed by the European Space Agency. Swarm data can be accessed online at http://earth.esa.int/swarm. The auroral imaging movie provided as Supporting Information S1 was produced using the FAITools library Version 2.2 available at http://epop.phys.ucalgary.ca/data.html. The International Reference Ionosphere Models was instantiated using the online tool available at http://wdc.kugi.kyoto-u.ac.jp/ionocond/sigcal/index.html.

Chapter 6: Conclusions and Future Work

The results presented in this thesis contribute to the advancement of space physics research through the development of improved and miniaturised fluxgate magnetometers, characterisation and calibration techniques, and new scientific results arising from magnetic data analysis techniques. These advances have been documented in the form of four journal articles that comprise the body of this thesis in Chapters 2-5 inclusive.

Chapter 2 presented the Magnetic Field Instrument (MGF) on the Enhanced Plasma Outflow Probe (e-POP). The MGF has been operating on-orbit since September 2013 providing high-cadence, high-resolution, and low-noise measurements of the Earth's magnetic field. This instrument design was subsequently extended into a radiation hardened, primarily digital fluxgate magnetometer design [*Miles et al.*, 2013] and miniaturised as described in Chapter 3.

Chapter 3 describes a miniature boom-mounted fluxgate magnetometer for CubeSats and appeared on the cover of the December 2016 issue of the Journal of Geophysical Research: Space Physics. The instrument will be demonstrated on the Ex-Alta 1 CubeSat as part of the QB50 mission and is currently scheduled for launch in early 2017. Its successful operation will demonstrate that scientifically useful magnetic surveys can be conducted from low-cost CubeSat platforms paving the way for future multi-spacecraft CubeSat constellation missions.

Chapter 4 used a novel calibration technique to compare the thermal gain stability of six experimental fluxgate sensors where the bobbin supporting the sense windings and the sensor base were constructed from different materials. The results showed that the historical Acuña et al. [1978] model for the fluxgate sensor thermal gain dependence over-estimated the impact of material properties by about a factor of two. Glass filled PEEK plastic was found to have good thermal stability paving the way for future lower-cost and more mechanically robust fluxgate sensors albeit with a modest impact on thermal stability.

Chapter 5 used conjugate measurements from e-POP and the Swarm A and C spacecraft during e-POP operation scheduled by the author. A case study is presented where the structuring and dynamics of discrete auroral arcs appears to be related to the electrodynamics of reflected and interfering Alfvén waves potentially modulated by the Ionospheric Alfvén Resonator. This fortuitous and temporary ad-hoc spacecraft conjunction demonstrates the scientific value that

could be derived from dense multi-spacecraft constellations with both magnetic and electric field measurements supported by high-cadence imaging for making significant research advances into auroral magnetosphere-ionosphere coupling and, in particular, the role of Alfvén waves. The disparity between the magnetic fields measured at 1.4° cross-track separation between Swarm A and C shows the need for closer proximity measurements. The ratio of the electric and magnetic perturbations measured by Swarm A shows the presence of Alfvén waves. Finally, conjugate magnetic measurements and auroral imaging from e-POP allows the Alfvén waves to be linked to the dynamics and small-scale structure of the associated aurora.

The instruments and techniques developed as part of this thesis point to the scientific value of at least two future missions. The scientific utility of the temporary Swarm/e-POP three-spacecraft constellation used in Chapter 5 argues for a future mission employing multiple spacecraft in a tight formation. The spacecraft should be equipped with at least high cadence auroral imaging, a high cadence electric field instrument, and a high-cadence magnetometer such as those presented in this thesis. A sub-orbital sounding rocket, and daughter payloads, each with high cadence magnetometers could be use to study potential Alfvénic auroral acceleration altitudes as low as a few thousand kilometers. A more detailed preliminary presentation of such a sounding rocket concept is provided below.

The role of Alfvén waves in magnetosphere-ionosphere coupling remains open from an observational standpoint largely due to the challenges of resolving the spatio-temporal evolution at appropriate scales. Traditionally, an electrostatic potential drop in what is called the auroral acceleration region is invoked to energize auroral electrons [e.g., *Swift*, 1981]. However, in a paper in Science, Keiling et al. [2003] showed that electromagnetic near-Earth Alfvén waves transport sufficient energy into the auroral region to power the aurora. Keiling et al. [2003] used satellites at ~30,000 km altitude to characterize the net energy that Alfvén waves carry towards the Earth, and showed that it is sufficient to power the aurora. Dombeck et al. [2005] showed that about half of the Alfvén wave energy observed at 44,000 km was lost by 3,500 km. However, what happens to the Alfvénic wave energy below this altitude or what role it may have in accelerating the electrons that cause the aurora is unclear.

Single satellite measurements in low-Earth orbit are poorly suited to studying this interaction because both Alfvén waves and auroral electrons travel parallel to the Earth's magnetic field while

spacecraft in low-Earth orbit necessarily travel approximately orthogonal to the field at auroral latitudes. However, a BlackBrant-12 sounding rocket launched from under the auroral zone could reach an altitude of ~1,500 km flying essentially parallel to the local magnetic field. Such a measurement profile would contribute to our understanding of the link between Alfvén waves and auroral dynamics [*Trondsen et al.*, 1997; *Stasiewicz et al.*, 2000] and could test for auroral electron acceleration at altitudes lower than are typically expected but which are theoretically possible given modelling of the wave-particle interactions [e.g., *Watt et al.*, 2005]. Prior rockets have observed large down-going Alfvén waves at these altitudes [e.g., *Boehm et al.*, 1990] and comparing the wave electrodynamic fields to auroral forms would be exciting.

If instrumented with a modern fluxgate magnetometer (as described in Chapters 2 and 3), an electric field instrument, and a keV electron telescope, such a sounding rocket mission could characterize Alfvénic Poynting Flux and keV electron population dynamics thereby characterising the altitudes of energy transfer between ~100 and ~1,500 km nominally along a single magnetic field line (Figure 6-1, left). These measurements could provide novel insight into the energy coupling mechanism between Alfvén waves and the aurora. Such a mission could be launched from the Poker Flat launch range in Alaska or alternatively from the SvalRak launch site in Svalbard, Norway albeit on a BlackBrant-10 albeit with a reduced 900 km apogee due to restrictions on sounding rockets overflying populated areas from this launch site.

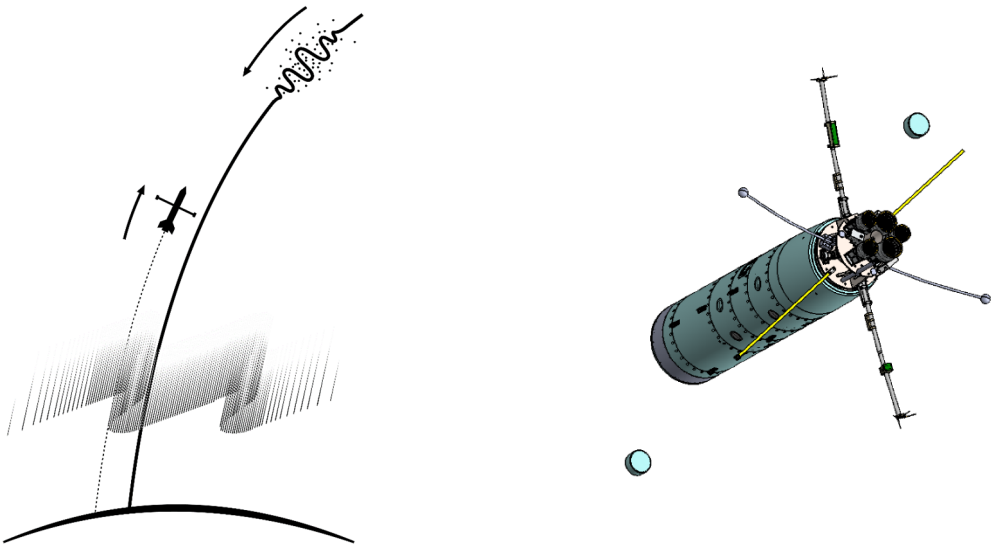

Figure 6-1: A potential future sounding rocket application. (left) A sounding rockets could travel parallel to an auroral magnetic field line and study where and how wave particle interaction accelerates the electrons that interact with the atmosphere to create aurora. Image credit: Andy Kale (right) Deploying daughter payloads with miniature instruments at altitude can help distinguish spatial from temporal variations. Image credit: Andøya Space Center.

Flying along a single magnetic field line simplifies data interpretation as, nominally, only one long linked plasma region is being sampled. However, in reality, the rocket will not fly exactly along the background field and the perpendicular extent of a 'field line' is not well defined. Further, with a single moving rocket platform, the question of spatial versus temporal evolution remains challenging to resolve. To help address this, the rocket could deploy daughter payloads after reaching altitude to create a moving multipoint measurement constellation (Figure 6-1, right). A first implementation of this measurement technique was developed under the auspice of the University of Oslo led 4DSpace Strategic Research Initiative. A technical demonstration of this multipoint technique was to be carried out on the MaxiDusty-1b sounding rocket in 2016 using daughter payloads adapted from the miniature fluxgate magnetometer described in Chapter 3. Unfortunately, due to a failure in the main rocket payload, the daughter payloads were never released. Despite this setback, these miniature instrument payloads are now available for future rocket campaigns and there remain attractive opportunities for advancing our understanding of the role of Alfvén waves in magnetosphere-ionosphere coupling.

Anticipated improvements in instrument performance will likely create new future applications for fluxgate magnetometers. Renewed interest in engineering low-noise fluxgate cores [e.g., *Narod*, 2014] may enable miniature sensors such as those described in Chapter 3 to achieve noise performance equal to that historically required larger and higher power sensors. Significant reductions in instrumental noise floor would allow fluxgates to compete with induction coil magnetometers at frequencies above the historical ~1 Hz crossover point. In some applications, this might allow the flight of a single high-cadence and low-noise fluxgate rather than a traditional pairing of fluxgate and induction coil magnetometers. In terrestrial applications, such a fluxgate might provide the high cadence measurements required to resolve shallow depths in magnetotelluric studies possibly removing the need for additional use of an induction coil magnetometer.

Fluxgate magnetometers have been an essential research tool in the decades since their invention. As demonstrated throughout this thesis, modern instruments with low magnetic noise, high measurement cadence, and modest power, mass, and volume requirements will continue to enable high-impact science at the forefront of international research priorities.

References

Acuña, M. H. (2002), Space-based magnetometers, *Rev. Sci. Instrum.*, *73*(11), 3717–3736.

Acuña, M. H., and C. J. Pellerin (1969), A Miniature Two-Axis Fluxgate Magnetometer, *IEEE Trans. Geosci. Electron.*, *7*(4), 252–260, doi:10.1109/TGE.1969.271360.

Acuña, M. H., C. S. Scearce, J. Seek, and J. Scheifele (1978), *The MAGSAT vector magnetometer: A precision fluxgate magnetometer for the measurement of the geomagnetic field*, National Aeronautics and Space Administration.

Alfven, H., and C. G. Falthammar (1963), *Cosmical Electrodynamics, Fundamental Principles 2nd ed., Clarendon*, Oxford.

Anderson, B. J., K. Takahashi, and B. A. Toth (2000), Sensing global Birkeland currents with Iridium engineering magnetometer data, *Geophys Res Lett*, *27*(24), 4045–4048.

André, M., and A. Yau (1997), Theories and observations of ion energization and outflow in the high latitude magnetosphere, *Space Sci. Rev.*, *80*(1–2), 27–48.

Angelopoulos, V. (2009), The THEMIS mission, in *The THEMIS Mission*, pp. 5–34, Springer.

Aschenbrenner, H., and G. Goubau (1936), Eine anordnung zur registrierung rascher magnetischer störungen, *Hochfrequenztech. Elektroakust.*, *47*(6), 177–181.

Auster, H. U. et al. (2009), The THEMIS fluxgate magnetometer, in *The THEMIS Mission*, pp. 235–264, Springer.

Baker, D. N. (2000), The occurrence of operational anomalies in spacecraft and their relationship to space weather, *IEEE Trans. Plasma Sci.*, *28*(6), 2007–2016, doi:10.1109/27.902228.

Baker, D. N., X. Li, A. Pulkkinen, C. M. Ngwira, M. L. Mays, A. B. Galvin, and K. D. C. Simunac (2013), A major solar eruptive event in July 2012: Defining extreme space weather scenarios, *Space Weather*, *11*(10), 2013SW000963, doi:10.1002/swe.20097.

Bandyopadhyay, S., G. P. Subramanian, R. Foust, D. Morgan, S.-J. Chung, and F. Y. Hadaegh (2015), A Review of Impending Small Satellite Formation Flying Missions, in *Proceedings of the 53rd AIAA Aerospace Sciences Meeting, Kissimmee FL*.

Basu, S. et al. (2001), Ionospheric effects of major magnetic storms during the International Space Weather Period of September and October 1999: GPS observations, VHF/UHF scintillations, and in situ density structures at middle and equatorial latitudes, *J. Geophys. Res. Space Phys.*, *106*(A12), 30389–30413, doi:10.1029/2001JA001116.

Bekkeng, T. A., K. S. Jacobsen, J. K. Bekkeng, A. Pedersen, T. Lindem, J. P. Lebreton, and J. I. Moen (2010), Design of a multi-needle Langmuir probe system, *Meas. Sci. Technol.*, *21*(8), 85903.

Belyaev, P. P., S. V. Polyakov, V. O. Rapoport, and V. Y. Trakhtengerts (1990), The ionospheric Alfvén resonator, *J. Atmospheric Terr. Phys.*, *52*(9), 781–788, doi:10.1016/0021-9169(90)90010-K.

Bilitza, D., D. Altadill, Y. Zhang, C. Mertens, V. Truhlik, P. Richards, L.-A. McKinnell, and B. Reinisch (2014), The International Reference Ionosphere 2012–a model of international collaboration, *J. Space Weather Space Clim.*, *4*, A07.

Birkeland, K. (1908), *The Norwegian aurora polaris expedition 1902-1903*, H. Aschelhoug & Company.

Boehm, M. H., C. W. Carlson, J. P. McFadden, J. H. Clemmons, and F. S. Mozer (1990), High-resolution sounding rocket observations of large-amplitude Alfvén waves, *J. Geophys. Res. Space Phys.*, *95*(A8), 12157–12171, doi:10.1029/JA095iA08p12157.

Boscher, D., S. Bourdarie, P. O'Brien, and T. Guild (2010), IRBEM library V4. 3, 2004–2008, *ONERA-DESP Toulouse Fr. Aerosp. Corp. Wash. DC*.

Boteler, D. H. (2006), The super storms of August/September 1859 and their effects on the telegraph system, *Adv. Space Res.*, *38*(2), 159–172, doi:10.1016/j.asr.2006.01.013.

Boteler, D. H., R. J. Pirjola, and H. Nevanlinna (1998), The effects of geomagnetic disturbances on electrical systems at the Earth's surface, *Adv. Space Res.*, *22*(1), 17–27, doi:10.1016/S0273-1177(97)01096-X.

Brown, P., T. Beek, C. Carr, H. O'Brien, E. Cupido, T. Oddy, and T. S. Horbury (2012), Magnetoresistive magnetometer for space science applications, *Meas. Sci. Technol.*, *23*(2), 25902.

Brown, P. et al. (2014), Space magnetometer based on an anisotropic magnetoresistive hybrid sensor, *Rev. Sci. Instrum.*, *85*(12), 125117.

Burch, J. L., T. E. Moore, R. B. Torbert, and B. L. Giles (2016), Magnetospheric multiscale overview and science objectives, *Space Sci. Rev.*, *199*(1–4), 5–21.

Butvin, P., M. Janošek, P. Ripka, B. Butvinová, P. Švec, M. Kuzminski, D. Janičkovič, and G. Vlasák (2012), Field annealed closed-path fluxgate sensors made of metallic-glass ribbons, *Sens. Actuators Phys.*, *184*, 72–77.

Cagniard, L. (1953), Basic theory of the magneto-telluric method of geophysical prospecting, *GEOPHYSICS*, *18*(3), 605–635, doi:10.1190/1.1437915.

Carr, C. et al. (2005), The Double Star magnetic field investigation: Instrument design, performance and highlights of the first year's observations, in *Annales Geophysicae*, vol. 23, pp. 2713–2732.

Chaston, C. C., J. W. Bonnell, C. W. Carlson, M. Berthomier, L. M. Peticolas, I. Roth, J. P. McFadden, R. E. Ergun, and R. J. Strangeway (2002), Electron acceleration in the ionospheric Alfven resonator, *J. Geophys. Res. Space Phys.*, *107*(A11), 1413, doi:10.1029/2002JA009272.

Choi, S. O., S. Kawahito, Y. Matsumoto, M. Ishida, and Y. Tadokoro (1996), An integrated micro fluxgate magnetic sensor, *Sens. Actuators Phys.*, *55*(2), 121–126.

Cogger, L. et al. (2014), Fast Auroral Imager (FAI) for the e-POP Mission, *Space Sci. Rev.*, *189*(1–4), 15–25, doi:10.1007/s11214-014-0107-x.

Dombeck, J., C. Cattell, J. R. Wygant, A. Keiling, and J. Scudder (2005), Alfvén waves and Poynting flux observed simultaneously by Polar and FAST in the plasma sheet boundary layer, *J. Geophys. Res. Space Phys.*, *110*(A12), A12S90, doi:10.1029/2005JA011269.

Drljaca, P. M., P. Kejik, F. Vincent, and R. S. Popovic (2003), Low noise CMOS micro-fluxgate magnetometer, in *TRANSDUCERS, Solid-State Sensors, Actuators and Microsystems, 12th International Conference on, 2003*, vol. 1, pp. 304–307, IEEE.

Dungey, J. W. (1963), Interactions of solar plasma with the geomagnetic field, *Planet. Space Sci.*, *10*, 233–237, doi:10.1016/0032-0633(63)90020-5.

Escoubet, C. P., M. Fehringer, and M. Goldstein (2001), Introduction the Cluster mission, in *Annales Geophysicae*, vol. 19, pp. 1197–1200.

Evans, D. S. (1974), Precipitating electron fluxes formed by a magnetic field aligned potential difference, *J. Geophys. Res.*, *79*(19), 2853–2858, doi:10.1029/JA079i019p02853.

Finlay, C. C., N. Olsen, and L. Tøffner-Clausen (2015), DTU candidate field models for IGRF-12 and the CHAOS-5 geomagnetic field model, *Earth Planets Space*, *67*(1), doi:10.1186/s40623-015-0274-3.

Forslund, Å., S. Belyayev, N. Ivchenko, G. Olsson, T. Edberg, and A. Marusenkov (2007), Miniaturized digital fluxgate magnetometer for small spacecraft applications, *Meas. Sci. Technol.*, *19*(1), 15202.

Forsyth, C., I. J. Rae, I. R. Mann, and I. P. Pakhotin (2017), Identifying intervals of temporally invariant field-aligned currents from Swarm: Assessing the validity of single-spacecraft methods, *J. Geophys. Res. Space Phys.*, 2016JA023708, doi:10.1002/2016JA023708.

Freja Magnetic Field Experiment Team (1994), Magnetic field experiment on the Freja satellite, *Space Sci. Rev.*, *70*(3–4), 465–482.

Friis-Christensen, E., H. Lühr, D. Knudsen, and R. Haagmans (2008), Swarm – An Earth Observation Mission investigating Geospace, *Adv. Space Res.*, *41*(1), 210–216, doi:10.1016/j.asr.2006.10.008.

Geyger, A. W. (1962), The ring-core magnetometer - A new type of second-harmonic flux-gate magnetometer, *Trans. Am. Inst. Electr. Eng. Part Commun. Electron.*, *81*(1), 65–73, doi:10.1109/TCE.1962.6373206.

Gjerloev, J. W., and R. A. Hoffman (2000), Height-integrated conductivity in auroral substorms: 2. Modeling, *J. Geophys. Res. Space Phys.*, *105*(A1), 227–235, doi:10.1029/1999JA900353.

Gjerloev, J. W., S. Ohtani, T. Iijima, B. Anderson, J. Slavin, and G. Le (2011), Characteristics of the terrestrial field-aligned current system, in *Annales Geophysicae*, vol. 29, pp. 1713–1729, Copernicus GmbH.

Goodwin, L. V. et al. (2015), Swarm in situ observations of F region polar cap patches created by cusp precipitation, *Geophys. Res. Lett.*, *42*(4), 2014GL062610, doi:10.1002/2014GL062610.

Grey, J. P. (2016), *Power Budget for Ex-Alta 1*, Technical Report, University of Alberta.

Grzesiak, M. (2000), Ionospheric Alfvén resonator as seen by Freja satellite, *Geophys. Res. Lett.*, *27*(7), 923–926, doi:10.1029/1999GL010747.

Gummow, R. A. (2002), GIC effects on pipeline corrosion and corrosion control systems, *J. Atmospheric Sol.-Terr. Phys.*, *64*(16), 1755–1764, doi:10.1016/S1364-6826(02)00125-6.

Hand, E. (2015a), Startup liftoff, *Science*, *348*(6231), 172–177.

Hand, E. (2015b), Thinking inside the box, *Science*, *348*(6231), 176–177.

Hardy, D. A., M. S. Gussenhoven, R. Raistrick, and W. J. McNeil (1987), Statistical and functional representations of the pattern of auroral energy flux, number flux, and conductivity, *J. Geophys. Res. Space Phys.*, *92*(A11), 12275–12294, doi:10.1029/JA092iA11p12275.

Heinzel, G., A. Rüdiger, and R. Schilling (2002), *Spectrum and spectral density estimation by the Discrete Fourier transform (DFT), including a comprehensive list of window functions and some new at-top windows*, Max-Planck-Institut fur Gravitationsphysik, Teilinstitut Hannover.

Heliophysics Roadmap Team (2014), *Our Dynamic Space Environment: Heliophysics Science and Technology Roadmap for 2014-2033*, National Aeronautics and Space Administration.

Hughes, W. J. (1974), The effect of the atmosphere and ionosphere on long period magnetospheric micropulsations, *Planet. Space Sci.*, *22*(8), 1157–1172, doi:10.1016/0032-0633(74)90001-4.

Iijima, T., and T. A. Potemra (1976), The amplitude distribution of field-aligned currents at northern high latitudes observed by Triad, *J. Geophys. Res.*, *81*(13), 2165–2174, doi:10.1029/JA081i013p02165.

Iijima, T., and T. A. Potemra (1978), Large-scale characteristics of field-aligned currents associated with substorms, *J. Geophys. Res. Space Phys.*, *83*(A2), 599–615, doi:10.1029/JA083iA02p00599.

Johnson, C. Y. (1969), Ion and neutral composition of the ionosphere., *Ann. IQSY*, *5*, 197–213.

Jones, J. B. L., R. D. Bentley, R. Hunter, R. H. A. Iles, G. C. Taylor, and D. J. Thomas (2005), Space weather and commercial airlines, *Adv. Space Res.*, *36*(12), 2258–2267, doi:10.1016/j.asr.2004.04.017.

Keiling, A., J. R. Wygant, C. A. Cattell, F. S. Mozer, and C. T. Russell (2003), The global morphology of wave Poynting flux: Powering the aurora, *Science*, *299*(5605), 383–386.

Kimball, D. S. (1960), *A Study of the Aurora of 1859*, Report, Geophysical Institute at the University of Alaska.

Kivelson, M. G., and C. T. Russell (1995), *Introduction to space physics*, Cambridge university press.

Knudsen, D. J., M. C. Kelley, G. D. Earle, J. F. Vickrey, and M. Boehm (1990), Distinguishing Alfvén waves from quasi-static field structures associated with the discrete aurora: Sounding rocket and HILAT satellite measurements, *Geophys. Res. Lett.*, *17*(7), 921–924, doi:10.1029/GL017i007p00921.

Knudsen, D. J., M. C. Kelley, and J. F. Vickrey (1992), Alfvén waves in the auroral ionosphere: A numerical model compared with measurements, *J. Geophys. Res. Space Phys.*, *97*(A1), 77–90, doi:10.1029/91JA02300.

Knudsen, D. J., J. K. Burchill, T. G. Cameron, G. A. Enno, A. Howarth, and A. W. Yau (2015), The CASSIOPE/e-POP Suprathermal Electron Imager (SEI), *Space Sci. Rev.*, *189*(1–4), 65–78, doi:10.1007/s11214-015-0151-1.

Knudsen, D. J., J. K. Burchill, S. C. Buchert, A. I. Eriksson, R. Gill, J.-E. Wahlund, L. Åhlen, M. Smith, and B. Moffat (2017), Thermal ion imagers and Langmuir probes in the Swarm electric field instruments, *J. Geophys. Res. Space Phys.*, 2016JA022571, doi:10.1002/2016JA022571.

Koen, J., and T. Gaunt (2003), Geomagnetically induced currents in the Southern African electricity transmission network, in *Power Tech Conference Proceedings, 2003 IEEE Bologna*, vol. 1, p. 7 pp. Vol.1-pp.

Le, G., J. A. Slavin, and R. J. Strangeway (2010), Space Technology 5 observations of the imbalance of regions 1 and 2 field-aligned currents and its implication to the cross-polar cap Pedersen currents, *J. Geophys. Res. Space Phys.*, *115*(A7), A07202, doi:10.1029/2009JA014979.

Leitner, S., A. Valavanoglou, P. Brown, C. Hagen, W. Magnes, B. J. Whiteside, C. M. Carr, M. Delva, and W. Baumjohann (2015), Design of the magnetoresistive magnetometer for ESA's SOSMAG project, *IEEE Trans. Magn.*, *51*(1), 1–4.

Lessard, M. R., and D. J. Knudsen (2001), Ionospheric reflection of small-scale Alfvén waves, *Geophys. Res. Lett.*, *28*(18), 3573–3576, doi:10.1029/2000GL012529.

Lessard, M. R., E. J. Lund, H. M. Kim, M. J. Engebretson, and K. Hayashi (2011), Pi1B pulsations as a possible driver of Alfvénic aurora at substorm onset, *J. Geophys. Res. Space Phys.*, *116*(A6), A06203, doi:10.1029/2010JA015776.

Li, X., D. N. Baker, T. P. O'Brien, L. Xie, and Q. G. Zong (2006), Correlation between the inner edge of outer radiation belt electrons and the innermost plasmapause location, *Geophys. Res. Lett.*, *33*(14), L14107, doi:10.1029/2006GL026294.

Linear Technology Corporation (2014), *LTC2641/LTC2642 Datasheet*, Linear Technology Corporation.

Lühr, H., J. Warnecke, L. J. Zanetti, P. A. Lindqvist, and T. J. Hughes (1994), Fine structure of field-aligned current sheets deduced from spacecraft and ground-based observations: Initial FREJA results, *Geophys. Res. Lett.*, *21*(17), 1883–1886, doi:10.1029/94GL01278.

Lühr, H., J. F. Warnecke, and M. K. A. Rother (1996), An algorithm for estimating field-aligned currents from single spacecraft magnetic field measurements: a diagnostic tool applied to Freja satellite data, *IEEE Trans. Geosci. Remote Sens.*, *34*(6), 1369–1376, doi:10.1109/36.544560.

Lysak, R. L. (1990), Electrodynamic coupling of the magnetosphere and ionosphere, *Space Sci. Rev.*, *52*(1–2), 33–87, doi:10.1007/BF00704239.

Lysak, R. L. (1991), Feedback instability of the ionospheric resonant cavity, *J. Geophys. Res. Space Phys.*, *96*(A2), 1553–1568.

Mann, I. R. et al. (2008), The Upgraded CARISMA Magnetometer Array in the THEMIS Era, *Space Sci. Rev.*, *141*(1–4), 413–451, doi:10.1007/s11214-008-9457-6.

Marklund, G. T., L. G. Blomberg, P.-A. Lindqvist, C.-G. Fälthammar, G. Haerendel, F. S. Mozer, A. Pedersen, and P. Tanskanen (1994), The Double Probe Electric Field Experiment on Freja: Experiment Description and First Results, in *The Freja Mission*, edited by R. Lundin, G. Haerendel, and S. Grahn, pp. 79–104, Springer Netherlands.

Matandirotya, E., R. R. Van Zyl, D. J. Gouws, and E. F. Saunderson (2013), Evaluation of a commercial-off-the-shelf fluxgate magnetometer for cubesat space magnetometry, *J. Small Satell.*, *2*(1), 133–146.

Maynard, T., N. Smith, and S. Gonzalez (2013), *Solar Storm Risk to the North American Electric Grid*, Lloyd's.

Mazur, J. E., W. R. Crain, M. D. Looper, D. J. Mabry, J. B. Blake, A. W. Case, M. J. Golightly, J. C. Kasper, and H. E. Spence (2011), New measurements of total ionizing dose in the lunar environment, *Space Weather*, *9*(7).

McPherron, R. L. (2005), Magnetic Pulsations: Their Sources and Relation to Solar Wind and Geomagnetic Activity, *Surv. Geophys.*, *26*(5), 545–592, doi:10.1007/s10712-005-1758-7.

Mehrparvar, A., D. Pignatelli, J. Carnahan, R. Munakata, W. Lan, A. Toorian, A. Hutputanasin, and S. Lee (2014), *CubeSat Design Specification (CDS) Rev 13*, California Polytechnic State University, San Luis Obispo, California, USA.

Mende, S. B., S. E. Harris, H. U. Frey, V. Angelopoulos, C. T. Russell, E. Donovan, B. Jackel, M. Greffen, and L. M. Peticolas (2009), The THEMIS array of ground-based observatories for the study of auroral substorms, in *The THEMIS Mission*, pp. 357–387, Springer.

Merayo, J. é M. G., J. L. Jørgensen, E. Friis-Christensen, P. Brauer, F. Primdahl, P. S. Jørgensen, T. H. Allin, and T. Denver (2008), The Swarm Magnetometry Package, in *Small Satellites for Earth Observation*, edited by R. Sandau, H.-P. Röser, and A. Valenzuela, pp. 143–151, Springer Netherlands.

Michelena, M. D. (2013), Commercial Off-The-Shelf GMR Based Sensor on Board Optos Picosatellite, in *Giant Magnetoresistance (GMR) Sensors*, pp. 181–210, Springer.

Miles, D. M. (2013), Towards a Radiation Hardened Fluxgate Magnetometer for Space Physics Applications, Master's Thesis, University of Alberta, Edmonton, Alberta, Canada.

Miles, D. M., J. R. Bennest, I. R. Mann, and D. K. Millling (2013), A radiation hardened digital fluxgate magnetometer for space applications, *Geosci. Instrum. Methods Data Syst.*, *2*(2), 213–224.

Miles, D. M. et al. (2016), A miniature, low-power scientific fluxgate magnetometer: A stepping-stone to cube-satellite constellation missions, *J. Geophys. Res. Space Phys.*, 2016JA023147, doi:10.1002/2016JA023147.

Miles, D. M., I. R. Mann, I. P. Pakhotin, D. J. Knudsen, J. K. Burchill, A. Howarth, and D. D. Wallis (2017a), Alfvénic dynamics and structuring of discrete auroral arcs: Swarm and e-POP observations, *Geophys Res Lett*, *In Prep*.

Miles, D. M., I. R. Mann, A. Kale, B. B. Narod, J. R. Bennest, D. Barona, D. K. Milling, and M. J. Unsworth (2017b), Thermal stability of fluxgate magnetometer sensors constructed from different materials, *Geosci. Instrum. Methods Data Syst.*, *In Prep*.

Moldwin, M. (2008), *An Introduction to Space Weather*, Cambridge University Press.

Mottez, F. (2015), Alfven wave acceleration of particles in the aurora, *Plasma Phys. Control. Fusion*, *57*(1), 14011, doi:10.1088/0741-3335/57/1/014011.

Murphy, K. R., I. R. Mann, I. J. Rae, C. L. Waters, H. U. Frey, A. Kale, H. J. Singer, B. J. Anderson, and H. Korth (2013), The detailed spatial structure of field-aligned currents comprising the substorm current wedge, *J. Geophys. Res. Space Phys.*, *118*(12), 7714–7727.

Muylaert, J., R. Reinhard, C. Asma, J. Buchlin, P. Rambaud, and M. Vetrano (2009), QB50: An international network of 50 cubesats for multi-point, in-situ measurements in the lower

thermosphere and for re-entry research, in *ESA Atmospheric Science Conference, Barcelona, Spain*, pp. 7–11.

NanoRacks LLC (2013), NanoRacks CubeSat Deployer (NRCSD) Interface Control Document,

Narod, B., and R. Russell (1984), Steady-state characteristics of the capacitively loaded flux gate sensor, *IEEE Trans. Magn.*, *20*(4), 592–597.

Narod, B. B. (1982), *Transconductance Amplifier Design and Sensitivity Analysis*, University of British Columbia, Department of Geophysics and Astronomy, Geophysical Instrumentation Laboratory.

Narod, B. B. (2014), The origin of noise and magnetic hysteresis in crystalline permalloy ring-core fluxgate sensors, *Geosci. Instrum. Methods Data Syst.*, *3*(2), 201.

Narod, B. B., and J. R. Bennest (1990), Ring-core fluxgate magnetometers for use as observatory variometers, *Phys. Earth Planet. Inter.*, *59*(1–2), 23–28.

Ness, N. F., K. W. Behannon, R. P. Lepping, and K. H. Schatten (1971), Use of two magnetometers for magnetic field measurements on a spacecraft, *J. Geophys. Res.*, *76*(16), 3564–3573.

Nielsen, O. V., J. R. Petersen, F. Primdahl, P. Brauer, B. Hernando, A. Fernandez, J. M. G. Merayo, and P. Ripka (1995), Development, construction and analysis of the'OErsted'fluxgate magnetometer, *Meas. Sci. Technol.*, *6*(8), 1099.

Oberg, E. (2012), *Machinery's Handbook 29th Edition-Full Book*, Industrial Press.

Olson, W. P., and K. A. Pfitzer (1977), Magnetospheric magnetic field modeling, Annual Scientific Report, AFOSR Contract No, *F44620-75-C-0033*.

van der Pauw, L. J. (1958), A method of measuring specific resistivity and Hall effect of discs of arbitrary shape, *Philips Res Rep*, *13*, 1–9.

Petrucha, V., and P. Kašpar (2012), Measurement of the temperature dependence of the sensitivity and orthogonality of a triaxial vector magnetometer, *J Elect Eng*, *63*(7s), 31–34.

Petrucha, V., M. Janošek, and M. A. Azpúrua (2015), Vector feedback homogeneity and inner layout influence on fluxgate sensor parameters, *IEEE Trans. Instrum. Meas.*, *64*(5), 1285–1291.

Potemra, T. A. (1985), Field-aligned (Birkeland) currents, *Space Sci. Rev.*, *42*(3–4), 295–311.

Prikner, K., K. Mursula, J. Kangas, R. Kerttula, and F. Z. Feygin (2004), An effect of the ionospheric Alfvén resonator on multiband Pc1 pulsations, *Ann Geophys*, *22*(2), 643–651, doi:10.5194/angeo-22-643-2004.

Primdahl, F. (1970), Temperature compensation of fluxgate magnetometers, *IEEE Trans. Magn.*, *6*(4), 819–822.

Primdahl, F. (1979), The fluxgate magnetometer, *J. Phys. [E]*, *12*(4), 241.

Primdahl, F., and P. A. Jensen (1982), Compact spherical coil for fluxgate magnetometer vector feedback, *J. Phys. [E]*, *15*(2), 221.

Primdahl, F., O. V. Nielsen, J. R. Petersen, and P. Ripka (1994), High frequency fluxgate sensor noise, *Electron. Lett.*, *30*(6), 481–482.

Pumpkin Inc. (2007), *CubeSat Kit PCB Specification*, Pumpkin Inc.

Purucker, M., T. Sabaka, G. Le, J. A. Slavin, R. J. Strangeway, and C. Busby (2007), Magnetic field gradients from the ST-5 constellation: Improving magnetic and thermal models of the lithosphere, *Geophys. Res. Lett.*, *34*(24), L24306, doi:10.1029/2007GL031739.

Ratcliffe (1972), *An Introduction to Ionosphere and Magnetosphere*, CUP Archive.

Rees, M. H. (1969), Auroral electrons, *Space Sci. Rev.*, *10*(3), 413–441, doi:10.1007/BF00203621.

Ripka, P. (2001), *Magnetic sensors and magnetometers*, Artech House,.

Ripka, P. (2003), Advances in fluxgate sensors, *Sens. Actuators Phys.*, *106*(1), 8–14.

Ripka, P., M. Tondra, J. Stokes, and R. Beech (1999), AC-driven AMR and GMR magnetoresistors, *Sens. Actuators Phys.*, *76*(1), 225–230.

Ritter, P., and H. Lühr (2006), Curl-B technique applied to Swarm constellation for determining field-aligned currents, *Earth Planets Space*, *58*(4), 463–476, doi:10.1186/BF03351942.

Ritter, P., H. Lühr, and J. Rauberg (2013), Determining field-aligned currents with the Swarm constellation mission, *Earth Planets Space*, *65*(11), 9, doi:10.5047/eps.2013.09.006.

Robertson, P. A. (2000), Microfabricated fluxgate sensors with low noise and wide bandwidth, *Electron. Lett.*, *36*(4), 331–332.

Rostoker, G., J. C. Samson, F. Creutzberg, T. J. Hughes, D. R. McDiarmid, A. G. McNamara, A. V. Jones, D. D. Wallis, and L. L. Cogger (1995), CANOPUS—A ground-based instrument array for remote sensing the high latitude ionosphere during the ISTP/GGS program, *Space Sci. Rev.*, *71*(1–4), 743–760.

Rother, M., K. Schlegel, and H. Lühr (2007), CHAMP observation of intense kilometer-scale field-aligned currents, evidence for an ionospheric Alfvén resonator, in *Annales Geophysicae*, vol. 25, pp. 1603–1615.

Schrijver, C. J. et al. (2015), Understanding space weather to shield society: A global road map for 2015–2025 commissioned by COSPAR and ILWS, *Adv. Space Res.*, *55*(12), 2745–2807.

Schultz, A. (2009), EMScope: a continental scale magnetotelluric observatory and data discovery resource, *Data Sci. J.*, *8*, IGY6–IGY20.

Sheng, C., Y. Deng, X. Yue, and Y. Huang (2014), Height-integrated Pedersen conductivity in both E and F regions from COSMIC observations, *J. Atmospheric Sol.-Terr. Phys.*, *115–116*, 79–86, doi:10.1016/j.jastp.2013.12.013.

Slavin, J. A., G. Le, R. J. Strangeway, Y. Wang, S. A. Boardsen, M. B. Moldwin, and H. E. Spence (2008), Space Technology 5 multi-point measurements of near-Earth magnetic fields: Initial results, *Geophys. Res. Lett.*, *35*(2).

Snare, R. C. (1998), A History of Vector Magnetometry in Space, in *Measurement Techniques in Space Plasmas Fields*, edited by R. F. Pfaff, J. E. Borovsky, and D. T. Young, pp. 101–114, American Geophysical Union.

Spicher, A., T. Cameron, E. M. Grono, K. N. Yakymenko, S. C. Buchert, L. B. N. Clausen, D. J. Knudsen, K. A. McWilliams, and J. I. Moen (2015), Observation of polar cap patches and calculation of gradient drift instability growth times: A Swarm case study, *Geophys. Res. Lett.*, *42*(2), 201–206.

Stasiewicz, K. et al. (2000), Small Scale Alfvénic Structure in the Aurora, *Space Sci. Rev.*, *92*(3–4), 423–533, doi:10.1023/A:1005207202143.

Stewart, B. (1861), On the great magnetic disturbance which extended from August 28 to September 7, 1859, as recorded by photography at the Kew Observatory, *Philos. Trans. R. Soc. Lond.*, *151*, 423–430.

Størmer, C. (1935), Measurements of Luminous Night Clouds in Norway 1933 and 1934. With 3 Figures in the Text and 17 Plates, *Astrophys. Nor.*, *1*, 87.

Størmer, C. (1937), On the trajectories of electric particles in the field of a magnetic dipole with applications to the theory of cosmic radiation. sixth communication. with 17 figures in the text, *Astrophys. Nor.*, *2*, 193.

Sukhorukov, A. I., and P. Stubbe (1997), Excitation of the ionospheric Alfven resonator by strong lightning discharges, *Geophys. Res. Lett.*, *24*(8), 829–832, doi:10.1029/97GL00807.

Swift, D. W. (1981), Mechanisms for auroral precipitation: A review, *Rev. Geophys.*, *19*(1), 185–211, doi:10.1029/RG019i001p00185.

Texas Instruments Inc. (2016), *DRV425 Fluxgate Magnetic-Field Sensor*, Texas Instruments Inc.

Trigg, D. F., P. H. Serson, and P. A. Camfield (1971), A solid-state electrical recording magnetometer, *Publ. Earth Phys. Branch, Dept Energy, Mines and Resources*, *41*, 66–80.

Trondsen, T. S., L. L. Cogger, and J. C. Samson (1997), Asymmetric multiple auroral arcs and inertial Alfvén waves, *Geophys. Res. Lett.*, *24*(22), 2945–2948, doi:10.1029/97GL52855.

Vacquier, V. (1993), Many jobs, *Annu. Rev. Earth Planet. Sci.*, *21*(1), 1–18.

Vacquier, V., A. D. Raff, and R. E. Warren (1961), Horizontal Displacement in the Floor of the Northeastern Pacific Ocean, *Geol. Soc. Am. Bull.*, *72*(8), 1251–1258, doi:10.1130/0016-7606(1961)72[1251:HDITFO]2.0.CO;2.

Wallis, D. D., D. M. Miles, B. B. Narod, J. R. Bennest, K. R. Murphy, I. R. Mann, and A. W. Yau (2015), The CASSIOPE/e-POP Magnetic Field Instrument (MGF), *Space Sci. Rev.*, *189*(1–4), 27–39, doi:10.1007/s11214-014-0105-z.

Waters, C. L., B. J. Anderson, and K. Liou (2001), Estimation of global field aligned currents using the Iridium® system magnetometer data, *Geophys. Res. Lett.*, *28*(11), 2165–2168.

Watt, C. E., and R. Rankin (2009), Electron trapping in shear Alfvén waves that power the aurora, *Phys. Rev. Lett.*, *102*(4), 45002.

Watt, C. E. J., and R. Rankin (2012), Alfvén wave acceleration of auroral electrons in warm magnetospheric plasma, *Auror. Phenomenol. Magnetos. Process. Earth Planets*, 251–260.

Watt, C. E. J., R. Rankin, I. J. Rae, and D. M. Wright (2005), Self-consistent electron acceleration due to inertial Alfvén wave pulses, *J. Geophys. Res. Space Phys.*, *110*(A10), A10S07, doi:10.1029/2004JA010877.

Welch, P. D. (1967), The use of fast Fourier transform for the estimation of power spectra: A method based on time averaging over short, modified periodograms, *IEEE Trans. Audio Electroacoustics*, *15*(2), 70–73.

Wygant, J. R. et al. (2000), Polar spacecraft based comparisons of intense electric fields and Poynting flux near and within the plasma sheet-tail lobe boundary to UVI images: An energy source for the aurora, *J. Geophys. Res. Space Phys.*, *105*(A8), 18675–18692.

Yau, A. W., and H. G. James (2015), CASSIOPE Enhanced Polar Outflow Probe (e-POP) Mission Overview, *Space Sci. Rev.*, *189*(1–4), 3–14, doi:10.1007/s11214-015-0135-1.

Appendix A: Transconductance Amplifier Design and Sensitivity Analysis

This document was originally prepared as an internal technical note for the University of British Columbia Department of Geophysics and Astronomy Geophysical Instrumentation Laboratory [*Narod*, 1982]. It has been reproduced and expanded here for the public record.

A1 Introduction

The transconductance amplifier is one of the most critical components in a fluxgate magnetometer as it is its characteristics, combined with the thermal and electrical properties of the sensor, which determine the feedback transfer function and thus the performance of the instrument as a whole. The amplifier serves two functions. Firstly, it converts a voltage analogue of the magnetic field into a current, which in turn creates the nulling field in the sense coil. Secondly, by careful selection of the resistors, the amplifier can be made to compensate the first order measurement distortions caused by thermal expansion of the sensor.

A2 Circuit Analysis

An idealized circuit for the transconductance amplifier producing an output current I_F is shown in Figure A1.

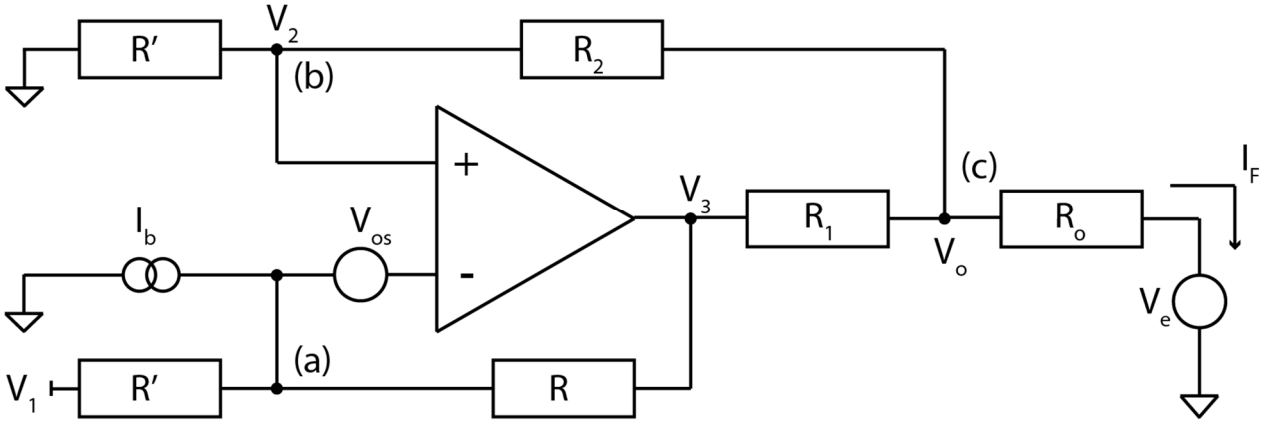

Figure A1: Idealised circuit for a transconductance amplifier.

Control voltage V_1 is attenuated 6 dB in the actual implementation of the transconductance amplifier by a summing node. R_1 is the current sense resistor. R_o is the sensor load resistance. Neglecting all noise sources (V_e, V_{os}, and I_b), the characteristic equations from nodes (a), (b), and (c) are respectively.

$$\frac{V_1 - V_2}{R'} = \frac{V_2 - V_3}{R} \tag{A1}$$

$$\frac{V_o - V_2}{R_2} = \frac{V_2}{R'} \tag{A2}$$

$$\frac{V_3 - V_o}{R_1} = I_f + \frac{V_2}{R'} \tag{A3}$$

where $I_f = \frac{V_o}{R_o}$ is the feedback current flowing into the sensor. Rearranging Eqs. (A1), (A2), and (A3) gives respectively

$$R'(V_2 - V_3) = R(V_1 - V_2) \tag{A4}$$

$$\mathrm{R'(V_o - V_2) = R_2(V_2)} \tag{A5}$$

$$\mathrm{R'(V_3 - V_o) = R_1 R' \frac{V_o}{R_o} + R_1 V_2} \tag{A6}$$

Combining Eqs. (A4) and (A6) to eliminate $\mathrm{V_3}$ gives

$$\mathrm{(R' + R - R_1)V_2 = RV_1 + R'\left(1 + \frac{R_1}{R_o}\right)V_o} \tag{A7}$$

Substituting Eq. (A5) to eliminate $\mathrm{V_2}$ gives

$$\mathrm{\frac{R'}{R' + R_2}(R' + R - R_1)V_o = RV_1 + R'\left(1 + \frac{R_1}{R_o}\right)V_o} \tag{A8}$$

Rearranging Eq. (A8) gives

$$\mathrm{I_f \equiv \frac{V_o}{R_o} = \frac{-V_1\left(\frac{R}{R_1}\right)}{R_1 + R_o - R_o\left(\frac{R' + R - R_1}{R' + R_2}\right)}} \tag{A9}$$

Rearranging and simplifying gives

$$\mathrm{I_f = \frac{-V_1\left(\frac{R}{R_1}\right)}{R_1 + R_o\left(\frac{R_1 + R_2 - R}{R' + R_2}\right)}} \tag{A10}$$

The ideal transconductance amplifier has the property that I_f is independent of R_o. From Eq. (A10), this the case when $R_1 + R_2 - R = 0$. However, here the design goal of the transconductance amplifier is to compensate for thermal variation in the sensor based on the resistivity coefficient of the copper sensor winding.

Defining the following parameters

$$G \equiv \frac{R}{R'} \tag{A11}$$

$$\beta \equiv \frac{R_1 + R_2 - R}{R' + R_2} \tag{A12}$$

$$R^* \equiv \left(\frac{1}{G}\right)(R_1 + \beta R_o) \tag{A13}$$

allows Eq. (A10) to be rewritten as

$$I_f = -\frac{V_1}{R^*} \tag{A14}$$

The design goal is met when I_f changes with R^* such that the offset field in the sensor is constant. The temperature dependence of the current output from the transconductance amplifier is

$$\frac{1}{I_f}\frac{dI_f}{dT} = \frac{-1}{R^*}\frac{dR^*}{dT} = \frac{-1}{R^*}\frac{d}{dT}\left[\frac{1}{G}(R_1 + \beta R_o)\right] \tag{A15}$$

Considering only the effect of temperature changes in the sensor then $\frac{d}{dT}R = 0, \frac{d}{dT}R_1 = 0, \frac{d}{dT}R' = 0$, and G is constant with respect to temperature. Taking the temperature coefficient of resistivity of the copper in the windings to be α_c, Eq. (8) then simplifies to

$$\frac{1}{I_f}\frac{dI_f}{dT} = \frac{-1}{R^*}\frac{1}{G}\left[\frac{d}{dT}R_1 + \beta\frac{d}{dT}R_o\right] = \frac{-1}{R^*}\frac{\alpha_c \beta R_o}{G} \tag{A16}$$

The offset field generated in the sensor is assumed to be proportional to the product of I_f and the sensor turns density which is further assumed to be determined by the coefficient of linear thermal expansion, α_m, of the bobbin which supports the sensor windings.

$$\frac{1}{I_f}\frac{dI_f}{dT} = \alpha_m \tag{A17}$$

This definition gives the following relationships

$$\beta = G\frac{-\alpha_m}{\alpha_c}\frac{R^*}{R_o} \tag{A18}$$

$$R_1 = GR^* - \beta R_o \tag{A19}$$

$$R_2 = \frac{R - R_1 + \beta R'}{1 - \beta} \tag{A20}$$

The procedure for designing the amplifier is then as follows:

1. Select R^* by determining a specification
2. Choose G, R, R'
3. Calculate β from Eq. (A18)
4. Calculate R_1 from Eq. (A19)
5. Calculate R_2 from Eq. (A20)

A3 Errors on Output

Suppose an error voltage V_e is placed in series with R_o. In the ideal transconductance amplifier, this would have no effect since it is insensitive to load variations. However, in an unbalanced amplifier, this produces a small error in the output. The analysis can be simplified by redefining the ground potential such that V_e is moved from the output to both inputs giving Figure A2.

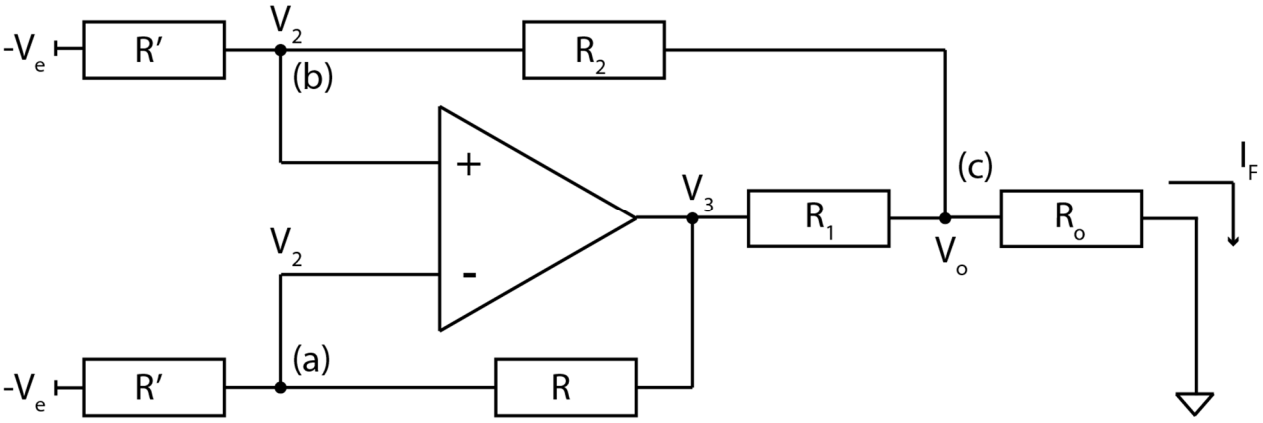

Figure A2: Error model for a transconductance amplifier.

The characteristic equations from nodes Eqs. (a), (b), and (c) respectively are then:

$$\frac{V_3 - V_2}{R} = \frac{V_2 + V_e}{R'} \tag{A21}$$

$$\frac{V_o - V_2}{R_2} = \frac{V_2 + V_e}{R'} \tag{A22}$$

$$\frac{V_3 - V_o}{R_1} = \frac{V_2 + V_e}{R'} + \frac{V_o}{R_o} \tag{A23}$$

or

$$R(V_2 + V_e) = R'(V_3 - V_2) \tag{A24}$$

$$R_2(V_2 + V_e) = R'(V_o - V_2) \tag{A25}$$

$$R'(V_3 - V_o) = R_1(V_2 + V_e) + \frac{R_1 R' V_o}{R_o} \tag{A26}$$

Rearranging and eliminating V_3 gives

$$(R + R' - R_1)V_2 = R'\left(1 + \frac{R_1}{R_o}\right)V_o + (R_1 - R)V_e \tag{A27}$$

Eliminating V_2 gives

$$\frac{(R + R' - R_1)(R'V_0 - R_2V_e)}{(R_2 + R')} = R'\left(1 + \frac{R_1}{R_o}\right)V_o + (R_1 - R)V_e \tag{A28}$$

or

$$\left\{(R + R' - R_1)R' - (R_2 + R')R'\left(1 + \frac{R_1}{R_o}\right)\right\}V_o = \{(R_2 + R')(R_1 - R) + (R + R' - R_1)R_2\}V_e \tag{A29}$$

This reduces to

$$I_{fe} = \frac{V_o}{R_o} = \frac{-V_e}{R_o - \frac{R_1(R_2 + R')}{R - R_1 - R_2}} \tag{A30}$$

or

$$I_{fe} = \frac{-V_e}{R_o + \frac{R_1}{\beta}} \tag{A31}$$

Thus the output circuit resistance is

$$\frac{-V_e}{I_{fe}} = R_o + \frac{R_1}{\beta} = R^*\frac{G}{\beta} = -R_o\frac{\alpha_c}{\alpha_m} \tag{A32}$$

Where $Z_{out} = \frac{R_1}{\beta}$ is the amplifier output impedance.

A4 Operational Amplifier Errors

Operational amplifier input offset error can be analysed by considering Figure A1 with $V_1 = 0$ and an offset voltage V_{os} on the inverting input. Then Eqs. (A1) and (A4) become

$$\frac{0 - (V_2 - V_{os})}{R'} = \left(\frac{V_2 - V_{os} - V_3}{R}\right) \tag{A33}$$

and

$$R'(V_2 - V_3 - V_{os}) = R(V_{os} - V_2) \tag{A34}$$

while Eqs. (A2), (A3), (A5), and (A6) remain constant. Defining a parameter V^* such that

$$RV^* = (R + R')V_{os} \tag{A35}$$

allows Eq. (A34) to be rewritten as

$$R'(V_2 - V_3) = R(V^* - V_2) \tag{A36}$$

which is identical in form to Eq. (A4) but with V_1 replaced by V^*. Starting from Eq. (A14), and substituting V^* for V_1 produces

$$I_{fos} = -\frac{V_{os}}{R^*}\left(1 + \frac{1}{G}\right) \tag{A37}$$

Similarly, for a bias current I_b at the inverting input Eqs. (A1) and (A4) become

$$\frac{0 - V_2}{R'} = \frac{V_2 - V_3}{R} - I_B \tag{A38}$$

and

$$R'(V_2 - V_3) = R(-V_2) + RR'I_B \tag{A39}$$

Defining

$$V^{\#} = R'I_B \tag{A40}$$

allows Eq. (A39) to be rewritten as

$$R'(V_2 - V_3) = R(V^{\#} - V_2) \tag{A41}$$

which is identical in form to Eq. (A4) but with V_1 replaced by $V^{\#}$. Starting from Eq. (A14), and substituting $V^{\#}$ for V_1 produces

$$I_{fb} = -\frac{R'}{R^*}I_b \tag{A42}$$

A5 Component Sensitivity

Equations Eqs. (A13) and (A14) combine to give

$$I_f = \frac{-V_1 G}{R_1 + \beta R_o} \tag{A43}$$

All the component sensitivities can be derived from Eq. (A43). βR_o is typically less than $1/100^{th}$ of R_1, so that absolute stability is almost chiefly dependent on the individual resistor R_1. The best quality resistors for the purpose are the metal foil variety with 0.5 ppm/deg temperature coefficients and 25 ppm/year drift.

G must also be stable but is principally a function of tracking stability between R, R', and R_2. Typically, 25 ppm/deg absolute and 2 ppm/deg tracking stability should be adequate. Lower cost high quality metal film or thin film chip resistors should prove satisfactory.

The implementation of β depends on G, α_c, α_m, R_o, and R^* - Eq. (A18). Thus knowledge of G and R^* is necessary for all deterministic design methods. A heuristic design method notes that the output impedance is dependent only on α_c, α_m, and R_o which must be known a priori. The principle function of a finite β transconductance amplifier is to create a well defined Z_{out} which can be achieved by adjusting R_2 to compensate for inexact implementation of G and R_1.

To achieve first order compensation of the design range β must be held within 1/30 of its target value. Accuracy of β is determined mostly by the ability of R and R_2 to track with each other Eq. (A12). By inspection of Eq. (A12), tracking tolerances can be relaxed as β is increased. Thus from Eq. (A18), G should be made as large as possible. Note that Eq. (A37) implies that this also reduces V_{os} sensitivity. The magnitude of G does however have a tradeoff with compliance of the amplifier.

A6 Cabling Considerations

For long cable runs (e.g., 100 m) cable resistance can be significant. The detrimental effect of long cables can be compensated by adding a lumped platinum resistance to the sensor. This has the positive effect of lumping the temperature sensing in a very well behaved localized resistor at the sensor. However increasing the effective R_o also decreases β thus putting greater demands on the implementation of R and R_2.

The preferred method is to have low resistance cable (<1 ohm) although a platinum sense element may also be required. Equation (A18) can then be modified to include: α_p, the temperature coefficient of platinum; R_p, the resistance of the platinum element; and R_c, the cable resistance

$$\frac{\beta}{G} = \frac{-\alpha_m}{\alpha_p} \frac{R^*}{R_o + R_p + R_c} \tag{A44}$$

where R_p dominates both R_o and R_c and α_p is known to be very close to α_c.

Appendix B: Material Notes from Machining and Testing the Experimental Sensors

B1 Material Notes from Machining the Experimental Sensors

MACOR and the three PEEK derivatives each presented unique machining challenges. The MACOR was machined using small diameter (3 mm to 8 mm) carbon steel or diamond tools, cutting fluid to control material heating, chamfered corners, and shallow cuts to avoid breakage. The cutting direction was found to be very important to avoid breakage; cutting in the entry direction worked well whereas cutting on the exit direction caused surface cracking. MACOR tolerated waterjet cutting which accelerated rough cutting. However, MACOR still rapidly blunted tools, leading to slow and expensive machining. Some MACOR stock also appears to have had internal fractures which could not be spotted by eye, causing a subset of nominally identical pieces to crack under normal machining.

All three PEEK derivatives machined well using slow tool speed and liberal use of coolant to minimise heating and the resulting hardening of the machined surfaces. Virgin PEEK was particularly susceptible and the surface finish was noticeably different from that of the as-purchased material. Virgin PEEK and 30% carbon filled PEEK both tended to deform during machining and two finishing passes were used to achieve reasonable tolerances. The 30% carbon filled PEEK also required an additional spring pass (repeating a tool path without advancing the cut) to remove protruding filaments from the machined surface. Overall, the 30% glass filled peek was the easiest to machine as it resisted surface hardening, did not accumulate surface fibres, and was less prone to deforming away from tools.

B2 Issues with 30% Carbon Filled PEEK

The manufacturer datasheets indicate that the 30% carbon filled PEEK has the best coefficient of linear thermal expansion of the PEEK derivatives (Table 4-3). However, other users had experienced these issues with the machined material causing short circuits [Werner Magnes, 2013, personal communication] and these issue were reproduced during assembly and testing. The machined 30% carbon filled PEEK bobbins were briefly flamed to remove any carbon fibers protruding from the machined surfaces. The sense windings on the 30% carbon filled PEEK bobbins had end-to-end resistances within the expected manufacturing variability. However, all the bobbins were found to be galvanically connected to their sense winding, suggesting at least

one short to the bobbin in each winding. One winding was removed and rewound but was still found to be galvanically connected to the bobbin.

During initial testing, the Carbon/PEEK sensor exhibited sudden and unpredictable changes of both sensitivity and offset during preliminary temperature cycling. The authors speculate that residual carbon fibres on the machined bobbin surface or the crevice where machined faces meet were causing intermittent shorts as the sensor expanded, contracted, and flexed during temperature cycling. These changes stopped occurring after several temperature cycles. The authors speculate that the carbon fibres were broken by the mechanical action of the temperature cycling or the shorts had reached a steady state.

The volume resistivity of the purchased 30% carbon filled PEEK was estimated using the van der Pauw method [*van der Pauw*, 1958] to test the residual material from the rectangular 31x31x1.25 cm slab of material used to make the bobbin. The volume resistivity measured 0.3 Ω-cm compared to the 10^{16} Ω-cm given in the datasheet. A subsequent broader search of datasheets for comparable materials from several vendors and manufacturers found large variations in parameters including resistivity values ranging from 10^{5} to 10^{16} Ω-cm.

Overall, the 30% Carbon filled PEEK was found to be significantly different from the material specified in the manufacturers data sheet and appears to have caused shorting in the sensor. The authors consider it a poor candidate for future sensors and consider the data taken with the experimental Carbon/PEEK sensor to be unreliable.